ISTITUTO ITALIANO DI TECNOLOGIA
CENTER FOR NANO SCIENCE AND TECHNOLOGY

POLITECNICO
MILANO 1863

Doctoral program in Energy and Nuclear Science and Technology
XXIX cycle

HIGH PERFORMANCE CERAMIC COATING FOR DEMO BREEDING BLANKETS

Ph.D. candidate:
Iadicicco Daniele
matr. 820851

Supervisors:
Prof. Marco G. Beghi
Dr. Fabio Di Fonzo

Tutor:
Prof. Carlo E. Bottani

January 2017

A Viola
e Valeria

Acknowledgments

This work has been made possible thanks to the financial support and collaboration of the *C.R. ENEA of Brasimone (BO)* and the *EUROfusion consortium*.

I would first like to thank the many colleagues and friends that helped and advised me in over 3 years research activity at *Center for Nanoscience and Technology* of *Istituto Italiano di Tecnologia*. In particular, special thanks go to Giorgio Nava, Francesco Fumagalli, Matteo Vanazzi, Alessandro Mezzetti and Francisco Garcia Ferré for many useful discussions, ideas and scientific advise and to all colleagues of the *N2E Labs*.
I'm grateful to the technician guys, in particular Enrico Patti for his enormous patient and to all administrative people: Tessa, Silvia and Alessandra. I'm also grateful to Marco Utili and Serena Bassini for scientific support and corrosion testing at the *C.R. ENEA Brasimone* test facilities. I would also acknowledge Mariano Tarantino, Pietro Agostini and again Marco Utili of *C.R. ENEA Brasimone* for believing in this project, and for financial and materials support. Finally, the most sincere acknowledgment goes to my family for the endless and unconditional support.

Milano, January 2017
Iadicicco Daniele

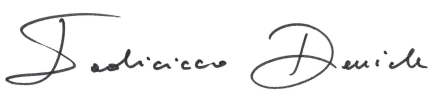

Contents

List of Acronyms

ADS: Accelerator Driven Systems
AFM: Atomic force microscope
ALD: Atomic Layer Deposition
BCC: Body Centered Cubic
CIEMAT: Centro de Investigaciones Energeticas Medioambientales y Tecnologicas
CVD: Chemical Vapor Deposition
DBTT: Ductile to Brittle Transition Temperature
DCLL: Dual Coolant Lead-Lithium
DEMO: DEMostrator reactor
DPA: Displacement per Atoms
EBN: Ellipsometry Brillouin Nanoindentation
EDX: Energy Dispersive X-ray
ENEA: Agenzia Nazionale per le nuove tecnologie, l'energia e lo sviluppo economico sostenibile
FAC: Flow Accelerated Corrosion
FCC: Face Centered Cubic
FMS: Ferritic-Martensitic Steel
GIV: Generation IV
HCLL: Helium Cooled Lead-Lithium
HCPB: Helium Cooled Pebble bed
HLM: Heavy Liquid Metal
ITER: International Thermonuclear European Reactor
JRC: Joint Research Center
LBE: Lead-Bismuth Eutectic
LCF: Low Cycle Fatigue
LFR: Lead Fast Reactor
LMAC: Liquid Metal Assisted Creep
LME: Liquid Metal Embrittlement
LOCA: Loss Of Coolant Accident
ODS: Oxide Dispersion Strengthened
PLD: Pulsed Laser Deposition
PRF: Permeation Reduction Factor
PVD: Physical Vapor Deposition
QMS: Quadrupole Mass Spectrometer
RAFM: Reduction activation ferritic-martensitic
R&D: Research and Development

RIPER: Radiation Induced Permeation and Released
RMS: Root Mean Square Roughness
SBS: Surface Brillouin Scattering
SEM: Scanning Electron Microscope
VPS: Vacuum Plasma Spraying
WCLL: Water Cooled Lead-Lithium

Synopsis

This Ph.D work focuses the characterization of alumina (Al_2O_3) ceramic coating as barrier against hydrogen permeation and corrosion in heavy liquid metals as well as the development of custom made Atomic Layer Deposition facility. The study is of particular relevance on the development of the advanced nuclear fusion DEMO reactor.
One of the major bottleneck for the development of DEMO breeding blanket is the degradation of candidate structural steels (ferritic-martensitic eurofer97) at high temperature by means of corrosion and tritium permeation. The most promising route available for an attempt to reduce hydrogen permeation and mitigate corrosion attack is the application of surface ceramic coatings. Al_2O_3 is considered from the seventies the major barrier candidate, thanks to its chemical inertia in heavy liquid metal and stability even at high temperature.
In order to meet requirements, a room temperature PLD process is proposed along with a custom made ALD facility, according to a bottom-up approach. Eurofer97 disks are covered starting with different morphologies and finally focused on compact and dense amorphous alumina. Performances as hydrogen permeation barrier are tested in PERI II facility up to 923K obtaining a promising PRF result close to 10^5. Short-term (1000h) corrosion tests in static eutectic Pb-16Li at 873K are performed at ENEA Brasimone. SEM analysis reveal that compact amorphous alumina performs as barrier against corrosion-dissolution by heavy liquid metals. Characterization of the PLD-grown coating is also performed by SEM and AFM analysis.
Also, development of a custom made ALD is carried out. Set up of fundamental parameters in order to define the so called ALD regime are defined for the most common metal oxides, namely alumina and titania. A first of kind thermal cycle tests in air demonstrate the adhesion and barrier potential of alumina grown by ALD.
This thesis is structured as follow: Chapter 1 introduces fusion reactors design with a focus on breeding blanket materials challenge. Chapter 2 details the main relevant phenoma in breeding blankets such as gaseous permeation and corrosion by heavy liquid metals. Chapter 3 is devoted to describe the Ph.D. work results for the ceramic coating on eurofer97 steels and the development of the ALD facility. In Chapter 4 conclusions and remarks. Chapter 5 describes materials and method used in this Ph.D work.

Chapter 1

Introduction

1.1 Introduction

The access to reliable and affordable energy is thought of as crucial to worldwide economic prosperity and stability. Today, nuclear power is totally provided by fission reactors providing about 11% of the global demand of electricity. The most diffuse reactor design worldwide is the Pressurized Water Reactor (**PWR**), accounting for two-thirds of the installed capacity, follows by Boiling Water Reactor (**BWR**) and Pressurized Heavy Water Reactor (**PHWR** or **CANDU**).[1, 2]
A long term electrical energy production needs economical and ecological sustainable energy resources. Among the variety of renewable energy resources (e.g. wind, photovoltaic, geothermal and hydrogen) two nuclear technologies are able to achieve all these requirements:

- Generation IV (**GIV**), fast fission reactors.
- Fusion reactors.

In fact, according to the **2015 United Nation Climate Change Conference - COP 21 or CMP 21**, held from 30th November 2015 to 12th December 2015 in Paris, nuclear power will play a central role in green house reducing and future energy sustainability.
Over the past decade, the scientific community has explored six particularly appealing advanced designs as potential Generation IV fast fission reactors.[3–5].
The concepts selected are:

- Super-critical Water-Cooled Reactor (**SCWR**)
- Sodium Fast Reactor (**SFR**)
- Lead Fast Reactor (**LFR**)
- Very-High Temperature Reactor (**VHTR**)
- Gas Fast Reactor (**GFR**)
- Molten Salt Reactor (**MSR**)

Nuclear fusion systems offer the possibility of an inexhaustible energy source. It has many potential advantages as compared to nuclear fission system, such as[6–8]:

- **Higher efficiency**: The basic fusion reactions are more energetic than the fission reactions and light nuclei are plentiful and easy to obtain.
- **Safe and controllable**: In case of accident (e.g. LOCA) reaction can be stopped without fuel melting risks.
- **More environmental acceptable**: Fusion products are usually light, stable nuclei rather than heavy radioactive ones.

Today, the nuclear fusion of a **deuteron**, (^{2}H), and a **triton**, (^{3}H), is considered to be the most promising reaction ($^2H +^3 H \rightarrow^3 He + n$) for a commercial fusion power plant, thanks to its highest cross-section at lower energies, as shown in figure 1.1.

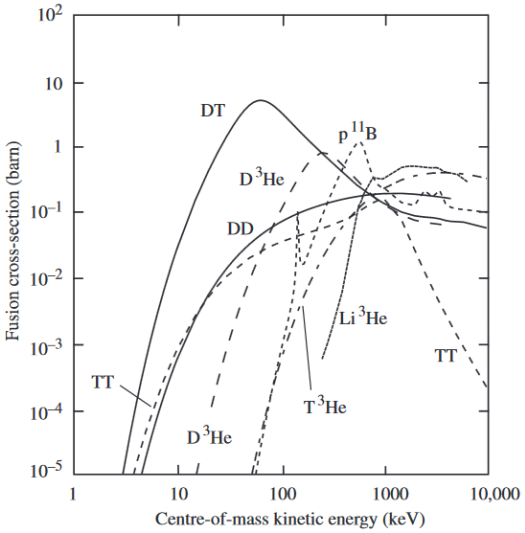

Figure 1.1: Fusion reactions cross sections versus center-of-mass energy for reactions. The curve DD represents the sum of the cross sections of the various branches of the reaction. Cross section is expressed in **barn**. 1 barn is equal to 10^{-24} cm^2.[8]

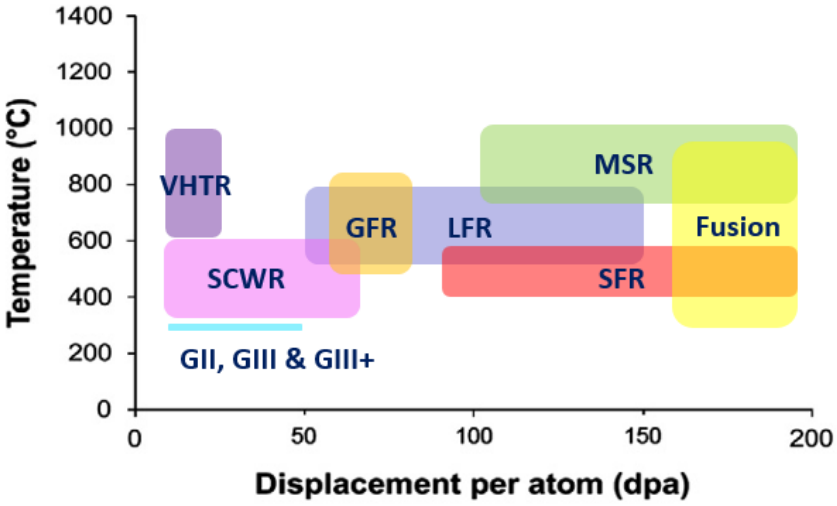

Figure 1.2: Temperature and DPA requirement for structural materials for future concept nuclear reactors. The dimensions of the rectangles define the ranges of temperature and dpa for each reactor design.[9]

Nuclear fusion reaction occurs only overcoming the **Coulomb repulsion** (temperatures of plasma of about 20 KeV, corresponding to 2 10^8 K are required) in order to bring the two nuclei close enough (about 10^{-14} - 10^{-15} m). Energy from fusion power will be extracted from 14.1 MeV kinetic energy of neutrons as product of **deuterium-tritium** fusion reactions. Thus, this energy should be adsorbed, efficiently channeled and eventually used for the generation of electricity by conventional scheme of a thermal power plant. Unfortunately, as shown in figure 1.2, all GIV designs and fusion design require an aggravation of the operating conditions (respect to the current technologies) in term of operating temperatures and radiation damage levels (quantified by the international parameter Displacement per Atom or **dpa**).[9–12]

Thus, the development of **GIV** and **fusion systems** depend to the successful resolution of several materials challenges.

1.2 Thermonuclear reactor

At the required energy to induce fusion, the atoms of a gas are stripped of their electrons forming a highly ionized gas described as **plasma**. Furthermore, the first step for a fusion reactor is to confine the internal energy of the plasma for a sufficient time, τ_E, to obtain a balance between the power output from the fusion reactions and the power input to make the reaction possible. This condition of breakeven is denote as **Lawson's criterion**, which, for the D-T reaction, is:

$$n\tau_E \geq 6\ 10^{19} \quad [s\ m^{-3}] \tag{1.1}$$

Where n is the plasma density at temperature of 10 keV. Since the temperature related to the kinetic energy of nuclei is over 10^8 K (mean particle kinetic energies of 10 keV), thus a physical plasma confinement is impossible. Actually, in the last decade two strategies are developed, in particular:

- **Magnetic confinement.**
- **Inertial confinement.**

In **Inertial confinement** a tiny pellet containing deuterium and tritium is suddenly struck with an intense laser pulse that both heats the pellet and compresses it to high density (up to $n \sim 10^{24}$ [nuclei cm^{-3}]).

The aim of inertial confinement is to achieve densities and temperatures that are high enough that fusion can occur before the pellet simply expands and blows apart. Considering the Lawson's criterion for D-T fusion reaction and expanding time in the range of 10^{-9} the confinement time must be at least the same. The sequence of processes in laser-driven fusion might be as follows: a pellet is injected into the reactor and simultaneously struck from many directions by an intense laser pulses. The outer layer of the pellet is vaporized and forms a plasma, which continues to absorb the laser radiation. At this point plasma itself is unconfined and it rapidly ablates, which drives a compressional šhockẅave back into the remaining pellet. This wave compresses and heats the core of pellet to the point at which thermonuclear ignition can occur, as shown in figure 1.3

Magnetic confinement confines plasma by means of the interaction with charged particles of plasma itself with a carefully design magnetic fields. The confinement plasma time in the order of second and according to Lawson's criterion the thermonuclear plasma density must be in the order of 10^{14} [nuclei cm^{-3}]. At present, the closed magnetic systems, **Tokamak** configuration, have been regarded as the most promising means for plasma confinement for **ITER** (International Thermonuclear Reactor) and **DEMO** (DEMOstrator reactor). Tokamak configuration is characterized by axial symmetric closed magnetic surfaces traced out by magnetic field lines, which fill the surface itself ergodically. A plasma ion spirals along a line of the magnetic field until it is remove by collision with another object. Figure 1.4 resumes the magnetic configuration of a typical tokamak reactor design.

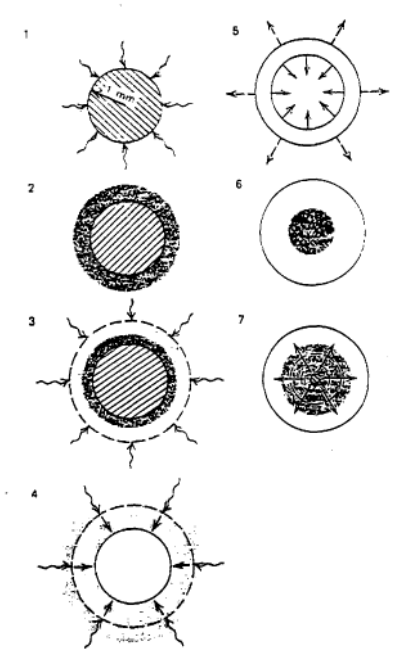

Figure 1.3: Sequence of stages in inertial confinement fusion: a)irradiation of fuel pellet by lasers or ion beams;b)formation of plasma atmosphere;c)additional external radiation adsorption;d)ablation and resulting imploding shock wave;e)shock wave conpressing core;f)ignition of core;g)burn propagating outward.[14]

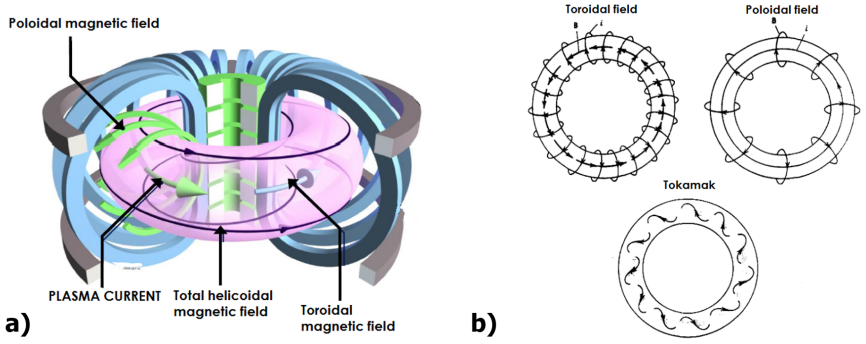

Figure 1.4: a)Magnetic fields configuration for a Tokamak reactor design.[13];b)A toroidal field is produced by a winding of coils and poloidal field is prouced by an axial current. (The current is of the order of a few MA. The use of transformer requires the tokamak to operate in a pulsed mode) The resulting of toroidal and poloidal fields is an helix, called tokamak, through which the ions can travel in closed orbits.[8]

Within the **European** fusion development scenario, **DEMO** will be the key device for meeting the following milestones:

- Qualification of materials: up to 120 - 150 dpa for first wall (blanket materials) and 40 - 60 dpa for divertor materials.
- Qualification of **in-vessel** materials: mainly welding, brazing and hipping up to 100 dpa for blanket and 40 dpa for divertor.
- Qualification of tritium systems: recovery, extraction and recirculation.

- Qualification of **ex-vessel** components and systems, such as: high temperature superconductors and balance of plant components.
- Validation of vacuum vessel and blanket architecture.
- Validation of divertor functional performance.
- Validation of blanket functional performance.

In additional to meeting the above milestones, both DEMO and future Fusion Power Plant will have to satisfy a number of requirements in the area of **safety, public acceptance** and **economics**.
Currently, **DEMO** reactor design has not been formally selected as well as operational requirements. Two main different **DEMO** design options are proposed for fusion European project:

- **Near-term DEMO**: is characterized of a *conservative-based design* deliverable in medium term (before 2030). Its substantially based on ITER design and performance (with a Q-value around 10) with modest power density and long pulse plasma. **Near-term DEMO** has the advantage of adopting the mature and reliable technology and materials.
- **Advanced DEMO**: based on more optimistic physics assumptions such as high-density power, high current drive steady-state plasma and design an reliable closed-fuel cycle. Unfortunately, its less mature technology that induce on long term time scale construction (not before 2050).

For both designs the performance of the materials is mandatory to the success of **DEMO** design. Suitability of robust and durable materials determine the fundamental existence of workable reactor itself and demonstrate the potential economics of fusion energy.
As well as the **in-vessel** components a key component for the success of fusion reactor is the so-called **Breeding Blanket**. For the tokamak configuration breeding blanket will provide the thermal energy extraction, 80 % of the fusion energy, (and its successive conversion to electricity) and tritium breeding in order to sustain the fusion reaction by replace the tritium burnt in the vacuum vessel. As shown in figure 1.5, breeding blanket is located behind the first wall surrounding the vacuum vessel.

Breeding Blankets materials, as listed before in the milestones, will be subjected to a very high neutron damage at high temperature (up to 823 K) as well as high thermal load (up to 2 MW m^{-2}). Several simulations are carried out to determine these parameters. For a 2,7 GW_{th} fusion reactor, a neutron flux over a 6 10^{22} n m^{-2} s^{-1} immediately behind the first wall is considered, that correspond to a damage up to 18 dpa per year of operation. Moreover 12 appm of **He** per dpa production ratio for transmutation must be considered.[15–17] A variety of breeding blankets concepts has been proposed worldwide, ranging from more conservative designs to higher-risk, highest-payoff designs for advanced **DEMO** and commercial **fusion reactors**.

1.2.1 European breeding blankets

European breeding blankets designs are still under investigation following the European **Power Plant Physics and Technology, PPPT** programme, organized within the **EUROfusion**

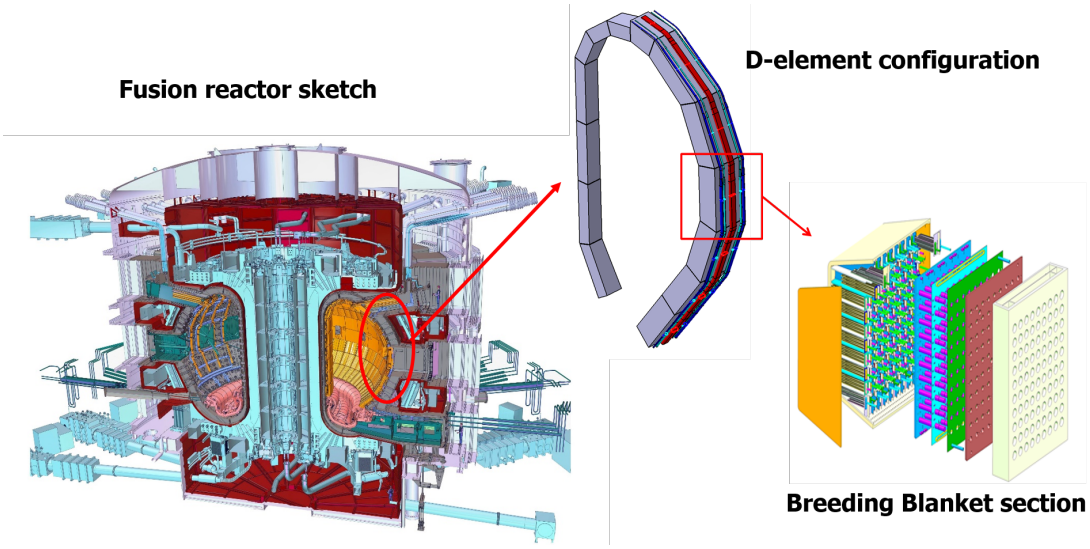

Figure 1.5: Sketch of Tokamak fusion reactor design. The vacuum vessel will be surrounde of D-elements that consist of a series of **breeding blankets**. For a DEMO reactor is expected from 200 to 400 breeding blankets elements, depending on selected design

consortium.
Four different design concepts are under investigation, tentatively to meet a set of **DEMO** requirements such as: **tritium breeding ratio (TBR)**, **net thermal conversion efficiency exceeding 20%**, **lifetime exceeding 40000 hours** and use of **structural materials** having a well established properties and known to behave satisfactorily under high fluence irradiation (described in section 1.2.2). Tritium breeding is efficiently obtained by means of **lithium** following the the fission reaction ^{6}Li + n $\rightarrow$ ^{4}He + 4,8MeV.
Attaining a **TBR** over unity proves to be a challenging task, the production of one tritium atom by the ^{6}Li (n,α)T reaction consumes one neutron, while the D-T fusion reaction generates only a neutron which has a probability (up to 35%) of not being available for tritium breeding (due to absorption in structural materials or streaming through the blanket openings). To replace neutron losses a **neutron multiplier**, by means of the reaction (n,2n), must be considered. For the four European breeding blankets designs the main candidates are **beryllium** for solid breeder and **lead** for liquid breeder designs.

Helium Cooled Pebble Bed (HCPB) breeding blanket

A blanket module consist of a **RAFM** steel box with a dimensions of 840mm x 1576mm x 2141mm (radial x toroidal x poloidal). HCPB module includes a U-shaped first wall, stiffening grids, box manifold, two caps at the top and the bottom and the integrated back supporting structure. Lithium, enriched to 60% at.w, is sintered in a orto-silicate ceramic ball (Li_4SiO_2) within **beryllium** as neutron multiplier. Sintered ball is filled in the form of pebble beds in the space between the cooling-stiffening plates. Cooling of breeder units, first wall and box structure is performed by means of high pressure (8 MPa) **helium** gas. Figure 1.13 shows a sketch of HCPB design.[18, 20–22]

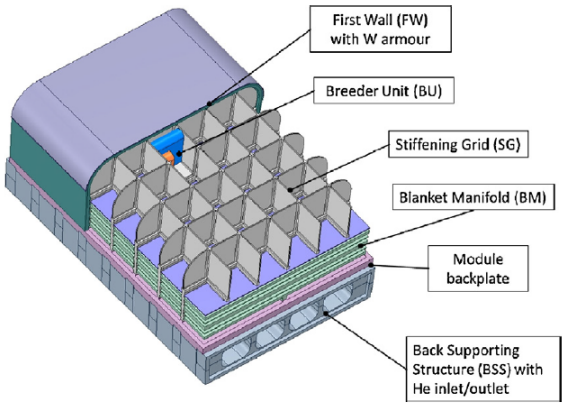

Figure 1.6: HCPB conceptual design. [21]

Helium Cooled Lithium-Lead (HCLL) breeding blanket

As the same matter of HCPB module, HCLL is a **RAFM** steel box within the same dimensions and box design. Here, eutectic **Pb-16Li** alloy, enriched up to 90% in ^{6}Li, is used as tritium breeder (lithium) and neutron multiplier (lead). Cooling of the eutectic alloy, first wall and box structure is provided by high pressure (8 MPa) helium gas. To extract efficiently tritium eutectic alloy is circulated at low velocity (few millimeters per minute). Moreover, a complex manifold scheme is required for the circulation of both the **Pb-16Li** and the **Helium** gas as shown in figure 1.7.[18, 20–22]

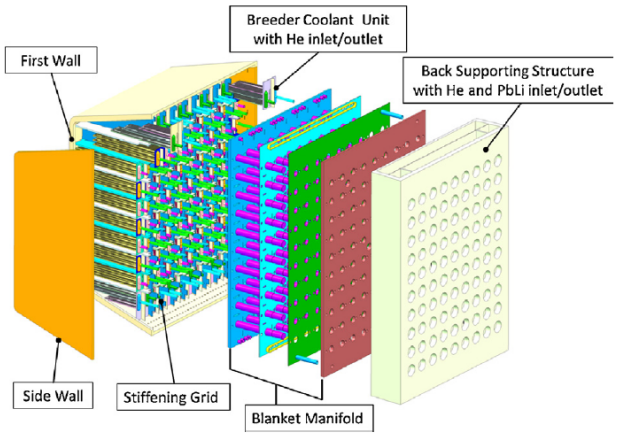

Figure 1.7: HCLL conceptual design. [21]

Water Cooled Lithium-Lead (WCLL) breeding blanket

Water Cooled breeding blanket employs the eutectic **Pb-16Li** alloy for tritium breeding and neutron multiplication as the same matter as HCLL concept. As the previous breeding blanket design concepts, box is composed of **RAFM** steel with first wall, caps, back wall and back supporting structure with inlet and outlet pipes for coolant and eutectic alloy. Figure 1.8

provides scheme of ENEA improved WCLL design.

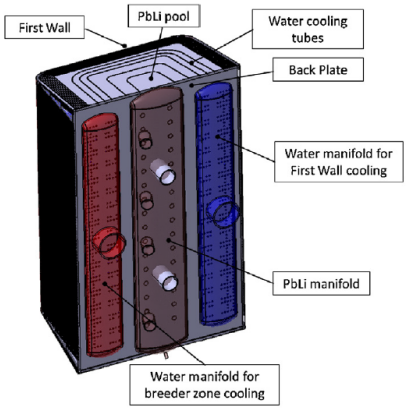

Figure 1.8: WCLL conceptual design. [21]

Here, cooling is provided by a pressurized water flowing in a pipes through the **Pb-16Li** pool, in a similar configuration of Pressurized Water Reactors (PWRs). (Using a well known PWR technology, makes WCLL one of the major Breeding Blanket candidate for **near-term DEMO** reactor)[18, 20–22].

Dual Coolant Lithium-Lead (DCLL) breeding blanket

Dual Coolant Lithium-Lead breeding blanket uses liquid eutectic **Pb-16Li** as tritium and neutron multiplier as well as coolant. Differently from WCLL and HCLL, **Pb-16Li** circulate at higher velocity (up to few centimeters per second) in large channel closed inside **RAFM** made steel box for removing the heat from the breeding zone. Similarly, DCLL box has the same dimension of three last breeding blanket concepts, as shown in figure 1.9.

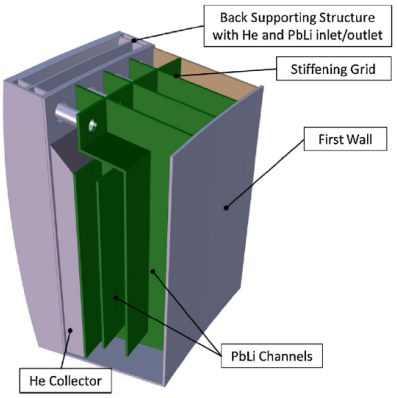

Figure 1.9: DCLL conceptual design. [21]

Finally, high pressure helium gas circuit (up to 14 MPa) is used to remove heat from the first wall.[18, 20–22]

In table 1.1 the mainly breeding blanket parameters are summarized.

	HCPB	HCLL	WCLL	DCLL
Breeder	Li_4SiO_2	Pb-16Li	Pb-16Li	Pb-16Li
Coolant	He	He	H_2O	Self + He
Structural materials (SM)	Eurofer97	Eurofer97	Eurofer97	Eurofer97
SM $\mathbf{T}_{max}$(K)	823	823	823	823
SMT$_{min}$(K)	573	573	538	573
Breeder $\mathbf{T}_{max}$(K)	1163	873	873	973
Breeder $\mathbf{T}_{min}$(K)	673	573	558	733
Coolant $\mathbf{T}_{max}$(K)	773	773	598	He: 753
Coolant $\mathbf{T}_{min}$(K)	523	523	538	He: 573
Coolant P(MPa)	8	8	15.5	14
TBR	1,04	1,07	1,13	1,04
Tritium production(g day^{-1})	356	356	356	356
Cycle η(%)	37	37	33	45
SM lifetime criteria	150 dpa-swelling	150 dpa-swelling	150 dpa-swelling	150 dpa-swelling

Table 1.1: Resuming of the mainly European breeding blankets parameters.

The minimum **TBR** value required for an effectiveness tritium self-sustain is 1.10. Thus, the only reliable design to day is the WCLL. Another advantage of the WCLL design is the well known **PWRs** technology adopted. On the contrary, as well as for HCLL and DCLL, **corrosion** by interaction of high temperature heavy liquid metal and tritium **permeation** from breeding zone to coolant system are the major bottlenecks on DEMO breeding blankets developments.

1.2.2 Breeding blankets structural materials

The general environment framework for the current and future nuclear reactors, in terms of operating temperatures and radiation damage (**dpa**) of the structural materials in shown is figure 1.2. The **fusion reactors** region and its conditions are fairly within reach if compared with those predicted for the future fission systems (namely **Generation IV**).
The choice of suitable structural materials for the **eutectic Pb-16Li** environment remains however the main technological issue for the breeding blankets that has to be solved to achieve **DEMO** deployment. In addition to high power density, high temperatures, high dose by energetic neutron spectrum, corrosion aggressiveness and tritium permeation impose several and special requirements to structural materials. Dimensional stability (in terms of void swelling, thermal and irradiation creep), adequate thermal, mechanical and chemical properties, as well as corrosion, tritium retention and liquid metal embrittlement resistance should be guaranteed under all operating conditions. Historically, the most used materials in liquid metal fast reactors (e.g. Superphenix, Phenix in France or Monjiu in Japan) is the austenitic stainless steel **AISI 316L** since its good behavior under creep conditions at high temperature and its high corrosion resistance in liquid sodium.
Austenitic stainless steels are Fe-Cr-Ni-C alloys with content of chromium between 16 and 28 wt.% and nickel between 6 and 32 wt.%. Austenitic steels have a face centered cubic (or **FCC**) crystalline structure by means of the presence of nickel. Austenitic structure enhances mechanical strength, tenacity, fatigue resistance and creep behavior.
Their main characteristic is the elevated resistance to creep and corrosion, even at high temper-

ature thanks to the presence of chromium that in an oxidizing environment induces formation of a thin and compact oxide layer. Generally, austenitic steels, the most common are the AISI 300 series (e.g AISI 304 and 304L, AISI 316 and 316L, AISI 321 and AISI 327), are though and ductile. Under fast neutron irradiation embrittlement phenomena may occur, causing an increase of both the **ultimate** and **yield stress**, and a reduction of the **plastic resources** before rupture as shown in figure 1.10.[23]

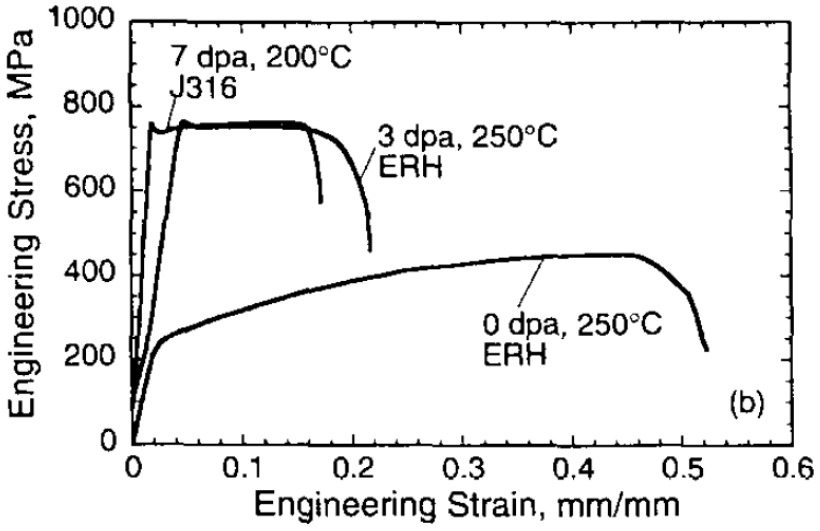

Figure 1.10: Effect of neutron irradiation to 3 and 7 dpa on the engineering stress-strain curves for AISI 316LN steel.[23]

The reduction in elongation and strain hardening capacity have been attributed to flow localization and strain hardening exhaustion mechanisms.[24–30] Therefore, austenitic steels, with high nickel content, are sensitive to **irradiation-swelling** phenomena. In fact nickel isotopes, in particular Ni^{58} and Ni^{59} present high (n,α) cross section. Swelling can also give rise to severe **inter-granular** embrittlement by means of the **helium bubbles** produced through the neutrons reactions with α particles.
On the other hand, the Ductile Brittle Transition Temperature (or **DBTT**) shift is not relevant, even at high irradiation dose.[31–34] The need to reduce severe swelling at high radiation level (i.e. up to 200 dpa) leads to consider the swelling-resistant **Ferritic-Martensitic steels**. Ferritic-martensitic steels with 9-12 wt.% of chromium were developed more than fifty years ago in high temperature working systems. Then, are widely used in heaters, boiler and heat exchangers. Compared with the well known austenitic steels, ferritic-martensitic steels show advantages such as **higher strength, improved resistance to thermal fatigue, higher thermal conductivity, lower thermal expansion coefficient** and **higher swelling resistance**. Ferritic-martensitic steels are body centered cubic (or **BCC**) crystalline structure; the low nickel content is not sufficient to stabilized the austenitic structure at room temperature. These alloys show the typical mechanical properties of ferritic BCC steels, but the presence of chromium enhances its resistant in oxidizing environment. Unfortunately, under neutron irradiation, BCC steels show an increase of **mechanical strength** and consequently a reduction in **ductility**, more then austenitic steels; as shown in figure 1.11.[35]

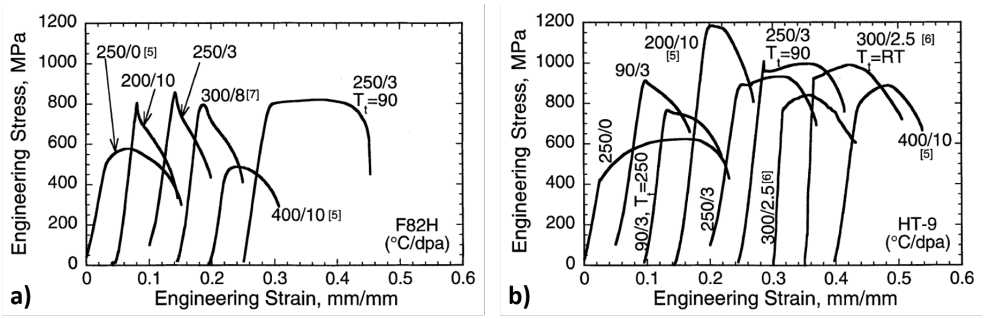

Figure 1.11: Effect of neutron irradiation up to 10 dpa on the engineering stress-strain curves for ferritic-martensitic steels at different temperature. a)F82H steel; b)HT-9 steel.[35]

Moreover, neutron irradiation shifts positively their **DBTT** even at low doses (i.e doses as low as 1 dpa). Then these steels might operate in the brittle zone already at the beginning of life. **Irradiation swelling resistance** and lower **helium embrittlement** make ferritic-martensitic steels attractive. For these reasons they are considered as the candidate structural materials for DEMO breeding blankets.[36]

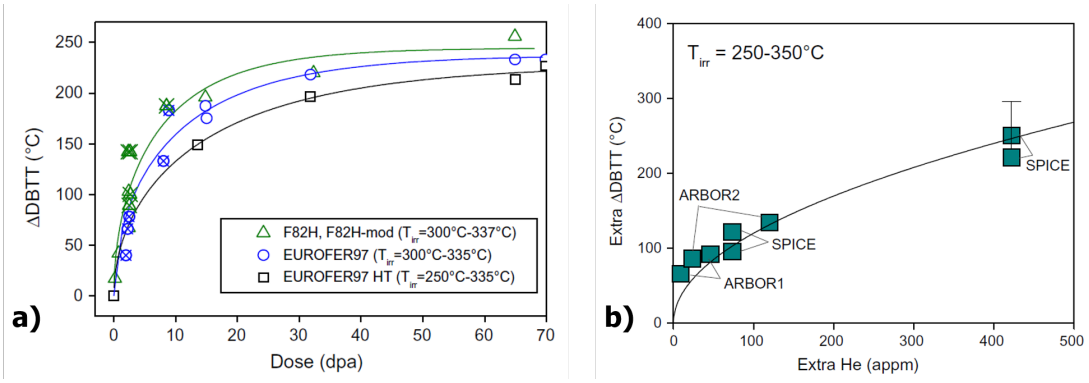

Figure 1.12: (a) Evolution of the irradiation embrittlement define as DBTT shift in function of neutron dose for eurofer97, eurofer97 HT and F82H steels. (b) Helium induce extra embrittlement.[38]

Reduction activation ferritic-martensitic[1], **RAFM**, steels are primary candidate structural materials for the **first wall** and **breeding blankets** that use the liquid breeder **Pb-16Li**. The 9%Cr-WVTa **Eurofer97** is today the major structural material candidate for the european DEMO project. Typical chemical composition of ferritic-martensitic candidate steels are resumed in table 1.2 below.

Although the radiation damage resistance of eurofer97 steels is superior to that the conventional ferritic-martensitic steels, **low temperature irradiation hardening, embrittlement** and **reduced ductility** remain the limiting factors for material application in DEMO relevant conditions.

Figures 1.12 and 1.13 underline the further needs of material development (e.g. **ODS RAFM** steels) as well as new approaches in breeding blankets designs optimization.

[1]The successful development of a reduced-activation materials was one of the major achievement in the last past decades. Their composition should make activation as low and quickly decaying as possible. Compared to conventional martensitic steel which need about 2 10^5 years to achieve low-level waste, (8-9)Cr-(1-2)WVTa ferritic-martensitic RAFM steels reach low-level waste already within 80-100 years.[37]

steel	C	Cr	Ni	Mo	V	Nb	Si	Mn	S	P	Ta	Al	W	Cu
Eurofer97	0,11	8,95	-	≤0,001	0,2	0,0017	0,04	0,048	-	0,125	-	-	1,08	-
T91	0,1	8,9	0,1	0,9	0,2	0,08	0,2	-	0,001	0,12	-	0,01	-	0,08
F82H	0,09	7,8	0,04	≤0,01	0,16	≤0,01	0,13	0,18	0,003	0,004	0,02	≤0,01	2	≤0,007
MANET II	0,11	10,3	0,65	0,58	0,19	0,14	0,18	0,85	0,004	0,005	-	0,012	-	0,01

Table 1.2: Typical chemical composition (in wt.%) of the candidate structural steels for **DEMO breeding blankets**

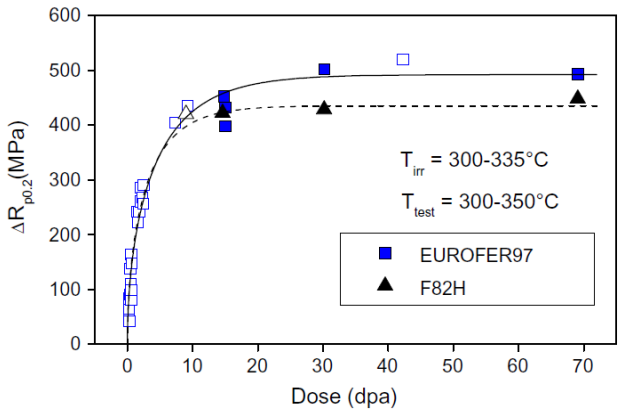

Figure 1.13: Hardening evolution in function of neutron irradiation dose for eurofer97 and F82H steels.[38]

1.2.3 Operating temperature windows for breeding blanket structural materials

As mention before, several phenomena occur in structural materials that modify their mechanical properties during the normal operation. All of these phenomena are temperature and dose irradiation depending. Consistently a critical analysis in materials selection is mandatory, defining the allowable operating temperature window for structural alloys in a fusion reactor. The **lower temperature limits** for ferritic-martensitic steels are due to(with a BCC structure) radiation hardening at low temperature can lead to a large increase in the **DBTT** temperature.[36, 39–42]
For **BCC** steels radiation hardening at low temperature (i.e. below $0.3T_M$, where T_M is the melting point) is already pronounced for doses as low as 1 dpa.[42–44]
The amount of radiation hardening typically decreases rapidly at irradiation temperature above $0.3T_M$, at which radiation-induced increase of the **DBTT** may be considered as acceptable. Both radiation hardening and **DBTT** shift appear to approach a saturation values following low temperature irradiation to doses above 10 dpa.[45–47] Resuming, the lower operating temperature limit in ferritic-martensitic steels (in general in all **BCC** and most of **FCC** alloys) is determined by **radiation embrittlement** (or decrease in fracture toughness) which is generally pronounced for irradiation temperature below $0.3T_M$.
The **upper temperature limit** is determined by one of the following factors:

- thermal creep (grain boundary sliding or matrix diffusional creep).
- high temperature **He** embrittlement of grain boundaries.

- cavity swelling.
- corrosion issues (coolant compatibility).

In many cases, especially for **lead-cooled fast reactor**, the upper temperature limit will be determined by coolant-corrosion compatibility rather than by thermal creep or radiation effects. In the case of fusion reactor conditions, **He embrittlement** may cause (some experimental studies have provided evidence that fusion-relevant He generation rates may produce a further increase in the **DBTT**[36]) a reduction in the upper temperature limit. However, ferritic-martensitic steels appear to be very resistant to helium embrittlement, thanks to their bulk matrix densities.[36,48]. In figure 1.14 the windows temperature for the most common structural materials proposed for fusion reactors are summarized.[49]

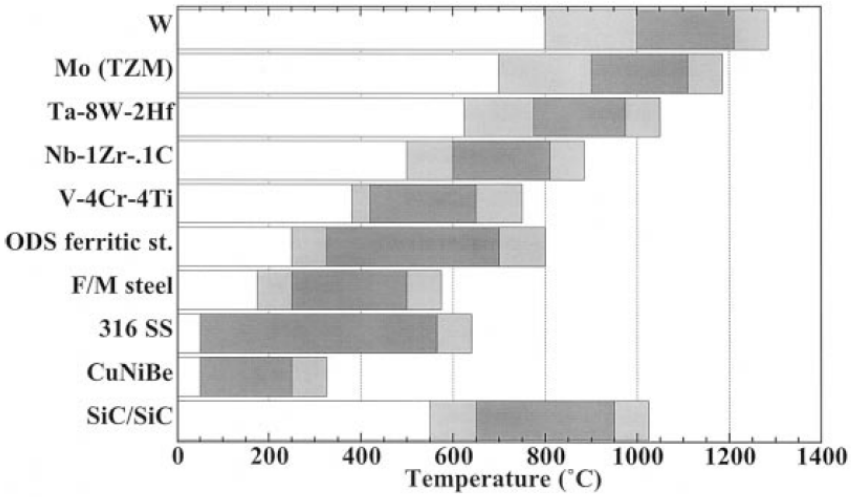

Figure 1.14: Operating temperature windows considering **radiation damage** and **creep considerations** for refractory alloys, steels alloys (austenics and ferritic-martensitics), ODS and SiC and Copper alloys. The light shaded regions on either side on the dark horizontal bands are an indication of the uncertainties in the temperature limits.[49]

	Li	**eutectic Pb-Li**
F-M steels	550-600°C [51–54]	450°C [51, 52, 54, 55]
Mo alloys	above 1300°C [56, 57]	600°C [58]
W	above 1300°C [56]	600°C [58]
SiC	550°C [59–61]	above 800°C [61]

Table 1.3: Maximum operating temperature of structural metal alloys in contact with liquid and heavy liquid metals coolants.

Finally, chemical compatibility with the eutectic **Pb-16Li** must be considered. Chemical compatibility issues can reduce the maximum operating temperature limits for breeding blankets structural materials. Chemical incompatibility of iron-based alloys (i.e austenitic and ferritic-martensitic steels) with heavy liquid metals is governed by dissolution of alloy constituents, mainly nickel, chromium and carbon.

Austenic and ferritic-martensitic steels are corroded rapidly (in flow Pb-16Li at 550°C the corrosion rate of Eurofer97 steel is close to 400μm y^{-1}.[50]) at temperature above 450-500°C. In table 1.3 the upper operating temperature limits based on experimental studies of corrosion in heavy liquid metal of the main structural materials are summarized.

Chapter 2

Materials challenge in DEMO relevant condition

2.1 Gaseous diffusion

From a macroscopic point of view the law governing diffusion processes are **Fick's laws**. These laws represent a continuum description and are purely phenomenological. Fick's laws describe the diffusive transport of matter as an empirical fact without claiming that it derives from basic concepts. More detailed physical mechanisms of diffusion in solids media is based on random walk theory and on the atomic interaction mechanisms of diffusion.

In a general description of diffusion in solid, anisotropic media must be considered. In particular, anisotropic media have different diffusion properties in different directions (i.e non cubic single crystals, composite materials, textured poli-crystals and quasi-crystals). Anisotropy affects the directional relationship between the diffusion flux and the concentration gradient. A generalization of Fick's first law is:

$$J = -\mathbf{D}\nabla\mathbf{C} \tag{2.1}$$

Where **J** is the diffusion flux, **D** is the diffusion coefficient (or diffusivity) and $\nabla\mathbf{C}$ is the concentration gradient. This equation imply that the diffusion flux and concentration gradient usually point in different directions. For anisotropic media diffusivity **D** is a tensor. Furthermore, as a consequence of the irreversibility behavior of process (Onsager's reciprocity in a thermodynamic point of view) the diffusivity tensor is symmetric, takes the form of orthogonal principal axes matrix:

$$\mathcal{D} = \begin{pmatrix} D_1 & 0 & 0 \\ 0 & D_2 & 0 \\ 0 & 0 & D_3 \end{pmatrix}$$

The majority of experiments for measurements of diffusion coefficients and diffusion flux are designed in such a way that the flow is one-dimensional and materials are substantially isotropic. In this condition if a concentration gradient exists only in one direction and both C and $\frac{\partial C}{\partial x}$ are everywhere independent of the other coordinates. Then, the Fick's first law can be written as:

$$J = -D\frac{\partial C}{\partial x} \tag{2.2}$$

The diffusion flux J is expressed of moles traveling a unit area per unit of time $[mol\ m^{-2}\ sec^{-1}]$. Thus the diffusivity D has the dimension of quadratic length per time $[m^2\ sec^{-1}]$.

In the time-dependent case, i.e when the diffusion flux at every point varies with time, combine Fick's first law with a materials balance is needed. In one-dimensional case, considering an interval x and $x + \Delta x$, materials balance can be define as:

$$J(x) - J(x + \Delta x) = \text{accumulation (or loss) rate} \tag{2.3}$$

For infinitesimal size of the interval the equation 2.3 can be written in infinitesimal form as:

$$\frac{\partial J}{\partial x} = -\frac{\partial C}{\partial t} \tag{2.4}$$

Equation 2.4 is denoted as the **continuity equation**.
Combing equations 2.2 and 2.4:

$$\frac{\partial C}{\partial t} = -\frac{\partial}{\partial x}(D\frac{\partial C}{\partial x}) \tag{2.5}$$

Equation 2.5 is named **diffusion equation** or **Fick's second law**. From a mathematical point of view diffusion equation is a second order partial differential equation. In general, D depends on concentration, which is, for example, the case when diffusion occurs in a chemical composition gradient and it cannot be solved analytically. If the diffusivity is independent of concentration, which is the case for tracer diffusion in chemically homogenous systems (the case of the experiments describe in this work) or for diffusion in ideal solid solutions equation 2.5 can be written as:

$$\frac{\partial C}{\partial t} = -D\frac{\partial^2 C}{\partial^2 x} \tag{2.6}$$

2.1.1 Random walk and atomic jump process

Hopping motion of atoms or molecules is an universal feature of diffusion process in solid media. This paragraph, introduces the fundamental of random walk theory and atomic jump process. From a microscopic point of view, diffusion occurs by the **Brownian motion** of atoms or molecules inside the media. Most solids are crystalline and diffusion occurs by jumps in a lattice. Diffusion in solids results from many **displacements, R**, of the diffusing particles. In a general description of the jumps process, the total displacements **R** of a particle is composed of many individual displacements r_i as shown in figure 2.1.

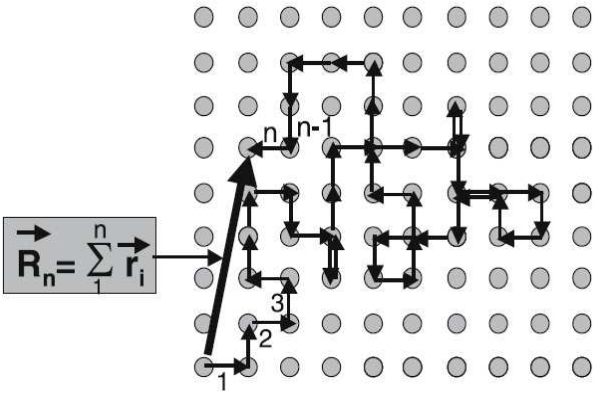

Figure 2.1: Expample of a jump process on a lattice[62]

In a sequence of n jumps is define as follow:

$$\mathbf{R} = \sum_{i=1}^{n} r_i \tag{2.7}$$

Considering a **distribution function** $W(\mathbf{R}, \tau)$, denoting the probability that after a time τ the diffusion particle will have traveled a path with an r-projection $\mathbf{R}$, the one-dimensional case the concentration C in a position x at the time $t + \tau$ is given by:

$$C(x, t + \tau) = \sum_{X} C(x - X, t)W(x, \tau) \tag{2.8}$$

For small values of τ end by Taylorâs expansion concentration C is can be written as:

$$\frac{\partial C}{\partial t} = -\frac{\langle X \rangle}{\tau}\frac{\partial C}{\partial x} + \frac{\langle X^2 \rangle}{2\tau}\frac{\partial^2 C}{\partial x^2} \tag{2.9}$$

Where the right-hand side of the equation 2.9 correspond to a drift term and the second one to the diffusion term. Thus, in absence of driving force $\langle X \rangle = 0$ and equation 2.9 reduces to Fick's second law with a diffusion coefficient:

$$D_x = \frac{\langle X^2 \rangle}{2\tau} \tag{2.10}$$

Equation 2.10 relates the **mean square displacement** $\langle X^2 \rangle$ with the pertinent component, D_x, of the diffusion coefficient. In an isotropic media the displacement in all direction x, $, y$ and, z are the same, giving diffusion coefficient equal to:

$$D_x = \frac{\langle R^2 \rangle}{6\tau} \tag{2.11}$$

Equation 2.11 is denote as **Einstein-Smoluchowski relation**.

Expanding the **mean square displacement**, $\langle R^2 \rangle$, more in detail the equation 2.7 becomes:

$$\langle R^2 \rangle = \sum_{i=1}^{n} \langle r_i^2 \rangle + 2 \sum_{i=1}^{n-1} \sum_{j+1}^{n} \langle r_i r_j \rangle \tag{2.12}$$

The first term contains squares of the individual jump lengths only. The double sum contains averages between jump i and all subsequent jumps j . In a random walk executes in a sequence of jumps in winch each individual jump is indipendent of all prior jump (*Markov sequnce or uncorrelated random walk*)the double sum in equation 2.12 is equal to zero. These terms contain memory effects also denoted as **correlation effects**. Thus, equation 2.12 without correlation becomes:

$$\langle R^2 \rangle = \sum_{i=1}^{n} \langle r_i^2 \rangle \tag{2.13}$$

After a number of jumps, for example in a perfect crystal lattice, the probability distribution for an atom will be a Gaussian, centered on the origin with a mean square displacement:

$$\langle r^2 \rangle = 6 D_t t \tag{2.14}$$

Where D_t is the tracer diffusivity. Considering the mean residence time τ on a site and a mean square jump length $\langle d^2 \rangle$ diffusivity can be written as:

$$D = \frac{\langle d^2 \rangle}{6\tau} \tag{2.15}$$

Considering a Bravais cubic lattice, diffusivity for a jump length d and lattice parameter a can be defined as:

$$D = a^2 \Gamma \tag{2.16}$$

Where Γ is the **jump probability per unit if time** toward a given site.
In a general description random walk is driven by several atomic mechanisms which are not free of memory effects. In fact, diffusion in solids is often defects mediated. Here are listed the most important diffusion mechanisms:

- Interstitial mechanism
- Vacancy mechanism
- Interstitialcy mechanism
- Interstitial-substitutional exchange mechanism

In this case when a correlation occurs the equation 2.16, that considers a perfect lattice, must be replace by:

$$D = f a^2 \Gamma \tag{2.17}$$

Where f is correlation factor (depending on lattice structure and geometrical parameter). Usually, an Arrhenius law holds for the jump rate Γ:

$$\Gamma = \nu^0 exp(-\frac{\Delta G}{k_b T}) \tag{2.18}$$

Equation 2.18 suggest how jump processes are promoted by thermal activation. As mentioned above, an atom moves into a neighbouring site, which could be either a neghbouring vacancy or an interstitial site.

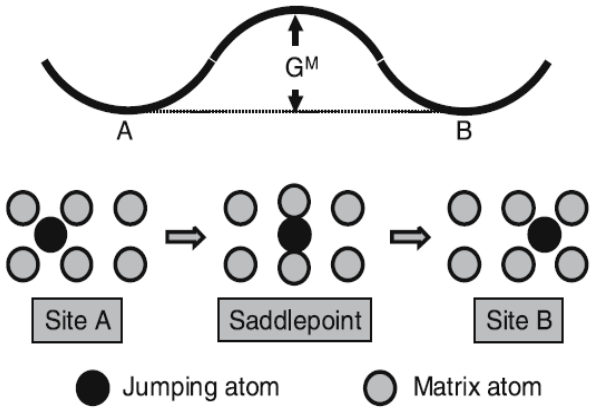

Figure 2.2: Diffusion black atom moves from an initial configuration (site A) to final configuration (site B) moving through a saddle-point configuration.[62]

The jumping atom has to squeeze between intervening lattice atoms as shown in Figure 2.2. Thermal energy, k_BT, induce oscillation of diffusion atoms around their equilibrium positions. These oscillations are not large enough to overcome the energy barrier,G^M, and the atom turns back to its initial position. Occasionally, large oscillation result in a successful jump of diffusing atom. More in detail G^M denoted the **Gibbs free energy** of migration of the diffusion atom. Gibbs free energy can be written as:

$$G^M = H^M - TS^M \tag{2.19}$$

Where H^M is the **enthalpy of migration** and S^M is the **entropy of migration**.[63–72]

2.1.2 Diffusion mechanisms

As described in Sect. 2.1.1 the hopping motion of atoms is a common feature of diffusion processes in solids. In some cases atomic jump processes are completely random (e.g if the solid is a single crystal free of defects), in others correlation between subsequent jump is involved. The latter is the case when jump is driven by atomic defects in solids. Real solids contain defects which may **trap** diffusion atom in a variety of sites (differently from other atoms dissolved in solids, the rapid diffusion of hydrogen, even at low temperatures, allows the trapping to occur at much lower temperatures than any other dissolved atom).

Interstitial mechanism

Generally diffusion atoms are considerably smaller than solid atoms and diffusion atoms can be incorporated on interstitial sites of the host lattice. An interstitial diffusion atom can diffuse by jumping from one interstitial point to one of its neighbouring points. Interstitial diffusion goes through saddle-point configurations. In this configuration neighbouring solid atoms must move aside to let the diffusion atom through. The result, when the jump is completed, is no permanent displacement of the solid atoms remains. Figure 2.3 shows the diffusion mechanism.

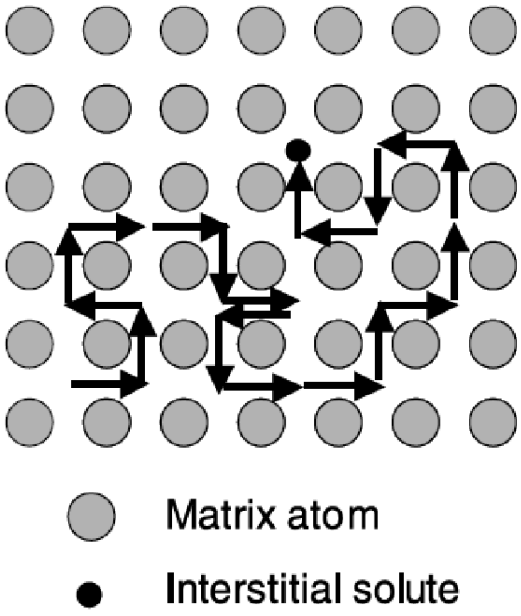

Figure 2.3: Interstitial diffusion mechanism in a no-defect lattice.[62]

Interstitial mechanism is also known as **direct interstitial mechanism**. In fact, no defect is needed to promote diffusion atoms jumps. This mechanism is relevant for diffusion of small atoms such as H, C, N and O in solids.

Interstitialcy mechanism

Interstitialcy mechanisms are collective diffusion mechanism because at least two atoms move simultaneously. This kind of mechanism occurs when diffusion atoms is nearly equal in size to the solid atoms. Both diffusion and solid atoms move in unison, the diffusion atom replaces an atom on a substitutional site, which then itself replaces a neighboring solid atom. Interstitialcy mechanism defines the simplest way of **self-interstitial** atoms to diffuse. In general, interstitialcy diffusion has fairly high formation enthalpies compared to defects, thus is negligible for thermal diffusion in solids. However, Interstitialcy diffusion of self-interstitial atoms is important for **radiation-induced diffusion**. When a solid is irradiated by meas energetic particles (e.g protons, neutrons, heavy ions and electrons) solid atoms are knocked out from their lattice positions. The knocked-out atoms leave behind a vacancies. The atoms themselves are deposited in the lattice to form self-interstitial atoms forming **frenkel pairs** athermally. Finally, self-interstitial play a fundamental role in the diffusion of doping element in silicon.

Vacancy mechanism

Diffusion atom is said to diffuse by vacancy mechanism, when it jumps into a neighbor vacancy. Vacancies are define as thermally induce defects in metal and ionic solids and represent the dominant diffusion mechanism. Generally, each atom of solid moves through the lattice by making a series of exchanges with vacancies, which from time to time are in its vicinity. In some conditions diffusion can also occur by means of aggregates of vacancies (called di-vacancies, tri-vacancies ext.), which concentration rise more rapidly and may became significant at high temperatures.

Interstitial substitutional exchange mechanisms

A diffusion atom diffuses by interstitial mechanism can dissolve in solid lattice on both interstitial and substitutional sites. If the change involves vacancies, $B_i + V \rightleftharpoons B_s$, the mechanism is named **dissociate mechanism**.
If the change involves self-interstials, $B_i \rightleftharpoons B_s + A_i$, the mechanism is named **kick-out mechanism**. Figure 2.4 shows the diffusion mechanism.

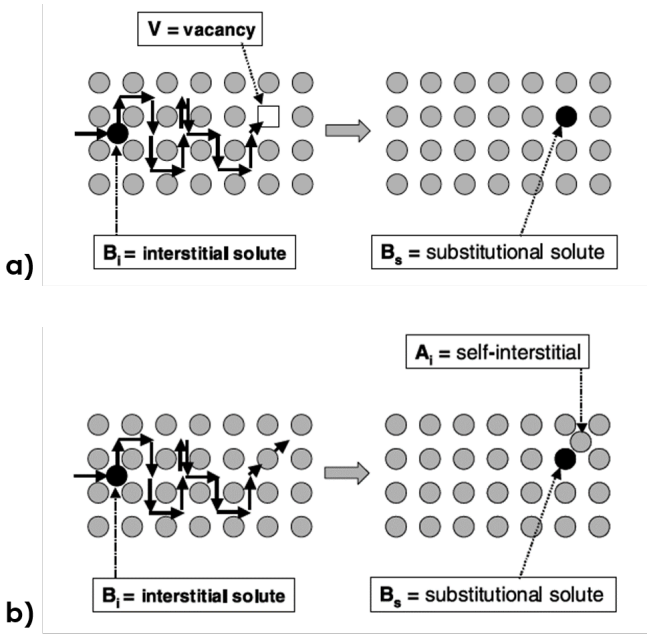

Figure 2.4: Interstitial substitutional exchange mechanism diffusion. (a) Dissociative mechanism. (b) Kick-out mechanism.[62]

Trapping

Defects in solids can be work as a **trap** for diffusion atoms because the interaction with defects is higher than the interaction with solids atoms. In general, trapping sites are voids, grain boundaries, impurity atoms, dislocations and self-trap present in the solid. Historically, trapping of diffusion atoms has been interest on many striking mechanical effects in metals and steels. Hydrogen, thanks to its rapid diffusion in metals, even at low temperatures, allows the

trapping to take place at much lower temperatures than of any other diffusion atoms. Furthermore, the presence of trapped hydrogen atoms are associated to the **embrittlement** of many steels and metals and the retention at high temperatures in structural materials.[63–72]

2.1.3 Isotope dependence

Considering two isotopes a and$b$ with masses m_a andm_b respectively, they have different diffusivity in the same solid. According to the classical theory, Einstein's model for the vibration frequencies of atoms in a solid describe a crystal as a set of independent harmonic oscillators. Characteristic vibration frequency ν^0 is inversely proportional to the square root of the mass of the diffusion atom and the activation enthalpy is mass independent:

$$\frac{D_a}{D_b} \propto \frac{\nu_a^0}{\nu_b^0} \propto \frac{\sqrt{m_a}}{\sqrt{m_b}} \tag{2.20}$$

Thus, heavier species diffuse more slowly as shown in figure 2.5 for hydrogen isotopes.

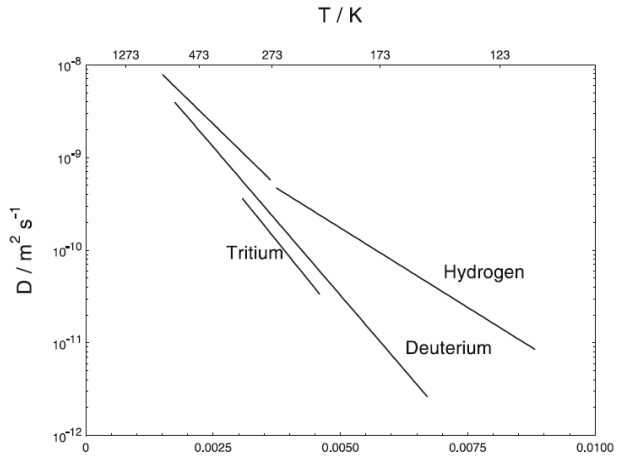

Figure 2.5: Diffusion of H, D, and T in Niobium. According to the equation 2.20 tritium has the lowest diffusivity.[62]

The assumption that activation enthalpy of isotopes are mass independent is well justified, since the barrier for an atomic jump is determined by the electronic interaction and not by the masses of the nuclei. This is only true at high temperature and for atoms heavier than Lithium. For lighter atoms at sufficiently low temperature, such as hydrogen isotopes, quantum effects, wich take into accounts the discrete nature of hydrogen energy levels (e.g zero-point vibration and tunneling) became relevant.[63–72]

2.1.4 Hydrogen isotopes permeation models

The permeation of hydrogen isotopes through a material usually refers to the net transport of gas from a region of high partial pressure to a region of low partial pressure.
Among the different techniques to measure hydrogen isotopes permeation, the one used in this work is the **step change method** in **continuous flow** as describe in chapter 4 in PERI II

section. Three basic processes occur in hydrogen isotopes permeation process (as shown in figure 2.6):

- Chemisorption, hydrogen molecules dissociate on the solid surface providing adsorbed atoms which may diffuse into the solid.
- Diffusion phenomena, hydrogen atoms move through the solid e/o membrane.
- Desorption, diffused hydrogen atoms recombine and are released as hydrogen molecules.

Chemisorption and **desorption** are also known as **surface effects** and **diffusion** as **bulk effect**.

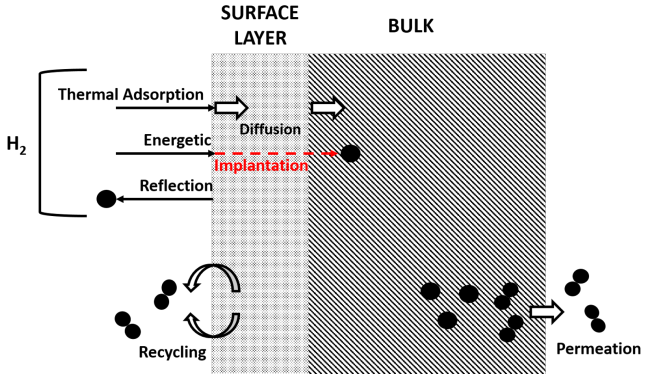

Figure 2.6: Hydrogen-Material interactions.

Generally, oxidized or contaminated surfaces tend to increase the importance of the surface effects controlling the permeation process in **surface-limited permeation**. Moreover, if the thickness of a sample or the pressure of a gas in contact with the membranes is reduced enough, the permeation rate will tend to the surface-limited condition. Conversely, for a thick sample at sufficiently high pressure, permeation will be **diffusion-limited**.

Diffusion-limited model

In diffusion-limited condition the **characteristic time** of the surface effects is negligible compared to the time of the diffusion through the solid. Considering a membrane with thickness d and diffusion coefficient D that initially does not contain dissolved hydrogen. At the time $t = 0$ one side is pressurized with hydrogen at pressure p_h setting up the hydrogen concentration at $c(d) = c_0$. Thus, the initial boundary conditions are:

$$\begin{aligned} c &= 0 \quad 0 < x < d \quad and \quad t = 0 \\ c &= c_0 \quad x = d \quad t > 0 \\ c &= 0 \quad x = 0 \quad t > 0 \end{aligned} \tag{2.21}$$

The general solution of the diffusion equation, equation 2.9 is given by:[73]

$$c(x,t) = c_0\left(1-\frac{x}{d}\right) - \frac{2c_0}{\pi}\sum_{n=1}^{\infty}\frac{1}{n}\sin\left[\frac{n\pi x}{d}\right]\exp\left[-D\frac{n^2\pi^2}{d^2}t\right] \tag{2.22}$$

Using the Fick's law, equation 2.1 or 2.2, the hydrogen flux from the exit surface as a function of time can be written as:

$$\begin{aligned} J(d,t) = -D\frac{\partial c}{\partial x} &= \frac{Dc_0}{d}\left(1+2\sum_{n=1}^{\infty}(-1)^n\exp\left[-D\frac{n^2\pi^2}{d^2}t\right]\right) \\ &= \frac{DK_s p_h^{\frac{1}{2}}}{d}\left(1+2\sum_{n=1}^{\infty}(-1)^n\exp\left[-D\frac{n^2\pi^2}{d^2}t\right]\right) \end{aligned} \tag{2.23}$$

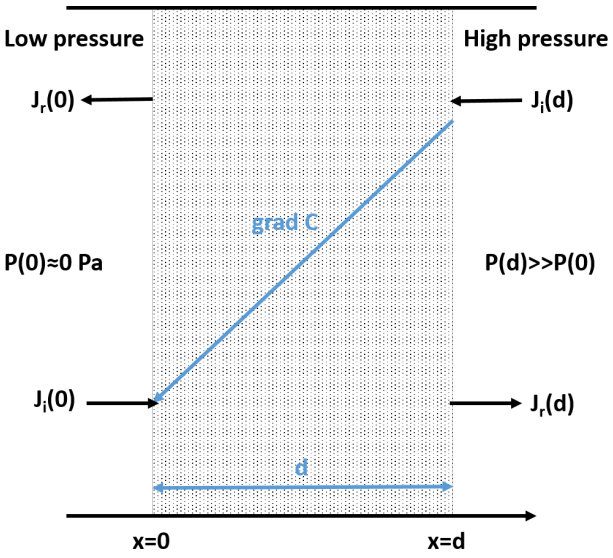

Figure 2.7: Different hydrogen permeation fluxes through a membrane

Considering a thermodynamic equilibrium state, the concentration of dissolved hydrogen atoms at the high, $c_{eq}(d)$, and low, $c_{eq}(0)$ pressure side are given by the Siverts' law (as shown in figure 2.7):

$$c_{eq}(d) = K_s p(d)^{\frac{1}{2}} \qquad \text{High pressure side.} \tag{2.24}$$

$$c_{eq}(0) = K_s p(0)^{\frac{1}{2}} \qquad \text{Low pressure side.} \tag{2.25}$$

At steady-state (i.e. considering $t \to \infty$) equation 2.23 becomes (see figure 2.7):

$$J = \frac{P}{d} p(d)^{\frac{1}{2}} \tag{2.26}$$

P is define as the **permeability** by means of the **Richardson's law** as follow:

$$P = K_s D \tag{2.27}$$

Where K_s and D are Sivert's constant and diffusivity respectively. Since the latter vary with temperature in an Arrhenius manner, than P can be written as:

$$P = P_0 \exp\left[-\frac{E_p}{RT}\right] \tag{2.28}$$

E_p is named **activation energy of permeation**. Since the permeation process depend on surface and bulk effects, activation energy of permeation can be divided in: $E_p = E_d + E_s$.
Finally, the total amount of hydrogen, $Q(t)$, which has permeated after a time t, in term of moles of gas, can be define as:

$$\begin{aligned} Q(t) &= \int_0^t J(d,t')dt' = \frac{Dc_0}{d}t - \frac{c_0 d}{6} - \frac{2c_0 d}{\pi^2}\sum_{n=1}^{\infty}\frac{(-1)^n}{n^2}\exp\left[-D\frac{n^2\pi^2}{d^2}t\right] \\ &= \frac{Pp(d)^{\frac{1}{2}}}{d}t - \frac{Pp(d)^{\frac{1}{2}}}{6D}d - 2\frac{Pp(d)^{\frac{1}{2}}}{\pi^2 D}d\sum_{n=1}^{\infty}\frac{(-1)^n}{n^2}\exp\left[-D\frac{n^2\pi^2}{d^2}t\right] \end{aligned} \tag{2.29}$$

$Q(t)$ is usually obtained experimentally studying the pressure rising during the time considering the **ideal gas law**. At steady-state (i.e. considering $t \to \infty$) equation 2.60 can be written as:

$$Q(t) = \frac{Dc_0}{d} - \frac{c_0 d}{6} = \frac{Pp(d)^{\frac{1}{2}}}{d}t - \frac{Pp(d)^{\frac{1}{2}}}{6D}d \tag{2.30}$$

The values of P and D are obtained by means of the square fitting to the experimantal data for each permeation test using the equation 2.25 or 2.60. It also possible to define P from the steady-state considering the equation 2.61 and diffusivity, D, from the **time lag** (or t_l), the time at which permeation is in regime mode.
Obtained P and D Sivert's constant is determined directly from the Richardson's law 2.58.

Surface-limited model

In surface-limited condition the **characteristic time** of the bulk effects is negligible compared to the time of the surface processes.
Assuming instantaneous diffusion through the bulk (on the time scale of adsorption or recombination processes) any concentration gradient is negligible by meas the diffusion process. Thus, at given time t, the hydrogen concentration c can be considered uniform inside the solid bulk $c(x,t) = c(t)$.

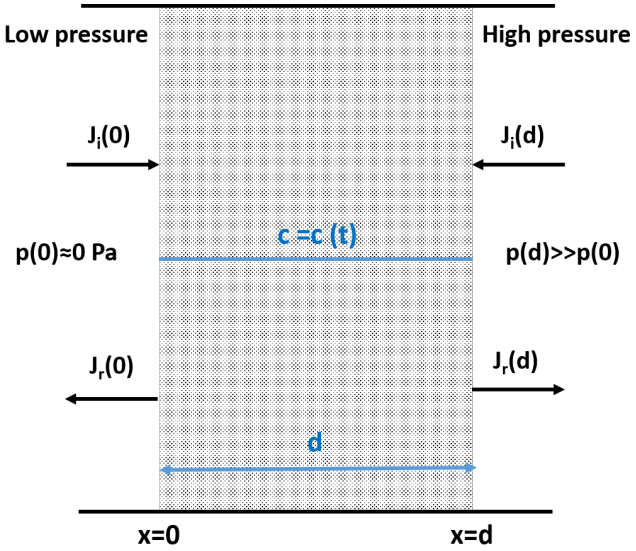

Figure 2.8: Hydrogen permeation fluxes through a solid in the surface-limited condition

As shown in figure 2.8 the incident adsorbed hydrogen flux is taken to be:

$$\begin{aligned} J_i(d) &= (\sigma k_1)p(d) \\ J_i(0) &= (\sigma k_1)'p(0) \end{aligned} \tag{2.31}$$

Where fluxes $J_i(d)$ and $J_i(0)$ are directly proportional to the hydrogen pressure and (σk_1) and (σk_1)' are proportionality constant. In particular, k_1 and k_1' are named **adsorption constant**, while σ and σ' are surface roughness factor defined as the ratio of the real area to the geometric area of the surface.
Due to diatomic nature of the hydrogen gas, the recombination fluxes are related to the quantity c^2 and can be defined ad follow (see figure 2.8):

$$\begin{aligned} J_r(d) &= (\sigma k_2)p(d) \\ J_r(0) &= (\sigma k_2)'p(0) \end{aligned} \tag{2.32}$$

Here, the proportionality constants (σk_2) and (σk_2)' are named **recombination constant**. Let us, $A(m^2)$ and $V(m^3)$ the area and the volume of the solid respectively, the variation of hydrogen concentration with time is given by the balance of hydrogen fluxes as follow:

$$\begin{aligned} V\frac{\partial c}{\partial t} &= A[J_i(d) + J_i(0)] - A[J_r(d) + J_r(0)] \\ &= A[(\sigma k_1)p(d) + (\sigma k_1)'p(0)] - A[(\sigma k_2) + (\sigma k_2)']c^2 \end{aligned} \tag{2.33}$$

The solution of equation 2.33 considering an initial condition $c(t = 0) = 0$ and assuming $(\sigma k_1)p(d) >> (\sigma k_1)'p(0)$ is given by the following equation:[74]

$$\frac{c_f - c}{c_f + c} = \exp\left[-2abt\right] \tag{2.34}$$

where:

$$\begin{aligned} a &= \sqrt{\frac{(\sigma k_1)p(d)}{d}} \\ b &= \sqrt{\frac{(\sigma k_2) + (\sigma k_2)'}{d}} \\ c_f &= \frac{a}{b} \end{aligned} \tag{2.35}$$

Here, c_f define the concentration at the steady-state, then $c_f = c(t \to \infty)$. The flux in the low pressure side is given by $J = (\sigma k_2)'c^2$, then resolving equations 2.34 and 2.35 flux can be written as:

$$J(t) = (\sigma k_2)'c_f^2\left(\frac{1 - \exp\left[-2abt\right]}{1 + \exp\left[-2abt\right]}\right)^2 \tag{2.36}$$

At the steady-state, $t \to \infty$, equation 2.36 can be written as:

$$J = (\sigma k_1)\left[\frac{(\sigma k_2)'}{(\sigma k_2) + (\sigma k_2)'}\right]p(d) \tag{2.37}$$

Finally, the total amount of hydrogen permeated per unit area at time t is given by:

$$Q(t) = (\sigma k_2)'c_f^2 t - \frac{(\sigma k_2)'c_f^2}{ab}\tanh(abt) \tag{2.38}$$

$Q(t)$ can be obtained experimentally by means of the measure of pressure-rise during the time by knowing its effective volume at the operating temperature.[75] At the thermodynamical equilibrium (i.e. $p(d) = p(0)$, $J_r(d) = J_i(d)$, $J_r(0) = J_i(0)$) and considering equations 2.31 and 2.32 so that:

$$\begin{aligned} c_{eq}^2 &= \frac{k_1}{k_2} p \\ &= \left(\frac{k_1}{k_2}\right)' p \end{aligned} \tag{2.39}$$

At the equilibrium, the concentration follows the Siverts' Law, and the relation between the Siverts' and the phenomenological constants is found:

$$\begin{aligned} k_1 &= k_2 K_s^2 \\ k_1' &= k_2' K_s' \end{aligned} \tag{2.40}$$

For an isotropic (i.e. symmetrical) solid, in particular for $(\sigma k_1) = (\sigma k_1)'$ and $(\sigma k_2) = (\sigma k_2)'$, relation 2.37 becomes:

$$J = \frac{\sigma k_1}{2} p(d) \tag{2.41}$$

The other way in which a linear dependance is found in when the permeation in molecular rather than atomic. The latter is the rule for all metals. Then, experimentally if the permeation rate if found to be linear with the hydrogen pressure is a good indicator that the permeation is surface-limited.

Intermediate regime model

In the more general case, a **flux equation**, J, as a function of hydrogen pressure in both regimes and also in the intermediate domain is needed.
The examination of the **intermediate regime** goes through the following steps:

- molecular adsorption and desorption
- surface dissociation and recombination
- diffusion within the lattice

Considering the model in figure 2.9, the hydrogen balance on the upstream and downstream sides is given by:

$$\begin{aligned} J(d) &= J_i(d) - J_r(d) = (\sigma k_1)p(d) - (\sigma k_2)c^2(d) \\ J(0) &= J_r(0) - J_i(0) = (\sigma k_2)'c^2(0) - (\sigma k_2)'p(0) \end{aligned} \tag{2.42}$$

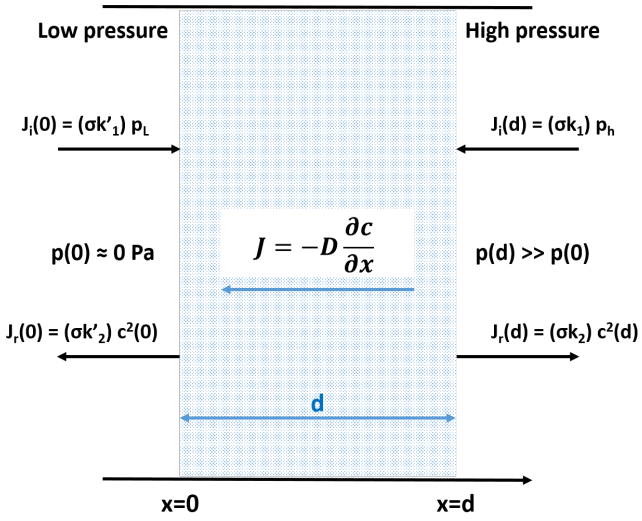

Figure 2.9: Different hydrogen permeation through a membrane

Assuming the case of **symmetrical solid**, $(\sigma k_1) = (\sigma k_1)'$ and $(\sigma k_2) = (\sigma k_2)'$, and the pressure in downstream is negligible compared with the upstream pressure, $p(d) \gg p(0)$, equation 2.42 becomes:

$$J(0) \simeq J_r(0) = (\sigma k_2)c^2(0) \tag{2.43}$$

These conditions are verified during the present measurements. Considering a **stationary state** the hydrogen fluxes in both sides must be the same:

$$J = J(0) = J(d) \tag{2.44}$$

For the first Fick's law, in a metal solid, the diffusion flux can be expressed as follow:

$$J = -D\frac{\partial c}{\partial x} = D\frac{c(d) - c(0)}{d} \tag{2.45}$$

For convenience are take the dimensionless numbers are going to be introduce:

$$\begin{aligned} W &= \frac{\sigma k_1 d}{P} p^{\frac{1}{2}}(d) \\ C(0) &= \frac{c(0)}{c_e q} \end{aligned} \tag{2.46}$$

C defines the **reduced concentration** of hydrogen, while W^2 is the **reduced permeation flux density**. Considering the **Siverts' law** and the equation 2.43, follow that:

$$\frac{J}{J_i} = C^2(0) \tag{2.47}$$

Substitution of equation 2.45 into equation 2.47 by using the definitions of W in the equation 2.46 and **Siverts' law** gives:

$$C^2(0)W = C(d) - C(0) \tag{2.48}$$

Substitution of equations 2.43 and 2.42 back in the equation 2.44, by considering the **Siverts' law** yields:

$$C^2(d) = 1 - C^2(0) \tag{2.49}$$

The last two equations, combined together, give the following relation:

$$W^2 C^4(0) + 2WC^3(0) + 2C^2(0) = 1 \tag{2.50}$$

This is the **general equation** for the **stationary state** permeation through s symmetrical solids. Looking this equation in depth, it is possible to note as follows:

$$\begin{aligned} &\text{If } \ W \ll 1 \ \text{ combining equations 2.50 and 2.47 gives } \ J = \frac{(\sigma k_1)}{2} p(d) \\ &\text{If } \ W \gg 1 \ \text{ combining equations 2.50 with definition of W and C gives } \ J = \frac{P}{d} p(d)^{\frac{1}{2}} \end{aligned} \tag{2.51}$$

Considering $W \ll 1$, define surface effects dominant respect to bulk effects (see equation 2.46), then, as expected, the result is a flux permeation directly proportional to the pressure, as found in **surface limited model** (see eqaution 2.41. Otherwise, considering $W \gg 1$, define bulks effect dominants. As the same way, the result is a flux permeation directly proportional to the square root of pressure as describe by the equation 2.26.[70, 75–77]

Considerations

In a more realistic cases, samples can be composed of two or more layers of different materials of uniform thicknesses d_1, d_2,... d_n with permeabilities P_1, P_2... P_n respectively. A classical approach is to describe the behavior of the system in terms of *permeation resistance* **R**.
Considering a bulk layers the **diffusion-limited regime** can be used. In this case, J represent the analogous of the current and $p^{\frac{1}{2}}$ represent the analogous of the voltage. From the equation 2.26 the permeation resistance of the n^{th} layer, R_n, is define by $R_n = \frac{d_n}{P_n}$. Thus, for a steady-state permeation process hydrogen flux through multilayer solids can be written as:

$$J = \frac{P_{eff}}{d_{tot}} p(d)^{\frac{1}{2}} \tag{2.52}$$

Where P_{eff} and d_{tot} are defined as follow:

$$\begin{aligned} P_{eff} &= \left(\frac{d_1}{\frac{d_1}{P_1}} + \frac{d_2}{\frac{d_2}{P_2}} + \cdots + \frac{d_n}{\frac{d_n}{P_n}} \right) \\ d_{tot} &= \sum_{i=1}^{n} d_i \end{aligned}$$

In a case of an effective permeation barrier (without any defects) of thickness d_1 and permeability P_1 onto a substrate of thickness and permeability d_2 and P_2 respectively, the usual case is define for $\frac{d_1}{P_1} \gg \frac{d_2}{P_2}$ and, in the case of coating barrier, $d_2 \gg d_1$, thus:

$$P_{eff} = P_1 \frac{d_2}{d_1} \tag{2.53}$$

Only in this case will P_{eff} vary in **Arrhenius** manner and permeation flux, J, will be **independent** of d_2.
Unfortunately, this model fails in the permeation barrier, d_1, present **defects** or **cracks** which allow hydrogen to reach the surface of the substrate without permeation (as a **short circuit**) process through the barrier layer itself. As describe in the introduction of the next chapter, this situation is very common, particularly when relatively brittle non-metals or chemical-grown coatings are applied onto the metallic substrate. Even when these defects exist, the steady-state permeation rate may be reduced, but the activation energy for permeation will be the same of uncoated sample.[78]
Only in this situation, the reciprocal of permeation reduction factor, **PRF**, can be interpreted as the fraction of coating area characterized of cracks and defects (assuming that hte coating material itself is highly impermeable).[78] Thus, the hydrogen permeation flux can be written as:

$$J = (1 - \frac{1}{PRF}) \frac{P_2}{d_2} p_d^{\frac{1}{2}} \tag{2.54}$$

During the 70' a model of permeation through **self-passivation** layers named **Strehlow and Savage model** was presented.[79] In this model oxide layers present cracks and defects.

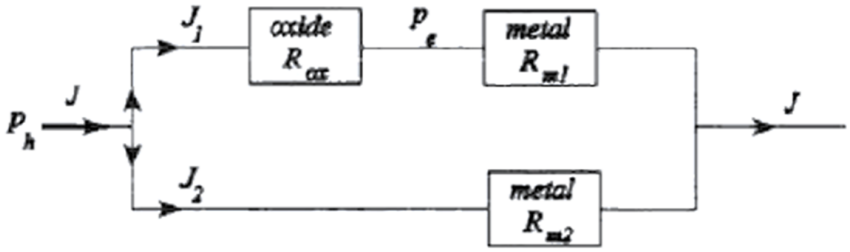

Figure 2.10: Block diagram representation of the **Strehlow** and **Savage model**.[79]

Considering the electrical representation, in figure reffig2.10, the model defines two possible permeation ways through the material. One path considers the intact oxide layer (R_{ox} and R_{m1}) and other path consider the permeation through the cracks (R_{m2}).
Supposing a molecule diffusion mechanism of hydrogen through the intact oxide layer the permeation fluxes, J_1 and J_2, are given by:

$$\begin{aligned} J_1 &= \frac{p_e^{\frac{1}{2}}}{R_{m1}} \\ J_2 &= \frac{p_h^{\frac{1}{2}}}{R_{m2}} \end{aligned} \tag{2.55}$$

For the whole system, figure 2.10

$$J = \frac{1}{R_{m1}} \left[\frac{R_{m1}}{R_{m2}} p_h^{\frac{1}{2}} - \frac{R_{ox}}{2R_{m1}} + \left[\left(\frac{R_{ox}}{2R_{m1}} \right)^2 + p_h \right]^{\frac{1}{2}} \right] \tag{2.56}$$

From the equation 2.56, for $R_{m2} \gg R_{m1}$ the following three cases can be derive:

$$\begin{aligned} J &= \frac{p_h^{\frac{1}{2}}}{R_{m2}} && p_h \text{ very low} \\ J &= \frac{p_h}{R_{ox}} + p_h^{\frac{1}{2}} R_{m2} && \text{intermediate } p_h \text{ value} \\ J &= \frac{p_h^{\frac{1}{2}}}{R_{m1}} && p_h \text{ high} \end{aligned} \tag{2.57}$$

As describe in equation 2.57 and shown in figure 2.11 there is a square root pressure dependance at very low and high pressure range. Instead, for intermediate pressure regime there is a linear pressure dependance, depending on the exact experimental conditions.

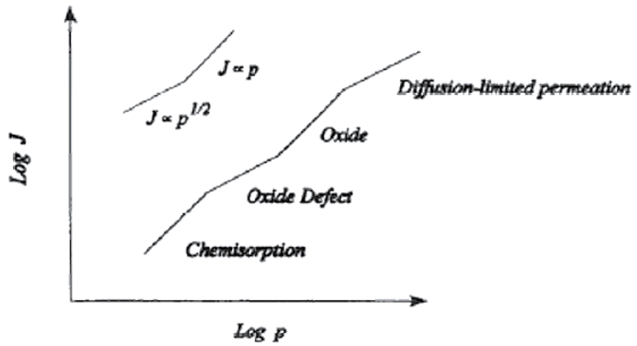

Figure 2.11: Permeation dependance in function of hydrogen pressure in **Strehlow** and **Savage model**.[80]

Although in some cases, the model describes the shape of permeation flux versus pressure in the right manner, it is based on the assumption that hydrogen dissolves as molecular form in oxide, which is unsupported by experimental evidence. [81]
However, considering the surface reaction rates on the oxide covered parts of the material rather than molecular diffusion are the cause of the linear pressure dependance in the intermediate regime it is possible to explain the behavior of permeation flux versus pressure. In most cases, due to the lack of experimental evidence, for the molecular hydrogen permeation through oxides leads to consider the permeation of atomic hydrogen through a solid, limited by surface reaction rates at low pressure.

2.2 Corrosion in Heavy Liquid Metals

Coolants with special properties are required for use in **advanced nuclear conversion systems** such as fast nuclear fission reactors and fusion reactors. Since the rate of power production in these systems is significantly higher than the current generation thermal reactors, coolants with high heat transfer coefficients are required. Since the working temperatures of these advanced nuclear energy system are high, their coolants should have high liquidus range so that the system operates at low pressures. **Liquid metals** with high thermal conductivity, high boiling point and adequately high specific heat meet this heat transfer requirement. Lithium in its pure form or as low melting point (more probably) Pb-16Li alloy is considered as tritium breeder cum coolant in fusion reactor systems.
Mechanism of corrosion of metals and steels exposed to liquid heavy liquid metals (**HLMs**) are mainly **dissolution** and **oxidation**. The diagram in figure 2.12 shows the two basic corrosion mechanisms: **oxidation-oxide** scale formation and liquid metal **corrosion-dissolution** attack[82].

The chart may be generalized to most heavy metals and it gives an overview of the corrosion behavior as a function of oxygen concentration. Above $10^{-6} at.\%$ oxygen concentration, corrosion is mainly caused by oxidation of the steel surface. The oxide film acts as protection layer against dissolution. Finally, the main parameters affecting matals degradation by HLMs

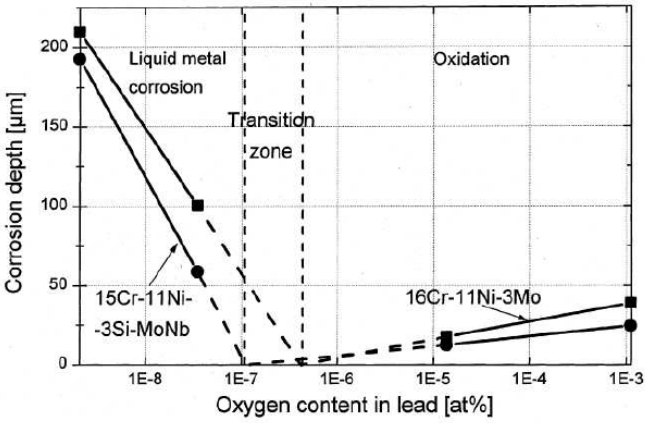

Figure 2.12: Corrosion behavior of steel in flowing lead after 3000h at 550Â°C. Mainly the oxide layer formed on the steel surface is Me_3O_4.[82]

interaction are:

- Solubility of metallic and non-metallic elements in hot liquid metals.
- Chemical composition of steel alloys.
- HLMs hydraulic parameters.
- Mechanical stresses.
- High temperature.
- Thermal stresses (induced by temperature gradients).
- Oxygen content in HLMs.

2.2.1 Solubility of metallic and non-metallic alloys elements

Because the main steel components (e.g. **iron**, **chromium** and **nickel** play an important role concerning dissolution processes, **solubility** of alloys elements at high temperature is a fundamental parameter related to steels corrosion issues in HLMs. In generally, the solubility of metals in liquid metals and metal alloys is define by the saturation concentration C_s that is correlate with temperature, according to Arrhenius' law:

$$\ln C_s = A - \frac{B}{T} \tag{2.58}$$

Where A and B are constants depending on the system obtained experimentally. More in detail stand for **system entropy** and **vaporization heat** respectively.[83] A lot of work has been done studying the solubility of element of nuclear grade steel for fast fission reactors. Figure 2.13 shows the solubility of some steel elements in liquid lead. Figure 2.13 indicates that solubility grows as temperature increases, in particular the use of austenitic steels is avoided for temperature over 723K/773K.[84]

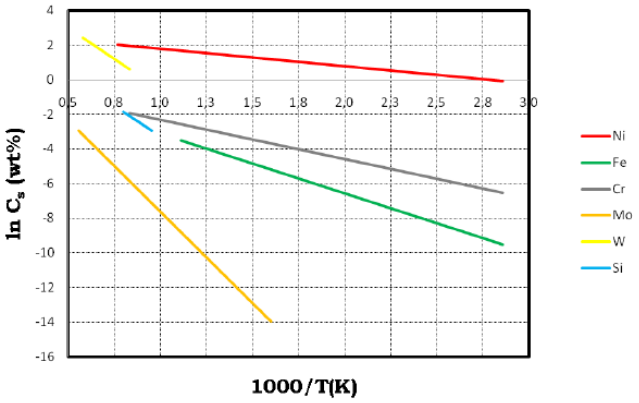

Figure 2.13: Sulubility chart of Ni, Fe, Cr, Mo, W and Si in liquid lead. Alloys with high Ni content (e.g. austenitic steels) are not suitable for HLMs systems.[84]

Oxidation phenomena

Oxygen concentration in HLMs play a fundamental role in corrosion mechanism. The concentration it must be high enough to allow the formation of protective oxide layers, but low enough to guarantee that the precipitation of HLMs oxides do not occur.
As introduced previously, when an oxide layer forms the direct dissolution of steel elements is reduced thanks the low diffusion rate of the alloying elements of steels in the oxides. Thus, the corrosion proceeds through dissociation or transport through oxide layer (which is much slower than direct dissolution).[85] Therefore, oxygen concentration could be a successful corrosion control technique by employing the **self-healing** mechanism up to 823K. Several experimental results report that the structure of oxide layer comprise an external magnetite layer (Fe_3O_4) and an internal Fe-Cr spinel ($(Fe\text{-}Cr)_3O_4$).
In figure 2.14 is shown the main mechanisms tha lead the oxidation of steel in HLMs. The oxidation phenomenon is governed by diffusion mechanisms that occur through the different layers[86, 87].

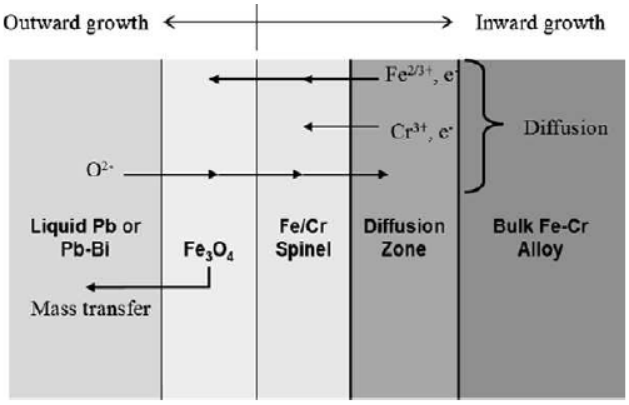

Figure 2.14: Diffusion mechanism through oxide layers.[88]

The magnetite-spinel interface represents the begin of the oxidation process that lies at the original liquid-solid interface: the spinel grows in the same direction of where the bulk of the

steel is, while the magnetite grows toward the HLMs. Chromium should be nearly non-existent in the outer layer, greatest in the spinel layer and back to alloy concentration in the bulk. Iron should be prevalent in the outer layer and scarce in the spinel and diffusion layer, before rising back to alloy concentration in the bulk.[88]
For the foreseen nuclear structural materials, both austenitic and ferritic-martensitic steels develop a duoble oxide layer as just described. The austenitic steels show better resistance to oxidation than martensitic steels, thanks to higher content of chromium (up to 17 wt.%) than with ferritic-martensitic alloys (no more than 8 wt.%).[89] Since the diffusion coefficients of austenitic steels are very low, the whole oxide structure is thinner, compared with the ferritic-martensitic steels at the same conditions[90].In general, it is confirmed that austenitic steels suffer severe corrosion attacks in HLMs at temperature above 773K, while ferritic-martensitic steels form thick oxide scales that periodically spall-off and consequently block forced convention loop. Furthermore, thick oxide layers could hinder heat transfer. Both materials are then recommended for operating temperature below 773K.

Dissolution phenomena

Dissolution of metals elements occur basically in no flow HLM condition or whether the concentration of elements reach the saturation limit. Basically, dissolution in HLMs can take place in three different way[84]:

- **Uniform dissolution**: all the alloying elements are dissolved in the liquid lead.
- **Leaching**: or preferential dissolution, an element is preferentially dissolved by HLMs.
- **Intergranular attack**: local dissolution can be driven by leaching by means the lower activation energies of the atoms at grain boundaries as compared to atoms within grains and by other factors such as penetration along grain boundaries or penetration along specific crystallographic directions.

Dissolution is driven by the driving force as difference between the chemical activities of the solute metals, the solid surface and HLM. Dissolution starts involving the rupture of the bonds between atoms in the solid metal. Subsequently, new bonds between the former and the liquid metals atoms are formed at the solid-liquid interface.[84]
Considering **static conditions** the main driving force is the chemical potential for dissolution -that is, the difference between the chemical activities of the solute metals at the solid surface and in the heavy liquid metal, and can be expressed as follow:

$$C_i = C_0[1 - e^{-\alpha S \frac{t}{V}}] \tag{2.59}$$

Where C_i is the concentration of solute after a lapse of time t, C_0 is the saturation concentration of solute in equilibrium with the solid state, S is the solid surface exposed to a volume V of liquid and:

$$\alpha = \alpha_0 e^{-\frac{\Delta E}{RT}} \tag{2.60}$$

Where α is the effective mass transfer corrosion constant. Here, ΔE is the dissolution activation energy, R is the gas constant and T is the temperature. Equation 2.59 underlines the importance of the solubility of steel elements in HLMs, as it determines the value of C_0. Under isothermal conditions, the dissolution rate decreases with the time, following an exponential law. Dissolution of alloys elements stops when the concentration of the elements in the HLM reaches the saturation value.
The reason why corrosion rates are high in **dissolutive** conditions is that the solubility of the main alloying components of steels in heavy liquid metals is high. The solubility curves for some of these components in lead are plotted in figure 2.13, which shows that solubility increases with an Arrhenius dependence on temperature. The different dissolution mode, listed above, determine two main evolution forms for the corrosion process, namely:

- Uniform corrosion.
- Local corrosion.

In uniform dissolution, all the alloying elements are dissolved in the heavy liquid metals, whereas local dissolution can be driven by leaching, by the lower activation energies of the atoms at grain boundaries as compared to the atoms within grains[1] (**intergranular attack**), and by other factors, as shown in figure. The term **leaching** identifies the preferential dissolution of a specific element. For instance, in the case of austenitic steels, a ferritization of the surface layers is usually observed, owing to the high solubility of Ni and to its consequent leaching [91, 92]. In **flowing condition** the transport of corrosion products from the surfaces to bulk liquid metals is determined by diffusion until reaching the saturation of the liquid phase with corrosion products.
Under flowing condition, the concentration of corrosion products,C_i, after a time t, can be expressed as follow[84]:

$$\frac{dC_i}{dt} = K\frac{S}{V}(C_0 - C_i) \tag{2.61}$$

Where K is a rate constant. Moreover, the flowing liquid can carries corrosion products to other point of the system, where they may deposit. Among external factors, flow velocity is the most important. In fact, HLM flowing over the surface solid accelerate the corrosion process. This phenomenom is called **flow-accelerated corrosion**.[94, 95] Figure 2.16 shows the flow velocity dependency on corrosion. At low speeds, mass transfer controls the corrosion rate. Indeed, in this situation the dissolution rate is higher than mass-transfer rate. Thus, corrosion products concentration near the solid-liquid interface grows until it reaches the saturation value.

When speed exceeds a critical value, the mass transfer rate becomes high enough to transport all corrosion products away from the interface. Thus the corrosion rate is determined by the dissolution/reaction rate and independent of flow speed. For high speed (e.g. highly turbulent

[1] In local corrosion HLM can penetrate into the steel where high defect density zones reach the surface. Local corrosion goes along grain boundaries (2.15-b), specific crystallographic directions (2.15-c), vacancies and pores (2.15-d) and previously formed defects (2.15-e/f).

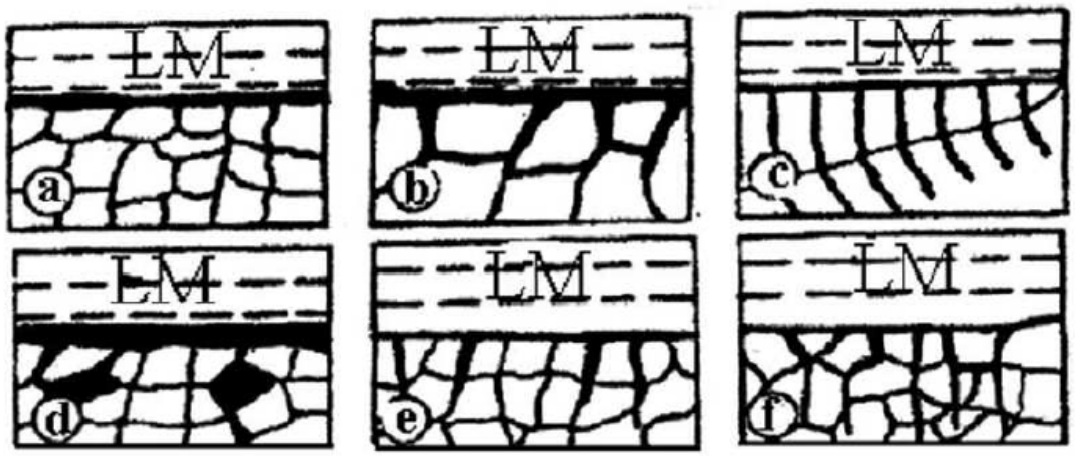

Figure 2.15: corrosion damage of metals in HLM (**LM**=Liquid Metal). a)uniform corrosion; b)penetration along grain boundaries; c)penetration along specific crystallographic directions; d)penetration along vacancies; e-f)penetration along previously formed defects.[93]

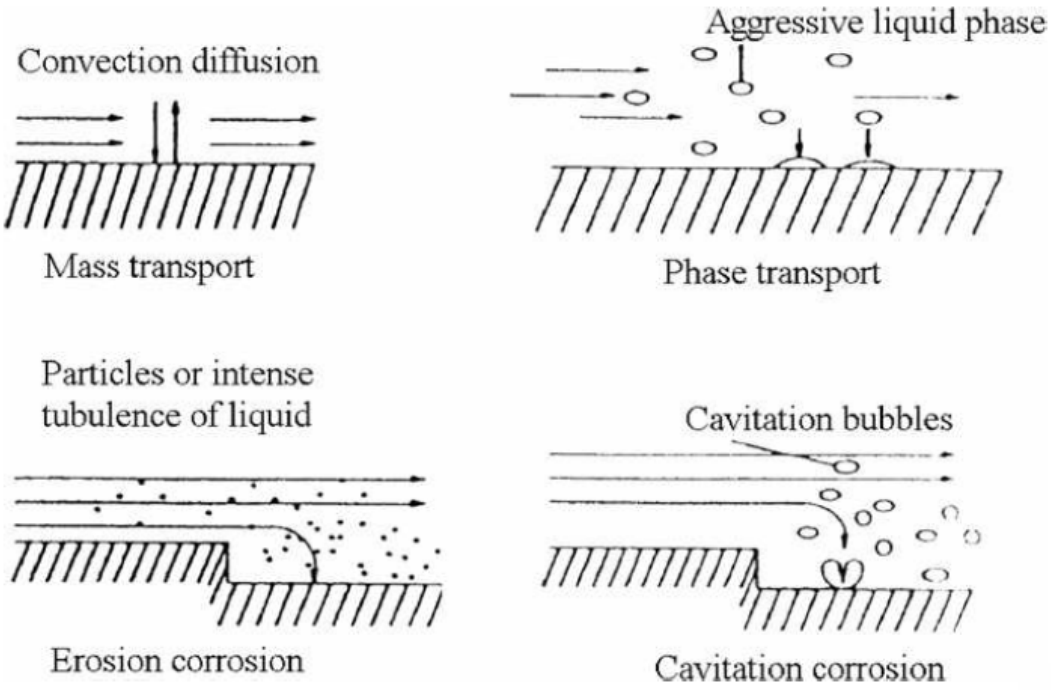

Figure 2.16: Main type of FCA depending on HLM velocity.[96]

flow) the solid-liquid interface is subject to high shear stresses that interplay with the dissolution process. Some cavities appear at the interface and the corrosion rate increases sharply with flow speed. For HLMs, such as lead-lithium, **erosion-corrosion** is likely to occur at moderately high speeds, due to high density.[94, 96].
In multi-phase flows, aggressive particles in the liquid may damage the steel while moving along its surface, or strip the oxide scale, if present. Especially whenever flow direction changes abruptly, as in sudden expansions or elbows, the liquid aggressive particles are thrown against

the steel surface, enhancing wear rate. This mechanism is called **phase transport erosion-controlled corrosion**.[94]
In addition, if cavitation bubbles happen to be present in the flowing heavy liquid metals, they can collapse on the steel surface, creating the so called **liquid metal micro-jets**. This phenomena can induce high stresses in the solid metal, causing localized corrosion fatigue damage and environmentally assisted miucro-fractures of the steel. This phenomena is known as **cavitation-corrosion**.[96]

2.2.2 Loss of mechanical properties

One of the main concerns that comes about with the interaction between steels and heavy liquid metals is the reduction of **surface energy** of the former, what is known as the **Rebinder effect**.[97] The mainly effects responsible for a loss of mechanical properties are namely **Liquid Metal Embrittlement**, (**LME**), and **Liquid Metal Assisted Creep**, (**LMAC**). Moreover, heavy liquid metal interaction, seem to have an influence on the performance of steels under **Low Cycle Fatigue**, (**LCF**).

Liquid Metal Embrittlement

LME refers to a loss of ductility or to a premature brittle failure of a material when placed in contact with HLMs under stress condition. Several investigations have been performed during the last decades, reaching the conclusion that the LME phenomenon is strongly influenced by metallurgical state, hardness and composition of steels, as well as stress and above all, temperature and strain rate.[98–105] Tensile tests have shown that both Ferritic-Martensitic ans Austenitic steels deform plastically in heavy liquid metals almost as in air over the whole temperature range investigated.

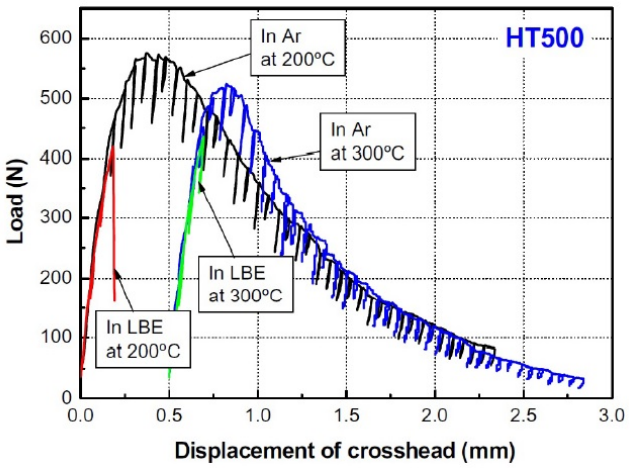

Figure 2.17: Load-displacement curves of Ferritic-Martensitic steel specimens tested in Ar and LBE at 473K and 573K.[99]

Nevertheless, Ferritic-Martensitic steels lost part of their ability to deform plastically after pre-exposure to HLMs under dissolutive conditions at temperature below 693K. The loss in ductility seems to be negligible after ageing in oxidizing conditions.[97] In contrast, Austenitic

steels retain ductility under conditions that are detrimental for Ferritic-Martensitic steels. In figure 2.17 are shown the typical detrimental effect of LME on the load-displacement curves of a Ferritic-Martensitic steels obtained by 3 point bending test in Argon environment and HLMs at 473K and 573K.

Liquid Metal Assisted Creep

Unfortunately, very little data is available on **LMAC**. The most reliable results are in the form of *creep to rupture* tests performed on martensitic steel T91 in flowing lead-bismuth eutectic containing 10^{-6} oxygen, at 823K and uni-axial tensile stress levels up to 220 Mpa as shown in figure 2.18 .[97–106]

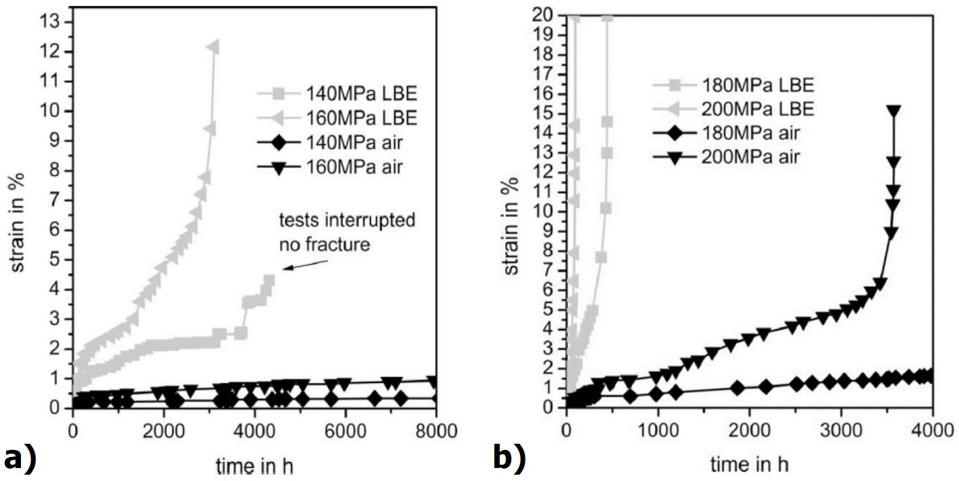

Figure 2.18: Creep-to-rupture tests performed on T91 in **LBE** and air at 823K, (a) 140MPa, 160MPa and (b) 180 and 200MPa.[106]

The time to rupture in HLMs is lower than in air, the strain in the primary stage of creep is higher, and the onsets of the secondary and tertiary stages take place at the earlier time. Therefore, in addition typical creep mechanisms, such as **dislocation gliding**, **vacancy and void formation**, **viscous creep** and **grain boundary sliding**, further **detrimental effects** are introduced by HLMs interaction. These effects are likely related to the consequent dissolution phenomena. A competition between the strain and oxidation phenomena is proposed to account for the observed behavior.[106]

Low Cycle Fatigue

As for **LMAC**, there are not many studies on **HLM**-assisted **LCF**. According to the most relevant data [107–109], there is a weak effect of **HLMs** on the fatigue behavior of 316L under all the tested conditions. On the other hand, there is a reduction of the resistance to **LCF** and an increase in fatigue crack growth in T91. The detrimental effect is amplified on samples pre-exposed to **HLMs** under dissolutive conditions, as also observed for **LME** and **LMAC**. Figure 2.19 shows the **LCF** resistance curves of T91 and 316L steels tested in oxygen saturated **HLMs** [109].

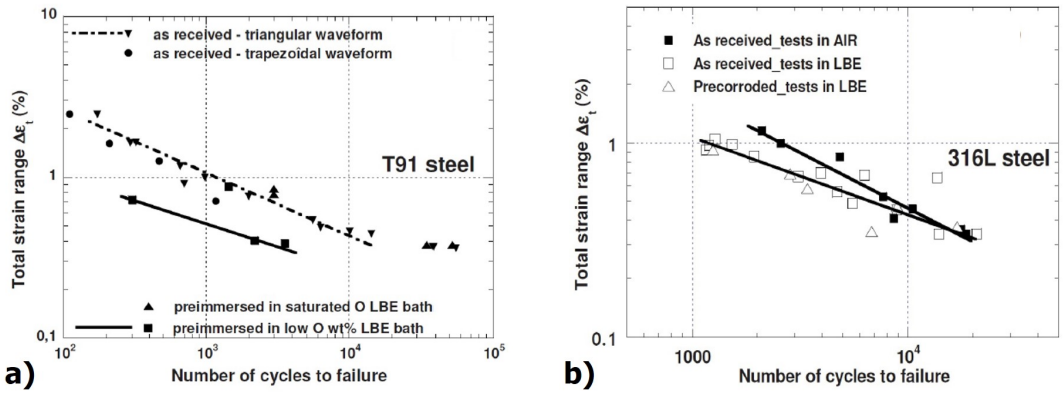

Figure 2.19: Effect of long term exposure in **HLMs** on the fatigue resistance for the (a) T91 and (b) 316L steels.[109]

Chapter 3

Alumina-based coating for DEMO Breeding-Blankets

3.1 Protection strategies for breeding blankets structural materials

Structural materials in nuclear fusion power plant will be exposed to very harsh conditions such as **tritium permeation, corrosion by heavy liquid metals, high dose irradiation** and **mechanical stresses**.
The strongest need in liquid Pb-16Li breeding blanket designs is having effective **barrier materials**, even though **barriers** are also necessary for other blanket and coolant systems. Uncontrolled tritium transport in nuclear fusion power plants can lead tritium inventory build-up in plant, tritium-contaminated effluents, high tritium concentrations in work areas, hydrogen embrittlement of structural metals and more difficult tritium processing. Hydrogen isotopes barriers are necessary to kinetically limit the achievement of isotopic thermodynamic equilibrium through hermetic boundaries. At the same time, structural material must maintain its integrity during the operation. Corrosion in the form of dissolution, intergranular penetration and interstitial transfer to and/or from liquid metal, can result in significant structural material thinning with loss of integrity and mechanical properties. In previous corrosion testing studies on structural materials for the european breeding blanket (**RAFM** steel named **Eurofer 97**) it was shown a strong corrosion attack with a corrosion rate up to 400 μm y^{-1} in flowing Pb-16Li at 823K as shown in figure 3.1.[50, 113, 114]

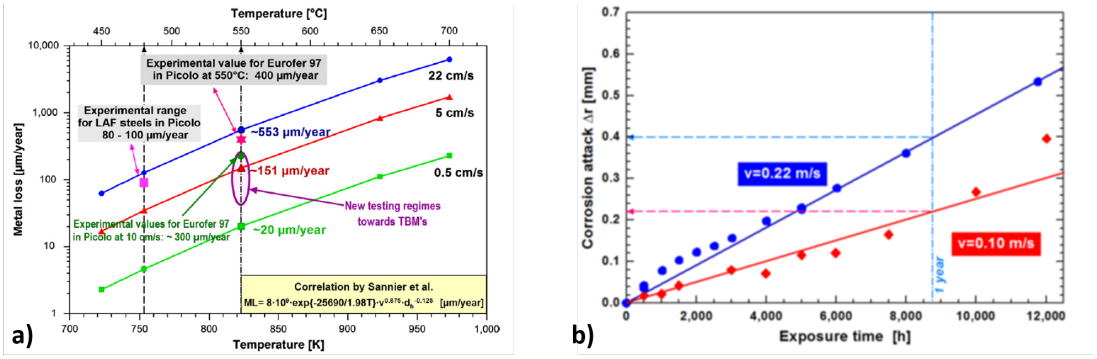

Figure 3.1: a) Comparison of PICOLO test results and calculations of metal loss for 0.5, 5 and 22 cm s^{-1} flow rate by using Sannier's correlation. b) Comparison of PICOLO test in radius reduction of Eurofer97 specimens in long duration tests for 10 and 22 cm s^{-1} at 823K.[114]

Moreover, the hydrogen permeabilities of different materials at the same conditions (e.g. temperature and gas partial pressure) cover a very wide range, as shown in figure 3.2.

Protective layers are the main approach to mitigate these issues, that can be achieved basically as follow:

- Growth of oxide layers.
- Deposition of surface coatings.

In the last few decades the main approach to mitigate materials degradation and tackle the tritium permeation was to produce protective layers by means of the **self-passivation** of the surface. This method consists to favor the in-situ formation of oxides layers (mainly iron-base spinel and chromia) by using or injecting oxygen in the systems. Thanks to its low dissociation

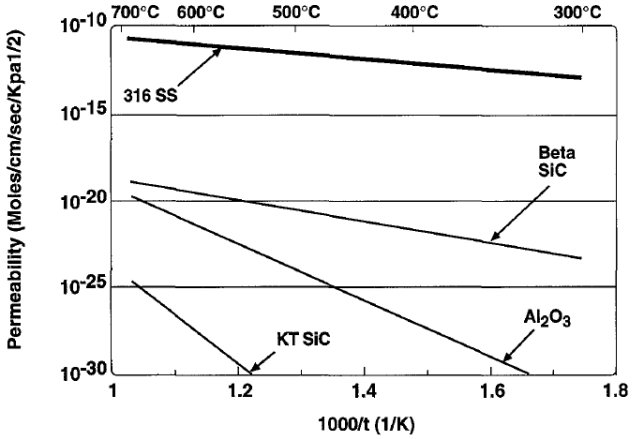

Figure 3.2: Tritium permeability of austenitic 316 stainless steel with those of Al_2O_3 and SiC.[110–112]

pressure, the most common native oxide (forming on the steel surface) is, of course, Cr_2O_3 (or **chromia**). Native metal oxides layers can be formed by heating the steel in the atmosphere (e.g. in presence of oxygen) or under a variety of conditions. It was found that dense, continuous layers consisting of few micrometers of pure chromia was likely to be more effective than much thicker mixed oxides layers or spinels. In fact, chromia provided a reduction in isotopes hydrogen permeation by about two order of magnitude. [115, 116] Unfortunately, the high solubility of **Chromium** in heavy liquid metals (see figure 2.7) makes chromia inadequate as anti-corrosion barrier. [117, 118]

During the 70' and 80' self-passivation technique was enhanced developing **silicon** and **aluminum-rich** bulk alloys. Just as for the bulk Fe-Cr-Si and Fe-Cr-Al systems, small addition of Si or Al to the surface of the steel will favor, by oxidation at high-temperature or by injecting oxygen in the system, a protective scale of $\mathbf{SiO_2}$ or $\mathbf{Al_2O_3}$ retaining the bulk mechanical properties of the standard steel.[119, 120] Oxide layers have interesting protective properties thanks their strong chemical inertia and to the possibility to decoupling the problem of corrosion protection for the low and high temperature range. Several studies on energy formation thermodynamic in **oxygen saturated Pb-16Li** up to 1023K show the stability and meta-stability of the majority of binary metal oxides.[61, 118, 121, 122] Furthermore, the majority of oxides (i.e. alumina, chromia and rare-heart oxides) show interesting properties as hydrogen isotopes permeation barrier.[118, 123–131]

Forcey et al. [123] found that the aluminized layer of 1 mm of thickness on austenitic 316L stainless steel offered a reduction of hydrogen permeation rate up to 4 order of magnitude (in the temperature range of 973-1073 K). The effectiveness of this permeation barrier is attributed to the surface oxide layer consisting of **alumina**.

Although the **self-healing** advantage, intrinsic drawbacks, such as brittleness, non-uniform density, micro-cracks, porosity and the metal dissolution in Pb-Li during the self-passivation process are the greatest limitation.

Similarly to self-passivation technique, the use of **oxide coatings**, deposited onto the structural materials, enable surface functionalization while retaining the mechanical properties of the steel. Several successes have been achieved with heterogeneous **carbide, nitride** (e.g. SiC, TiC, TiN, BN) and **oxide** coatings applied to metals.

There are a large of number of potential coating techniques available, such as: **CVD, electroplating, sputtering process, pack cementation VPS** and **aluminising**.[132–134]
In all cases, **metal oxides** and **rare-earth oxides** have been studied extensively.[123,130,135–154]
Alumina ($\mathbf{Al_2O_3}$), as shown in the charts in figure 3.3, attains the lowest elastic properties mismatch with steel, reaching an excellent compromise in terms of thermo-mechanical behavior.[155]

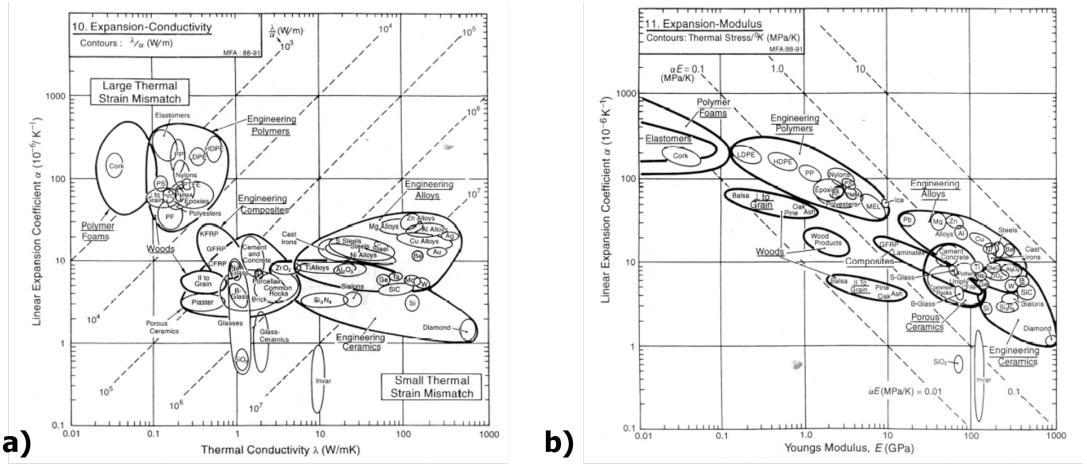

Figure 3.3: (a)The linear expansion coefficient α plotted against the thermal conductivity λ. The contours show the thermal distortion parameter $\frac{\lambda}{\alpha}$. (b) The linear expansion coefficient α plotted against Young's modulus E. The contours show the thermal stress created by a temperature change of 1°C if sample is axially constrained.[155]

Along with its chemical inertia, Al_2O_3 is one of the most promising candidate as coating barrier (i.e. against corrosion and tritium permeation) in DEMO breeding blankets.[61, 113, 117,118,121,122,124,130–134,156–171]

In this framework, the **aim** of the present **Ph.D thesis** can be divided in two main activities:

- testing the **PLD** nano-structured Al_2O_3, in order to provide a statement regarding its feasibility as **tritium permeation barrier** and as **corrosion protection method** in DEMO condition eutectic Pb-16Li.
- Developing of **Atomic Layer Deposition** technique optimizing metal oxides deposition onto stainless steels substrate characterize to complicated geometries (e.g DEMO breeding blanket).

3.2 Pulsed laser deposited Al_2O_3 coating under DEMO relevant conditions

Pulsed laser deposition (e.g **PLD**) is promising and flexible technique that offers valuable means for engineering materials properties at the nano-scale. The mechanism deposition process is deeply described in chapter 5.
Remarkably, PLD process conditions can be tailored to obtain high-quality Al_2O_3 coatings with

a wide range of microstructures, from fully dense and compact to aerogel through hierarchical.[175] Consequently, the deposited films can be hard, moderately hard or even soft. As a matter of fact, PLD grown film morphology can be modified by adjusting the deposition temperature. At room temperature, x-ray amorphous Al_2O_3 is usually observed.[176] Instead, for PLD processing above 500°C a noncrystalline phase of γ-Al_2O_3 is observed.[177] In comparison, reactive magnetron sputtering generally requires higher temperatures to produce similar features, otherwise giving rise to a lower quality product.[178–180] The final choice in the frame of this Ph.D. work is to characterize deeply compact amorphous alumina, grown at room temperature, after a preliminary consideration of the performance by changing the film morphology (i.e. increasing the background pressure). PLD-grown coatings typically reproduce the roughness

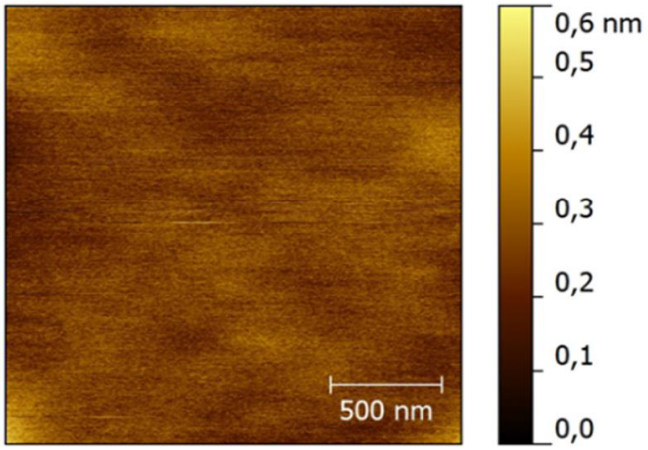

Figure 3.4: AFM topogrphy of an atomically flat Al_2O_3 coating grown on Si wafer (RMS below 0.1 nm.[181]

of the underlying substrate.[181] Measurement at atomic force microscope (or **AFM**) on coated silicon wafer demonstrate that the roughness of the coatings is the same of the underlying substrate with a RMS below 0.1 nm, as shown in figure 3.4.[181] SEM images reported in figure 3.5 confirm the same evidence. The surface is ultra-smooth, with the exception of few submicron-sized defects and droplets. Cross-sectional views of coated steel specimens show that the coatings completely cover the surface and reproduce its roughness. The microstructure of low back ground pressure deposited alumina is compact and fully dense.[182]

The mechanical properties of deposited films have been examined using a combination of nanoindentation and Brillouin spectroscopy.

The loading and unloading curves (i.e maximum load of 50 mN) of the indentation measurements are shown in figure 3.6 Coatings deposited at room temperature attains an unusual combination of compactness, moderate stiffness (such as a metal-like behavior) and significant hardness, resulting in superior plastic behavior. For deposition at high temperature (i.e. 600°C) an increase of stiffness and a significant enhancement of hardness are obtained. The Young's modulus, **E**, and the Poisson's ratio, ν, can be defined through the Brillouin spectroscopy by means of the Ellipsometry-Brillouin-Nanoindentation method (i.e. **EBN**).[182] Mechanical properties are resume in table 3.1 compared with 316L stainless steel and bulk sapphire.

The substrate-coating **adhesion** has been evaluated through **nanoscratch** tests by means of the evaluation of the interfacial bonding strength. In a scratch test, a diamond stylus is scratched across the surface of the coating under continuously increasing load until the coating

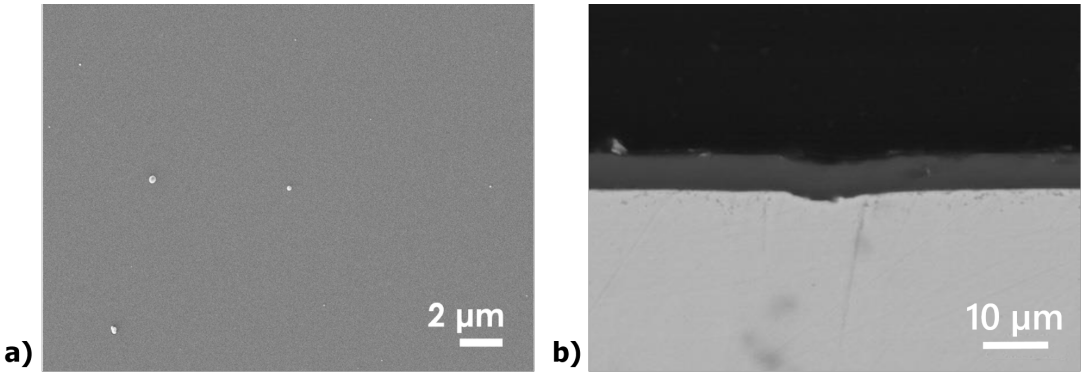

Figure 3.5: a) SEM images showing the surface of as-deposited Al_2O_3 coatings. Droplet coverage is low. b) Cross-sectional SEM view of an as-deposited Al_2O_3 coating on stainless steel. The coating is compact and reproduces the roughness of the substrate. No defects can be found throughout the thickness[182]

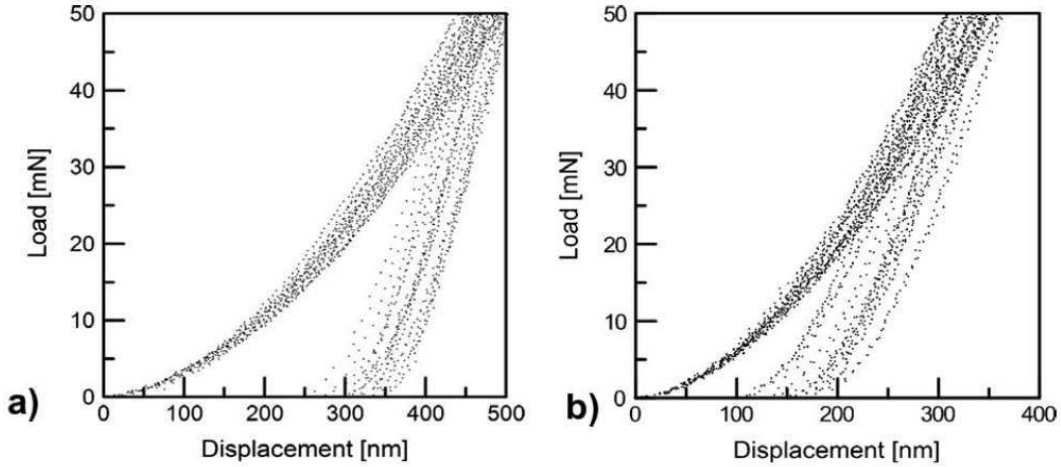

Figure 3.6: Loading and un-loading curves of indentations on steel substrates for coatings grown at a) room temperature and b) $600°C$.[182]

detaches from the substrate. This load is defined as the critical load and provides a qualitative measure of adhesion strength. Under the experimental condition of the PLD-grown Al_2O_3, a critical load cannot be defined (i.e nanoscratch tests did not cause the delamination of the coatings), which exhibit strong interfacial bonding regardless of the deposition temperature. Furthermore, no evidence of major coating fracture or loss of interfacial bonding is observed, neither discontinuities of penetration profiles are found, indicating that no brittle failure occurred.[182] The ratio of **hardness** and **Young's modulus** is a good indicator for describing tribological behavior of coatings. For PLD-grown Al_2O_3, as shown in table 3.1, the H/E is in the range from $0,049$ to $0,091$ depending on deposition temperature. These values are comparable to those of super-hard (i.e. H$\geq$40 GPa) coatings for tribological applications (i.e. nitrides or carbides phase systems, such as Ti-B-N or Ti-Al-B-N [183]), for which the typical H/E ratio varies from $0,05$ to $0,12$. Nevertheless, high values of H/E may not be enough to guarantee a satisfying tribological performance. Under these conditions, the ability of the coatings to dissipate a significant part of the deformation energy becomes crucial.

This ability can be evaluated considering the energy dissipated as a consequence of plastic

	Sapphire	Al_2O_3 at RT	Al_2O_3 at 600°C	AISI 316L
ν	0,24	0,29±0,025	0,27±0,02	0,3
E [GPa]	345	193,8±9,9	277,1 ± 8,6	200
H [GPa]	2,78	10,3±1,0	25,2 ± 1,0	4
H/E	0,059	0,049±0,006	0,091±0,007	0,025

Table 3.1: Mechanical properties of PLD-grown Al_2O_3 deposited at different temperature.[182]

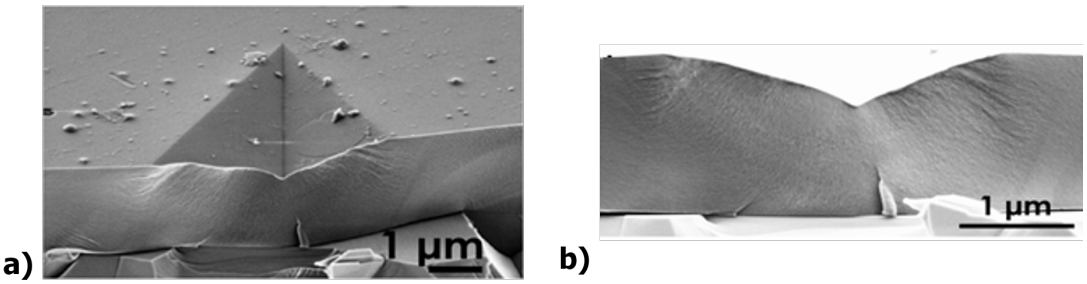

Figure 3.7: Cross-sectional SEM images of nanoindentation imprints on compact Al_2O_3 showing plastic strain through banding in the coating. The absence of cracks in the coating suggest a high fracture strength

strain in respect to the total deformation energy that is measured during nanoindentation. Since, the significant **plastic resources** and the quality of the PLD-grown Al_2O_3 to dissipate a large amount of energy, no signs of cracks and delamination are present even under plastic deformation, as shown in figure 3.7. Having evaluated all these qualities, PLD-grown Al_2O_3 achieves the metal-like mechanical properties, allowing to qualify it as a moderately stiff and ductile ceramic. In respect to **radiation tolerant** behavior, irradiation tests with heavy ions have been performed. PLD-grown Al_2O_3 deposited on austenitic stainless steel substrates have been irradiated in two ion beams of 12MeV Au^{5+} ions and 18MeV W^{8+} reaching an irradiation damage (**dpa**) up to 150dpa.[184] Irradiation induces an amorphous to crystalline transformation resulting in a fully nanograined structure, while extended irradiations induce grain growth and softening in accordance with the Hall-Petch relationship, as resumed in figure 3.8 and 3.9.[184]

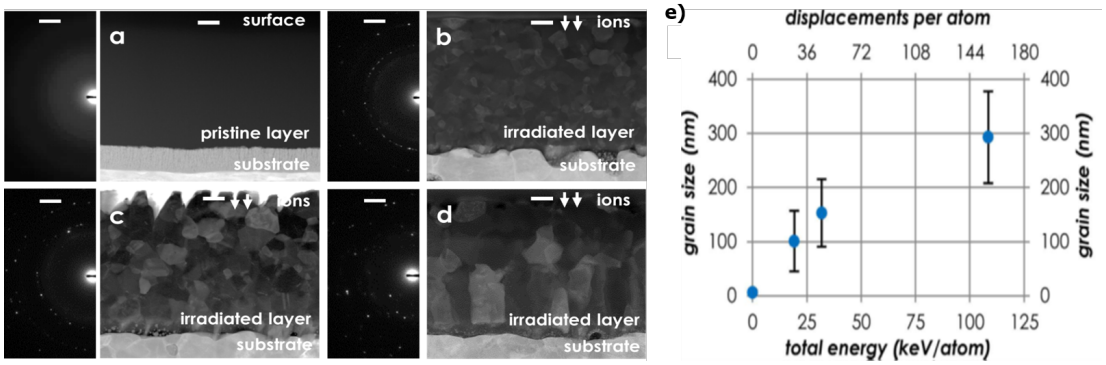

Figure 3.8: ADF-STEM images and DPs showing as-deposited (a) and irradiated Al_2O_3 coating after 20 dpa (b) 40 dpa (c) and 150 dpa (d) at 600°C. e) Grain size growth as a function of total dpa and energy injection.[184]

The Young's modulus increase monotonically, (see figure 3.9), with increasing irradiation

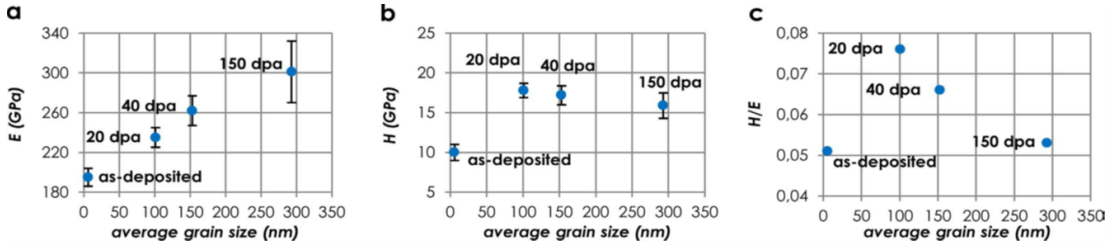

Figure 3.9: Effect of radiation on the mechanical properties of Al_2O_3 coating, namely (a) Young's modulus (**E**), (b) Hardness (**H**), and (c) H/E ratio.[184]

dose, while the ratio H/E increase upon the crystallization and decrease thereafter, with a final ratio H/E close to the initial value. The improvement of H/E at extreme ions irradiations dose due to the energy dissipation mechanism as twinning (during grain growth), and lattice plasticity and localized crystalline-to-amorphous transformation after impact loading.[184] Overall, the finding of these properties underline the capability of PLD-grown Al_2O_3 as coating in a very harsh conditions. Unfortunately, it may not be enough for DEMO breeding blanket, unless the barrier properties against high temperature corrosion (in eutectic Pb-16Li media) and tritium permeation are studied and verified.

3.2.1 Hydrogen permeation tests

As pointed out before, tritium permeation from the breeding zone to the cooling system, through the structural steels, is of course a bottleneck in DEMO development.[117, 157, 172] The final choice in the frame of PLD-grown barrier is to grow Al_2O_3 at different background gas deposition pressures, focusing on optimizing the performance of compact barriers. Typical process parameters are listed below:

- laser pulse energy 410 mJ.
- laser pulse fluence $\sim$ 4 J cm^{-2}.
- pulse repetition rate of 20 Hz.
- background oxygen pressure in the range 0,1-2 Pa.
- base vacuum pressure $\leq$ 5 10^{-3} Pa.
- target to substrate distance of 5 cm.

Resulting deposition rate is $\sim$ 0,85 nm sec^{-1}. In this study, the effectiveness of the coatings is investigated by permeation test, in **continuous flow regime**, in PERI II facility deeply described in Chapter 5. The main goal of the tests is to define the quality factor **Permeation Reduction Factor** (or **PRF**) and the hydrogen **permeation flux** in different conditions. PRF is defined by the ration of hydrogen permeation flux through the **uncoated** sample and hydrogen permeation flux through the **coated** sample:

$$PRF = \frac{J_{h_2}^{uncoated}}{J_{h_2}^{coated}} \tag{3.1}$$

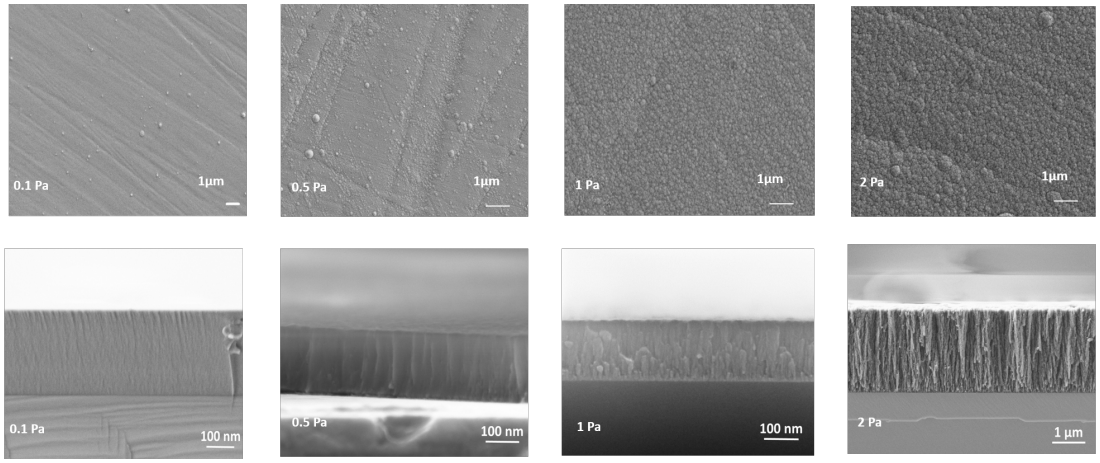

Figure 3.10: Morphology of PLD-grown alumina. Increasing the background pressure increase of porosity is shown

Preliminary tests are focused on the investigation of effectiveness barrier behavior grown in different morphology, as shown in SEM pictures in figure 3.10. The background oxygen deposition pressure selected are 0.1, 0.5, 1 and 2Pa, while the thickness is 5 μm for all samples (an uncoated substrate is used as reference). Substrates are Eurofer97 ferritic-martensitic steel of 52mm of diameter and 0.7mm of thickness. The substrates preparation, mainly cleanliness and roughness of surfaces are mandatory factors for a successful coating deposition. Here, substrates are grounded using SiC paper with increasing grits (180, 400, 800, 1200 and 2400), polished with diamond suspensions (6μm, 3μm and 1μm) and cleaned with an ultrasonic device in ethanol and rinsed in distilled water.

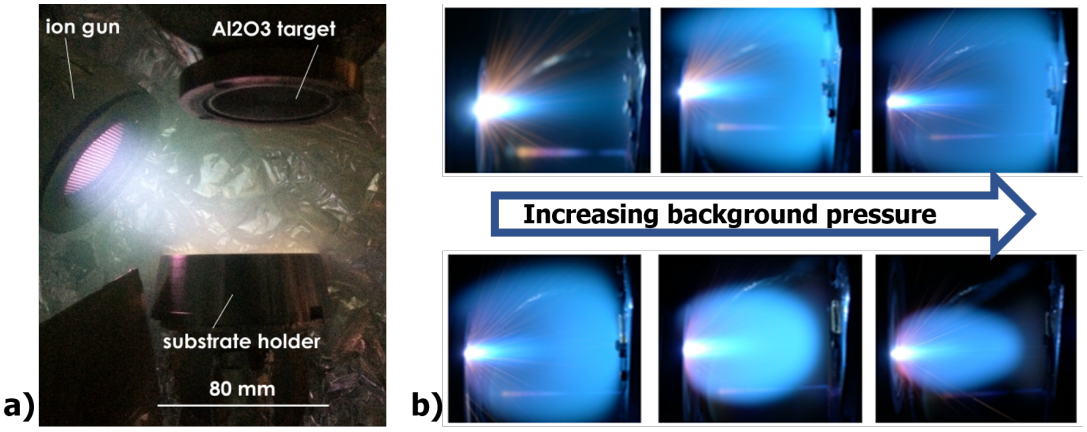

Figure 3.11: (a) Ion-gun cleaning inside the PLD chamber (b) Plasma plume at different background pressure during Al_2O_3 deposition.

Further cleaning was carried out in-situ by pre-sputtering by means of **ion beam** of **Ar plasma** with an ion-gun as shown in figure 3.11(a). Figure 3.11(b) shows a typical plasma plume modification by tuning the background deposition pressure. Samples are mounted in the test section of PERI II facility, dividing the high-pressure section to the low-pressure section as shown in figure 3.12 and deeply described in Chapter 5.
After taking the pressure down to $\sim 10^{-5}$Pa, the high-pressure section is fulfilled of pure hy-

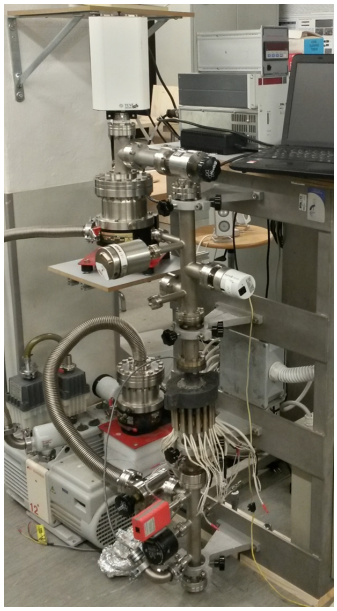

Figure 3.12: PERI II facility in vertical position. Upper part is the low pressure section keeping constantly at pressure in the range of low 10^{-4}Pa. Here a quadrupole mass spectrometer detect the hydrogen concentration during the time. The bottom part is the high pressure section. After a vacuum in order of 10^{-4}Pa is filled by pure hydrogen. In this work a partial pressure of 100mBar is used.

drogen (99,999%) at 100mBar. Coated and uncoated samples (figure 3.13 shows an example) are tested at different temperatures such as 623K, 723K and 823K. After each permeation measurement at a fixed temperature, the coated sample is kept at 873K overnight to release the hydrogen accumulated in the sample. While, the bare sample is kept, even overnight, at 773K.

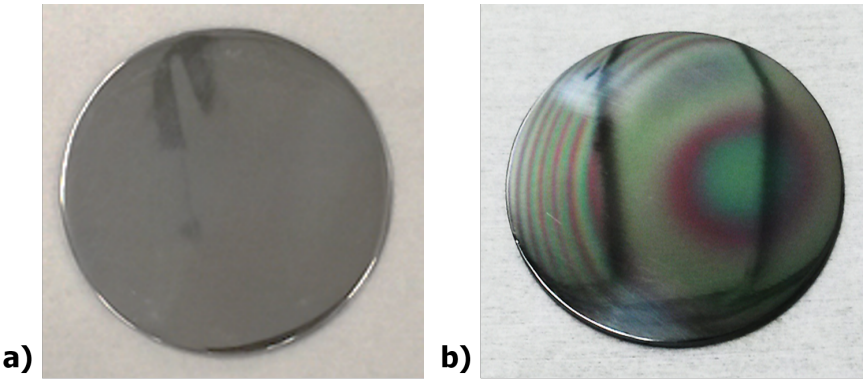

Figure 3.13: Eurofer97 disks, 52mm diameter and 0,7mm thick. (a) Polished bare Eurofer97 disks used as reference (b) 5μm coated at 0.1Pa of oxygen deposition pressure by PLD

The concentration of hydrogen is detected by using a Quadrupole Mass Spectrometer (**QMS** see Chapter 5) in low pressure section. Crude signals are represented by an average ion current collected each cycle (an cycle correspond to $\sim$ 12s of measure collection) as shown in figure 3.14.

As mentioned in Chapter 2, temperature plays an important role in thermodynamic permeation behavior. Increasing the temperature of hydrogen species, makes them interacting with

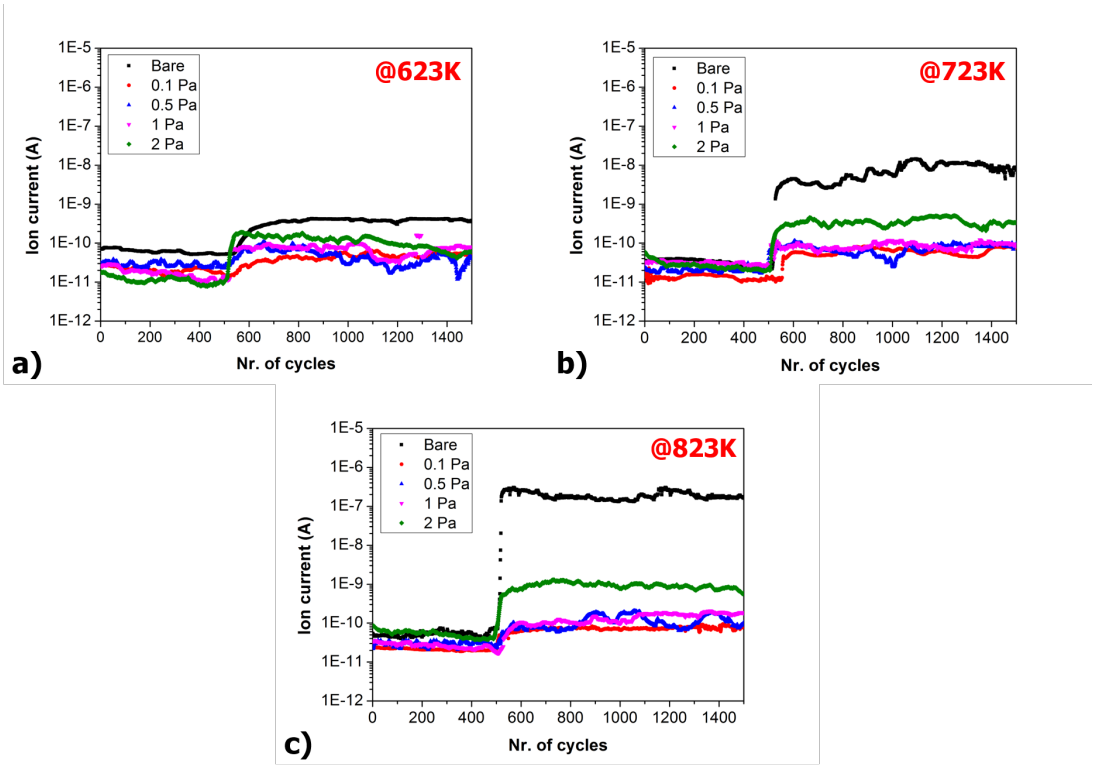

Figure 3.14: Ion current measured at different temperature by QMS for samples coated with 5μm of PLD-grown alumina at different background pressure. After a background measure of 500 cycles pure H_2 is injected at 100mBar.

the samples surfaces, both coated and uncoated, with higher energy, increasing the chance of being adsorbed (hydrogen energy is closer to the activation energy). This behavior is more evident for the bare sample, mainly due to the lower **activation energy**[1]. Looking more in detail, it is possible to note a dramatic ion current detection increase for the sample covered with Al_2O_3 coating deposited at higher background pressure, as shown in figure 3.14.
An ideal permeation barrier must be compact and defect-free in order to maximize the activation energy and avoid the permeation through material lattice defects as explained in section 2.1. Al_2O_3 coatings deposited by PLD at room temperature is mainly amorphous with randomly dispersed nano-domains (see section 3.2). Although, several works showed that crystalline structures of coatings have higher barrier performance than amorphous[123, 125–127, 149], in this work thesis a value near 10^5 of **PRF** is obtained. Moreover, the effectiveness of permeation barrier also depends much on the integrity of the coating. Several investigations show a reduction of PRF up to 10 with even small cracking (around 0.001% of surface is open). [129, 173].
Columnar morphologies that characterized barriers, deposited at higher background deposition pressures, define a preferential path ways (in term of activation energy) for hydrogen atoms, that may diffuse through the ceramic coating and reach the stainless steel surface. Although, preferential path ways may be a possible explanation, it remains partially and incomplete. Unfortunately, surface effects (adsorption and desorption) cannot be determined. Surface constants for adsorption (σk_1) and desorption (σk_2) are strictly related to the surface condition

[1] **Activation energy**, $\mathbf{E}_A$ is defined as the minimum energy required to start a chemical or physical reaction. In this case the reaction is represented by the **surface interactions**

and allow to determine whether the permeation is atomically or molecularly. The main goal of this analysis is to provide a preliminary description of the coating behavior as barrier against hydrogen permeation in term of **permeation flux**, **J** and **PRF**. For this reason no surface studies are carried out. The conversion from **ion current** (the signal detected by the QMS) to **J** is performed by means of conversion factor. The conversion factor is defined by a measure of hydrogen permeation at same conditions (in terms of temperatures and pressures) of calibrated volume of hydrogen. Figure 3.15a shows the resume of the average values of **J** at different temperatures for bare and coated samples. As mention before, the average values of **J** increase while increasing both the temperatures and the background deposition pressure.

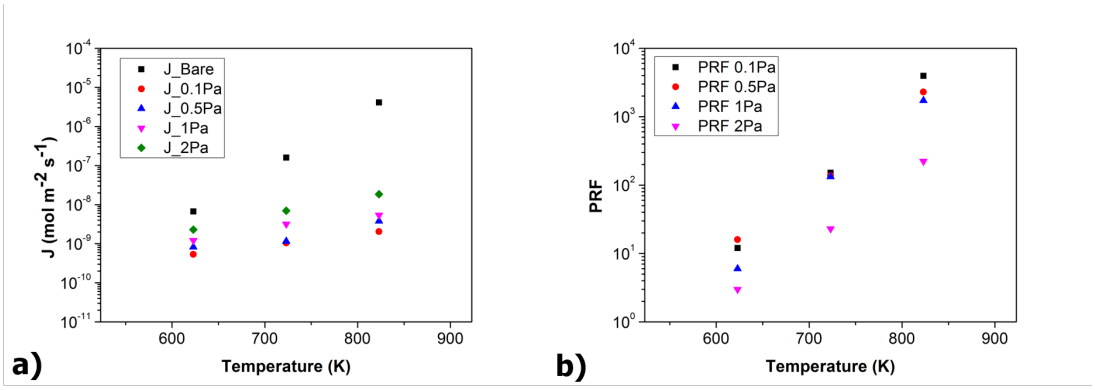

Figure 3.15: Hydrogen permeation flux defined by conversion of measured ion current.

Finally, by means of the equation 3.1, the **PRF** is defined for all conditions. **PRF** values are showed in figure 3.15b. Table 3.2, resumed the **J** and **PRF** values for these samples.

@623 K	**J** [mol $m^{-2}s^{-1}$]	**PRF**
Bare	6,67 10^{-9} ± 5.81 10^{-11}	1
0.1 Pa	5,36 10^{-10} ± 1.04 10^{-11}	12,4 ± 0,4
0.5 Pa	4,19 10^{-10} ± 1,76 10^{-11}	15,9 ± 0,6
1 Pa	1,21 10^{-9} ± 1,99 10^{-11}	5,5 ± 0,3
2 Pa	2,28 10^{-9} ± 2,91 10^{-11}	2,9 ± 0,3
@723 K	**J** [mol $m^{-2}s^{-1}$]	**PRF**
Bare	1,58 10^{-7} ± 2,42 10^{-9}	1
0.1 Pa	1,05 10^{-9} ± 1,05 10^{-11}	150,7 ± 3,8
0.5 Pa	1,15 10^{-9} ± 1,50 10^{-11}	137,8 ± 3,3
1 Pa	1,18 10^{-9} ± 1,29 10^{-11}	133,4 ± 3,0
2 Pa	6,94 10^{-9} ± 6,71 10^{-11}	22,7 ± 2,8
@823 K	**J** [mol $m^{-2}s^{-1}$]	**PRF**
Bare	4,13 10^{-6} ± 3,30 10^{-8}	1
0.1 Pa	1,04 10^{-9} ± 7,61 10^{-11}	3959,5 ± 60,5
0.5 Pa	1,80 10^{-9} ± 2,94 10^{-11}	2295,4 ± 99,1
1 Pa	2,39 10^{-9} ± 3,16 10^{-11}	1725,8 ± 86,8
2 Pa	1,85 10^{-8} ± 1,44 10^{-10}	222,8 ± 65,2

Table 3.2: Resume of J and PRF values

The exponential increment of **PRF** values with the temperature is mainly related to the dramatic increasing of permeation flux for the bare sample. Especially for sample covered with

Al_2O_3 grown at lower background pressures, the values of **J** change only about an order of magnitude respect over three order of magnitude for the bare sample. These results, underline the effectiveness barrier behavior of alumina-based coating grown by **PLD** technique.
According to these values, tests of barrier behavior of alumina-based coating grown by **PLD** are focused on optimizing the deposition process for compact and fully dense Al_2O_3.
As discussed in the introduction of section 3.2 and obtained as results in preliminary permeation tests described above, the best compact and fully dense stoichiometric Al_2O_3 is obtained at 0.1Pa of oxygen background pressure. The thickness of the investigated coating is from 100nm to 5μm, grown onto Eurofer97 disks. At the same matter of preliminary tests, these samples are characterized as permeation barrier by means of PERI II facility in the range of temperature from 623K to 923K.
Several works, carried out on coatings technologies as permeation barriers, demonstrate as the permeation through thin solid oxide films, without cracks or defects, is governed by atomic diffusion and can be described by using the **diffusion-limited model** (see section 2.1.4). [70, 74,75,77–81,111,112,124]. Thus in addition to the performance characterization in term of **PRF** and **J**, this model allows to define two important physical parameters, namely **permeability** and **activation energy**[2]. In figure 3.16 the results in term of **PRF** and **J** are resumed.

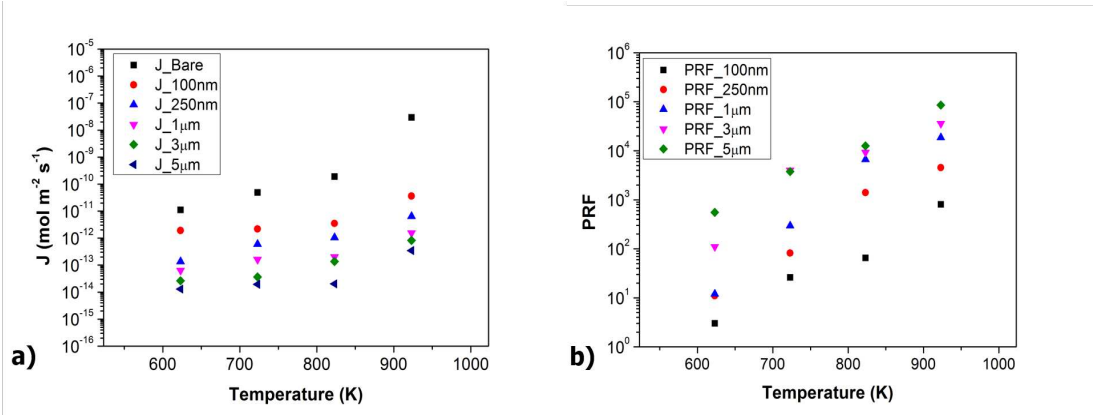

Figure 3.16: (a) Permeation flux, **J**, for different thicknesses of compact Al_2O_3 deposited at 0.1 Pa of background oxygen pressure. (b) the associated **PRF** values.

An unprecedented performance, values resumed in table 3.3, is obtained for thicker coating with a **PRF** value close to 10^5 at 923K and over 10^4 at 823K, that is the reference operating temperature for DEMO.

These results represent a breakthrough on coating developing as protective barrier in fusion technologies. In fact, a superior performance of amorphous ceramic coatings is obtained, being comparable to fully crystalline coatings one[125, 185]. Of course, the strength point of **PLD-grown** coatings is the **room temperature** processing as well as a compact and fully dense film. In this way no structural and metallurgical modifications of substrates are produced during the deposition as well as the lower energy consumption, making **PLD** technique economically competitive.
As pointed out before, by means of equation 2.26 of the **diffusion-limited model**, considering $n = \frac{1}{2}$ and d as the total thickness (for coated samples thin film plus substrate), it is possible to define the **permeability**. Permeability values are listed in figure 3.17. As expected, lower

[2]This analysis allows to define activation energy for the coupled system coating + substrate

PRF	623 K	723 K	823 K	923 K
100 nm	3,2 ± 0,12	25,7 ± 1,52	65,4 ± 4,69	810,3 ± 29,61
250 nm	10,7 ± 0,27	82,2 ± 4,17	1410,5 ± 81,83	4559,3 ± 200,31
1 μm	11,9 ± 0,3	295,6 ± 11,01	6661,2 ± 474,35	18729,9 ± 401,22
3 μm	110,4 ± 18,56	4020,8 ± 327,07	9312,9 ± 643,98	35960,1 ± 1292,62
5 μm	554.3 ± 50,00	3789,6 ± 280,58	12629,2 ± 1035,94	85369,8 ± 2713,55
J [mol m^{-2}s^{-1}]	**623 K**	**723 K**	**823 K**	**923 K**
100 nm	1,9 10^{-12} ± 7,4 10^{-14}	2,20 10^{-12} ± 5.3 10^{-14}	3.51 10^{-12} ± 3,8 10^{-14}	3.65 10^{-11} ± 8.6 10^{-13}
250 nm	1,35 10^{-13} ± 9,6 10^{-15}	5,96 10^{-13} ± 1,2 10^{-14}	1,05 10^{-12} ± 1,7 10^{-14}	6,48 10^{-12} ± 2,0 10^{-13}
1 μm	6,32 10^{-14} ± 1,5 10^{-15}	1,62 10^{-13} ± 1,3 10^{-15}	2,03 10^{-13} ± 1,0 10^{-15}	1,55 10^{-12} ± 1,3 10^{-14}
3 μm	2,64 10^{-14} ± 5,6 10^{-15}	3,67 10^{-14} ± 1,3 10^{-15}	1,36 10^{-13} ± 1,9 10^{-15}	8,24 10^{-13} ± 1,9 10^{-14}
5 μm	1,29 10^{-14} ± 1,6 10^{-15}	1,95 10^{-14} ± 5,6 10^{-16}	2,03 10^{-13} ± 6,5 10^{-16}	3,46 10^{-13} ± 6,4 10^{-15}

Table 3.3: Resuming values of **PRF** and **J** for as-deposited, not annealed, coated substrates

permeability values are obtained for thicker samples, underlining the higher difficult of hydrogen atoms to permeate the barrier (that define the higher **PRF** value).

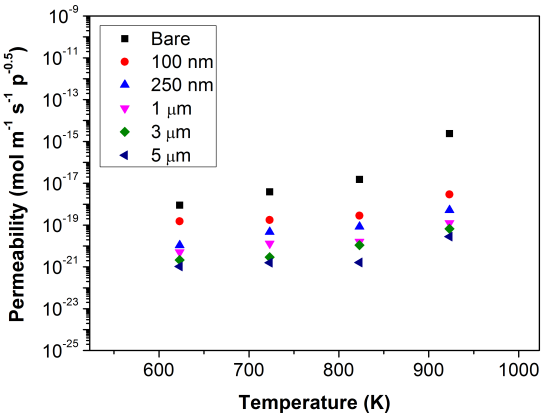

Figure 3.17: As expected, higher permeability are defined for bare samples and for lower coating thickness.

Except for bare samples and absolute performance of coated sample, **J** and **permeability** are not in good agreement with the literature. As described in section 2.1.4, **permeability** follows the **Arrhenius' law**, equation 2.59. Considering the figure 3.17 and plotting the trend curve of the data, the exponential term $\left[-\frac{E_p}{RT}\right]$ defines the slope of the trend curve itself. Since R and T are fixed values, it is easy to extrapolate the **activation energy**, $\mathbf{E}_A$, values both for bare Eurofer97 and coated samples. **Activation energy** values are shown in figure 3.23 and resumed in table 3.4 below.

	Bare	100 nm	250 nm	1 μm	3 μm	5 μm
Act. Energy (kJ mol^{-1})	11,4	41,51	45,42	51,92	53,18	56,59

Table 3.4: Activation energies, $\mathbf{E}_A$, for coated samples refer for the couple substrate-coating.

As shown in figure 3.23 and underline in table 3.3, pristine alumina-based coatings act as barrier against hydrogen permeation. A marked increase of activation energy, up to five times, is found for thicker coated sample. Moreover, activation energy for thinner coatings are

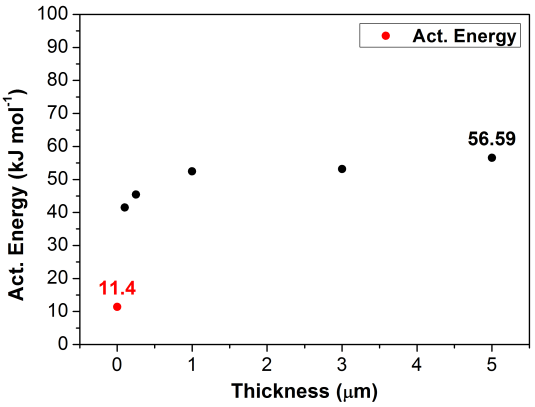

Figure 3.18: Dot in red indicates the activation energy for bare Eurofer 97 disk.

comparable with the thicker ones. This result may underline that the permeation through PLD-grown alumina is governed by bulk diffusion processes, thus the **diffusion-limited model**, in these tests conditions (in term of temperatures and pressures), is a good description of the permeation phenomena.
To evaluate coating adhesion and reliability in term of performance, all coated samples are subjected to thermal tests. Thermal tests are designed in order to simulate the pulsed behavior of a hypothetical DEMO reactor work cycles. Listed below the specifics of thermal annealing, repeated 50 times:

- Heating up from room temperature to 823K at 2K min^{-1}.
- dwell time at 823K of 2 h.
- Cooling down from 823K at 2K min^{-1} to 523K.
- dwell time at 523K of 2h.

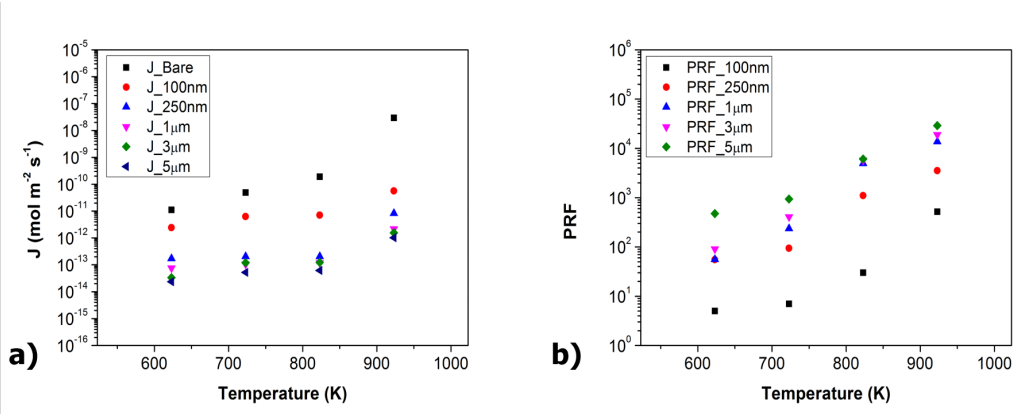

Figure 3.19: (a) Permeation flux, **J**, for different thicknesses of compact Al_2O_3 after thermal cycles and (b) the associated **PRF** values.

Thermal annealing condition is set-up in order to simulate the environment conditions, in term of water and oxygen concentration, of DEMO reactor. An overpressure of pure Ar

(99,99999%) gas is purified by using an oxygen-moisture trap (Supelpure®-O oxygen-moisture trap), in order to reduce down to 1ppb the oxygen concentration inlet. Samples are characterized again in PERI II facility by means of the same conditions describe above. Both **PRF** and **J** are showed in figure 3.19 and resumed in table 3.5.

PRF	**623 K**	**723 K**	**823 K**	**923 K**
100 nm	4,6 ± 0,44	6,9 ± 0,45	30,1 ± 5,45	518,7 ± 19,72
250 nm	54,9 ± 2,79	94,5 ± 3,90	1105,0 ± 627,2	3546,3 ± 857,07
1 μm	56,0 ± 1,46	235,4 ± 9,01	4966,5 ± 473,56	13662,5 ± 299,45
3 μm	91,4 ± 13,11	408,9 ± 194,01	5721,0 ± 631,91	19027,1 ± 1473,09
5 μm	475,8 ± 18,36	937,1 ± 60,75	6095,9 ± 473,56	28943,2 ± 1011,17
J [mol m^{-2}s^{-1}]	**623 K**	**723 K**	**823 K**	**923 K**
100 nm	$2{,}43\ 10^{-12} \pm 1{,}9\ 10^{-13}$	$6{,}32\ 10^{-12} \pm 2{,}4\ 10^{-13}$	$7{,}07\ 10^{-12} \pm 8{,}6\ 10^{-13}$	$5{,}70\ 10^{-11} \pm 1{,}4\ 10^{-12}$
250 nm	$1{,}72\ 10^{-13} \pm 7{,}1\ 10^{-15}$	$2{,}04\ 10^{-13} \pm 5{,}4\ 10^{-15}$	$2{,}05\ 10^{-12} \pm 9{,}0\ 10^{-14}$	$8{,}33\ 10^{-12} \pm 9{,}4\ 10^{-14}$
1 μm	$7{,}57\ 10^{-14} \pm 2{,}1\ 10^{-15}$	$3{,}06\ 10^{-13} \pm 1{,}6\ 10^{-15}$	$5{,}19\ 10^{-13} \pm 2{,}6\ 10^{-14}$	$2{,}16\ 10^{-12} \pm 1{,}9\ 10^{-14}$
3 μm	$3{,}33\ 10^{-14} \pm 5{,}6\ 10^{-15}$	$1{,}20\ 10^{-13} \pm 1{,}8\ 10^{-15}$	$4{,}23\ 10^{-13} \pm 9{,}7\ 10^{-15}$	$1{,}55\ 10^{-12} \pm 6{,}6\ 10^{-14}$
5 μm	$2{,}36\ 10^{-14} \pm 5{,}3\ 10^{-15}$	$5{,}22\ 10^{-14} \pm 1{,}8\ 10^{-15}$	$6{,}17\ 10^{-13} \pm 1{,}71\ 10^{-14}$	$1{,}02\ 10^{-12} \pm 2{,}3\ 10^{-14}$

Table 3.5: Resuming values of **PRF** and **J** for annealed coated substrates

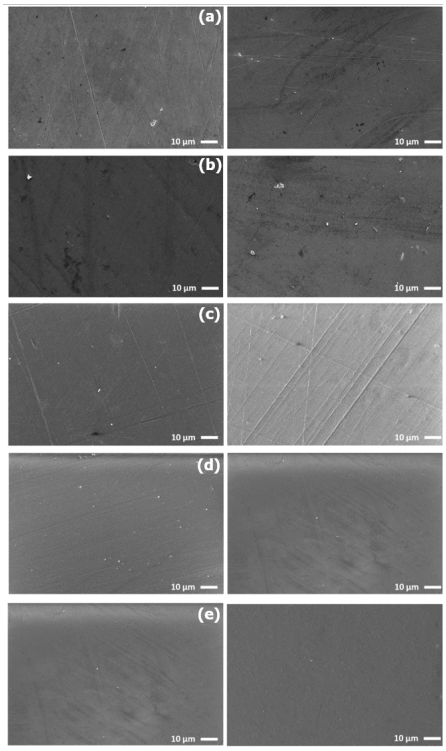

Figure 3.20: SEM images on the left refer to as-deposited coated surfaces and images on right refer to post annealed coated surfaces. Eurofer 97 disks coated with PLD-grown Al_2O_3 (a) 100nm; (b) 250nm; (c) 1μm; (d) 3μm; (e) 5μm.

However, an accurate SEM analysis, figure 3.20, reveal no cracks or film delamination over all the coated surface, comparing the value before and after thermal cycles (see tables 3.3, 3.5 and figure 3.21 below) a general performance degradation is observed. Thus, the change

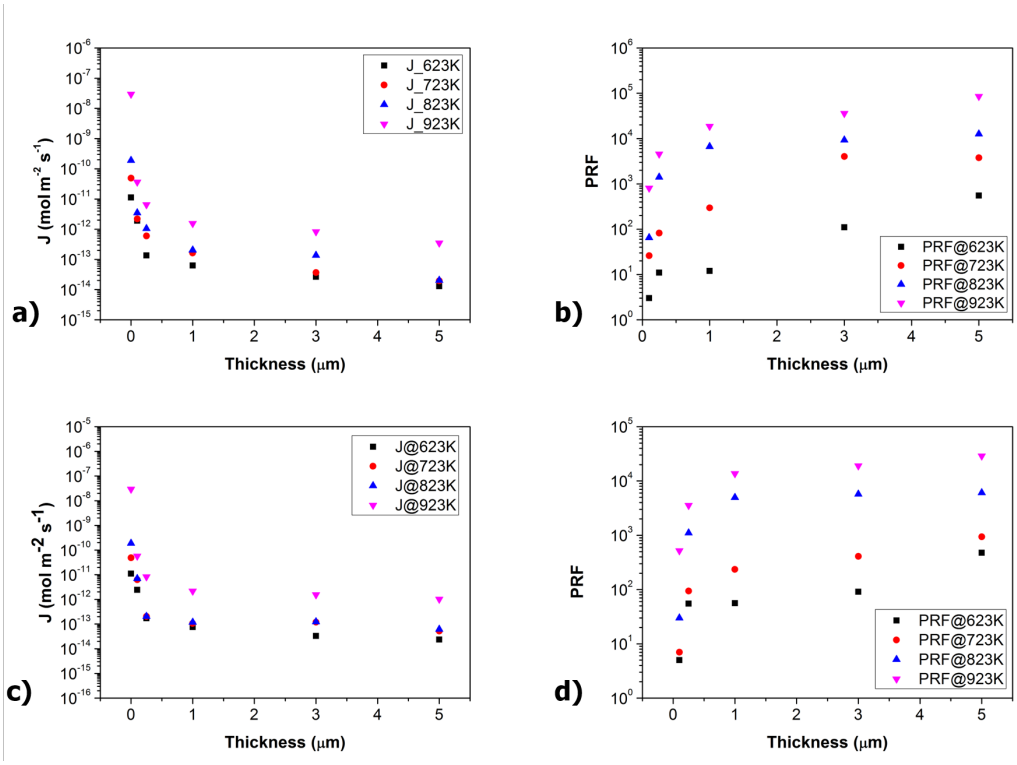

Figure 3.21: (a-b)Show the resuming values of **PRF** and **J** in function of thickness for as-deposited substrates; (c-d)show the resuming values of **PRF** and **J** in function of thickness for annealed substrates.

in performance is not caused by coating modification or failures but it may be explained by substrate structural changes after both thermal cycles and permeation measurements. Several works underline the influence of the substrates in terms of surface preparation and materials.[80, 185, 186] In fact, as describe in sections 1.2.2 and 1.2.3, ferritic-martensitic steels suffer high temperature working (i.e thermal cycles and heat treatments above 873-923K) which changes their morphology. The main effects are an increasing in grain size (that produces a decreasing in hardness), the evolution of some ferritic phase (mainly alpha phase ferrite well describe by means the Hollomon-Jaffe relation) and various precipitates. In fact alloying elements (i.e C, N, Ti, Nb, V, Cr and Mo) promote the formation of precipitates like Cr-rich $\mathbf{M_{23}C_6}$, and Ti, Nb or V-rich **MX** particles (where M stands for metals). The Cr-rich type precipitates are mainly observed at the lath boundaries and prior austenite grain boundaries. These precipitates obstruct the movement of dislocations, refine grains during heat treatment, and delay the plastic deformation.[187–195]

Nevertheless, it is obtained the interesting technological result as **breakeven point**, meeting the requirements of thickness and minimum **PRF** values. To reduce the radiological activities by released tritium below 5 Ci day^{-1}, as described in section 1.2.1, the required **PRF** value is at least 1000 at the end of life of the **breeding blanket**.
Thanks to the defect free and fully dense and compact PLD-grown $\mathbf{Al_2O_3}$, this requirement, at the expected operating temperature of 823K, is obtained for a very thin barrier of 250nm of thickness (see figure 3.22). This result is a technological and economical breakthrough. In fact, it allows to define the exact amount of tritium loss through the breeding blanket, optimizing

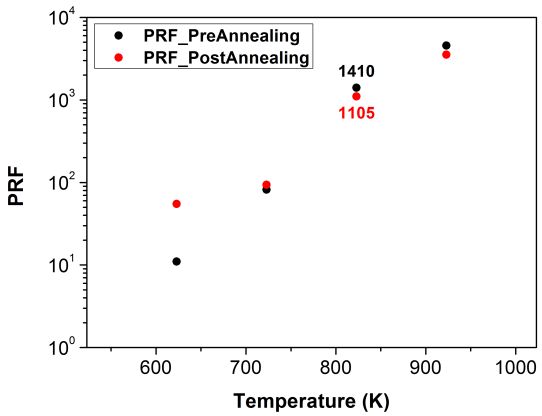

Figure 3.22: In black PRF in function of temperature for 250 nm PLD-grown pristine coating. Red dots indicate the PRF for the sample annealed. However, the performance decrease of about 20%, after thermal cycles the minimum PRF requirement is satisfy.

the tritium balance during all DEMO life cycle overall the radiological protection of workers. Last, but not the least, it allows to define the minimum economical impact of the coatings in order to satisfy the minimum PRF requirement.

3.2.2 Deuterium permeation tests under electron irradiation

It is expected that hydrogen isotopes permeation during irradiation could be deeply modified by means radiation induced effects such as **radiation enhanced diffusion**, **adsorption**, **desorption** or **radiation induced reaction** between hydrogen isotopes and protective coating materials.[196]
A full characterization of PLD-grown alumina has been carried out during 2016 in collaboration with **CIEMAT** laboratories.
The final choice in this frame is to grow Al_2O_3 at low background gas deposition pressure (obtaining a fully dense and compact barriers). Process parameters are listed below:

- laser pulse energy 410 mJ.
- laser pulse fluence $\sim$ 4 J cm^{-2}.
- pulse repetition rate of 20 Hz.
- background oxygen pressure in the range 0,1 Pa
- base vacuum pressure $\leq$ 5 10^{-3} Pa.
- target to substrate distance of 5 cm.

In this study, the characterizations of the coating are investigated by **SEM-EDX** analysis, **XRD** analysis and **deuterium permeation tests** under **electron irradiation**.
More specifically, deuterium permeation tests are carried out at **Radiation Induced Permeation and Released**, **RIPER**, facility of CIEMAT, as shown in figure 3.23.

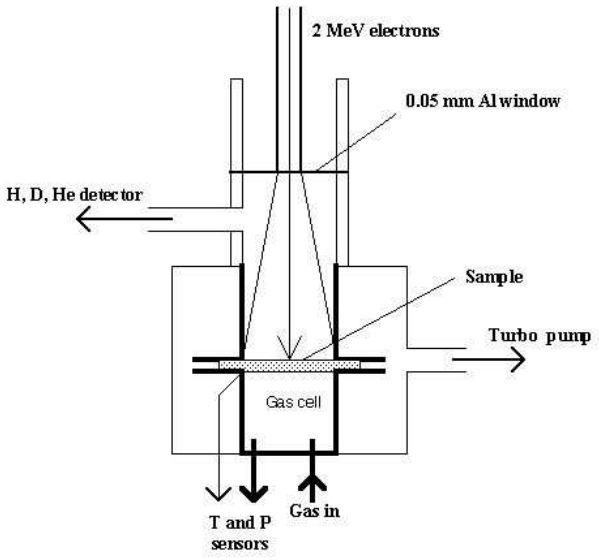

Figure 3.23: Scheme of RIPER facility at CIEMAT

Electron beams are produced by a linear Van de Graaff accelerator with the following experimental parameters:[197]

- Dose rates up to 400 Gy s^{-1}.
- Testing temperature 723 K.
- Ion beam energy up to 1.8 MeV.

Substrates are Eurofer97 disks of 36mm of diameter and 0.7mm of thickness. Similarly to substrates used for hydrogen permeation tests, these substrates are grounded using SiC paper with increasing grits (up to 2400) and polished with diamond suspensions (up to 1μ m) and cleaned with an ultrasonic device in ethanol and rinsed in distilled water.

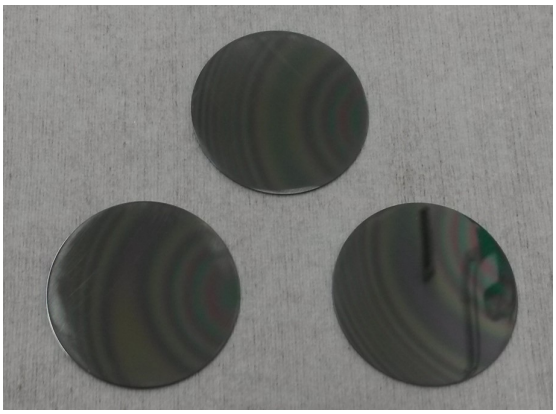

Figure 3.24: Eurofer97 disks covered with 5μm of compact alumina. Substrates are 36mm in diameter and 0.7mm in thickness

Substrates are covered on one side with 5μm of compact alumina, in order to obtain a fully dense permeation barrier. Figure 3.24, shows coated Eurofer97 disks.

Composition of as-deposited samples are characterized by means **SIMS** and **EDX** analysis. As shown in Figure 3.25(a) **AlO** and $\mathbf{Al_2}$ (two Al atoms together) are typical $\mathbf{Al_2O_3}$ fragments for Ar^+ SIMS. Instead, **Fe** and **Cr** fragments are used for Eurofer 97 detection. The **EDX line scan** pictured in Figure 3.25(b) confirms that the external structure (first 5μm) consists of **Al** and **O** in the ratio close to $\frac{2}{3}$.

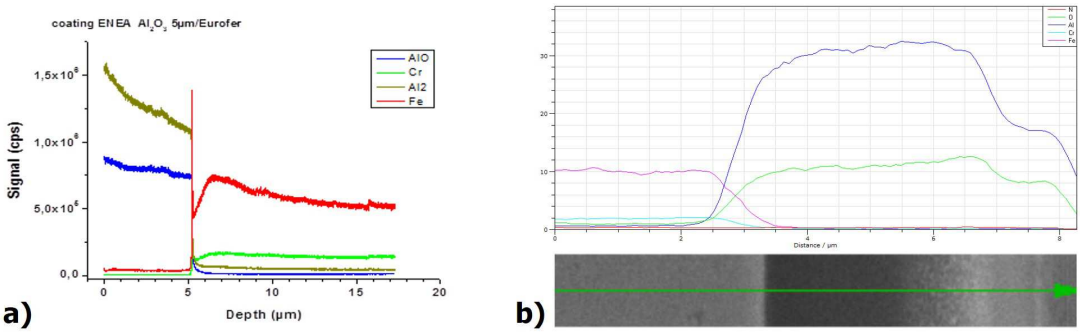

Figure 3.25: (a) SIMS analysis for the 5μm PLD-grown alumina. (b) EDX line scan picture shows clearly the interface between the alumina coating and Eurofer steel substrate.

In any case, both **SIMS** and **EDX line scan** underline a sharp transition at the coating-Eurofer interface.
The sample is place in such a way to divide the RIPER facility in two sides, sealed on both faces by copper rings as shown in figure 3.23. In one side (the coated one) deuterium is continuously introduced and the other side is irradiated by electron beam. The amount of permeating deuterium through the samples is measured by a Pfeiffer Smart Test (with a sensitivity of 10^{-12} mBarL sec^{-1}.
Permeation tests are carried out at 723K for seven days. Temperature control and measurement are performed by means a thermocouple welded on the uncoated side of the sample.

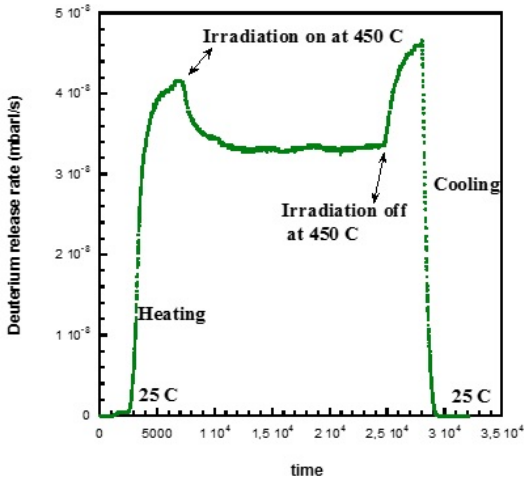

Figure 3.26: Deuterium permeation during and without electron irradiation for alumina coatings

During the tests, samples are heated up from room temperature up to 723K with a ramp of 10K min^{-1}. At this temperature, electron irradiation is performed for 8 hours. After that,

sample is cooled down to room temperature rapidly. The same procedure is used for all testing days. Figure 3.26 shows the deuterium permeation during this procedure. **PRF** is determined comparing permeation results of bare Eurofer97 disk and alumina coated disks. As shown in figure 3.27 a PRF close to 1000 is observed with a reduction of permeation deuterium flux from 10^{-5} mBarL sec^{-1} (measured for bare disk) to 3 10^{-8} mBarL sec^{-1} (measured for coated disks).

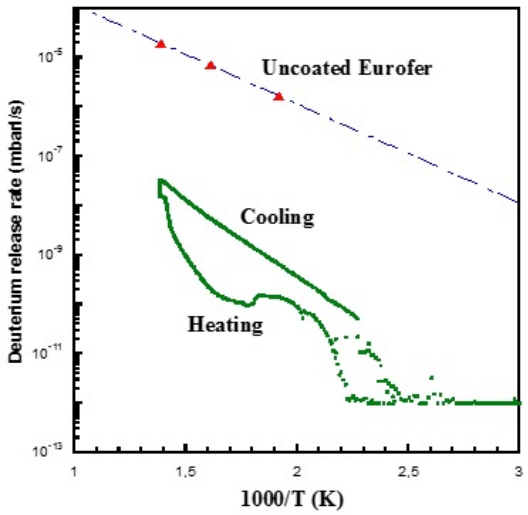

Figure 3.27: Dots in red define deuterium permeation for bare Eurofer97 disk. Curve in green is the deuterium permeation rate for coated samples during heating-cooling cycles.

Deuterium permeation measures are carried out for seven days within several thermal and irradiation cycles.

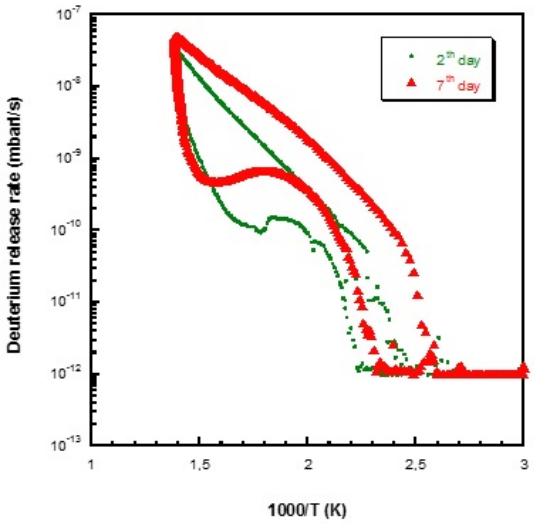

Figure 3.28: Comparison between deuterium permeation after two days and seven days.

Even though a slightly increase of deuterium permeation rate up to 5 10^{-8} mBarL sec^{-1} is seen (compared to 3 10^{-8} mBarL sec^{-1}), after several days of measure no dramatic increase

of permeation. keeping the PRF close to 1000. Figure 3.28 resumes the deuterium permeation values during the days. Finally, these measures, according with hydrogen permeation results, underline that alumina coating acts correctly as **anti-permeation barrier**.

3.2.3 Corrosion in static liquid eutectic Pb-16Li

Corrosion of steels by heavy liquid metal compounds depend on many factors, as described in section 2.2 and shown in figure 3.29.[198] Two of the most important parameters are temperature and oxygen concentration in the liquid metal.

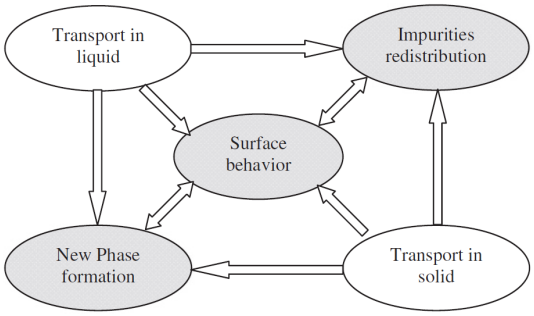

Figure 3.29: Simple view of corrosion synergies in liquid metals.[198]

Generally, for a given temperature, corrosion proceeds by oxidation if the oxygen content is high enough.

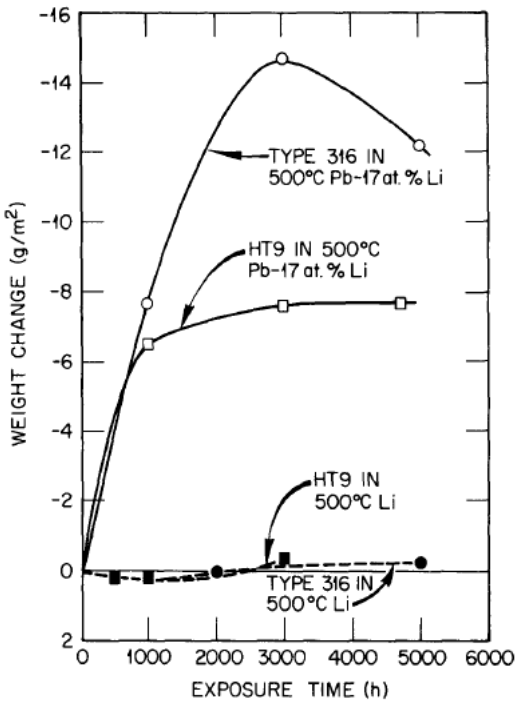

Figure 3.30: Changing in weight during the time for austenitic 316 and ferritic-martensitic HT9 stainless steels in static pure **Li** and eutectic **Pb-17Li** at 773 K.[200]

On the contrary, if the oxygen content is very low, direct dissolution of the most important alloying components of steels takes place. Since austenitic alloys are particularly susceptible to this type of corrosion (as well as swelling under severe neutron irradiation) due to the considerable amount of Ni, ferritic-martensitic alloys are the major candidate for DEMO breeding blankets (see sections 1.2.2 and 1.2.3). Effect of pure **Li** on structural steels is mainly related to penetration on grain boundaries, producing precipitates that affect mechanical properties such as ultimate tensile strength, ductility of material and reducing of ultimate creep strength[199]. Although, pure **Li** can act as both tritium breeder and coolant under certain accident conditions, this alloy would exotically react with water and air. Low-melting eutectic **lead-lithium**, **Pb-16Li**, alloys are potential tritium breeding materials for **WCLL, HCLL** and **DCLL breeding blankets** designs. Additionally, the lead provides neutron multiplication as well as first wall cooling. Several experiments with static and flowing eutectic lithium-lead, have shown how lead-rich solution acts like pure lead.[50, 85, 113, 114, 167, 200–204]
In pure lead environment the corrosion rate is much higher when it proceeds by dissolution, and in this condition it is generally avoided by injecting oxygen into the liquid lead. Ceramic coatings, such as Al_2O_3 provide a promising alternative to this strategy. However, oxygen concentration in **Pb-16Li** alloy is a fundamental parameter when coating strategy is considered. As shown in figure 3.31, activity of **Pb-16Li** changes drastically in function of oxygen content and temperature. In some condition, it is evident how Al_2O_3 can be unstable, mainly due to the chemical reduction attack lead by lithium.

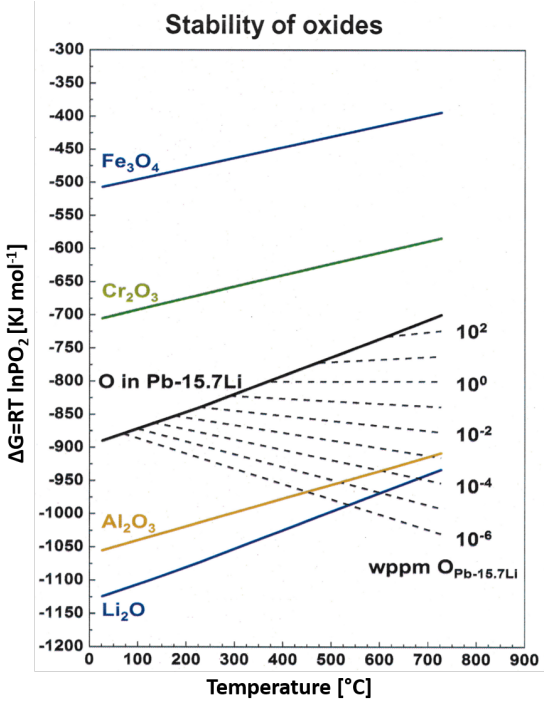

Figure 3.31: Thermodynamics scenarios in function of oxygen content and temperature. Alumina is stable in pure lead environment even at high temperature. Pure lithium has more favorable energy formation of oxide respect to alumina. Then in some condition of temperature and absent of oxygen content alumina results unstable in eutectic Pb-16Li alloy

During last decades, thermodynamic studies on coatings stability are carried out on eutec-

tic **Pb-17Li saturated** with oxygen. Considering oxides barrier materials, diversity of their behavior is displayed. Among the most common oxides (around the DEMO operating temperature 723K - 823K) for example **chromia**, $\mathbf{Cr_2O_3}$ is unstable even in saturated condition and it reduces to metallic chromium. In case of **Alumina**, $\mathbf{Al_2O_3}$ is quite stable to reduction to metal with a Gibbs free energy close to zero, $\Delta_r G^a = 143,8\text{kJ mol metal}^{-1}$. (On the contrary, $\mathbf{Al_2O_3}$ is unstable to reduction to metal in saturated pure **lithium**). Moreover, thermodynamics calculations indicate that decreasing the oxygen concentration and increasing the temperature lead to more negative value of Gibbs free energy of oxide formation, then to the oxide instability.[61, 118, 205]
More recent works carried out at high temperature (up to 1073K) in saturated eutectic **Pb-17Li** underline the degradation of $\mathbf{Al_2O_3}$ by means of the formation of ternary oxide. Since ternary oxide, namely $LiAlO_2$, is thermodynamically favored, it results more stable to reduction to the metal.[61, 118, 121, 122, 164, 205]
In this study, the effectiveness of the coating is investigated by the short-term (around 1000h) exposure of coated and uncoated samples to stagnant molten **Pb-16Li**. Corrosion tests are carried out at **C.R. ENEA** of Brasimone (BO) and longer tests (2000h, 4000h and 8000h) at the same condition are still undergoing.
The aim of the tests is to provide a simple comparison of the performance of the coating with respect to uncoated samples. For this reason, neither an active oxygen control is performed nor chemical condition of the HLM during the exposure are assessed systematically. The thickness of investigated ceramic coating is 1μm on both sides of the plate as shown in figure 3.32.

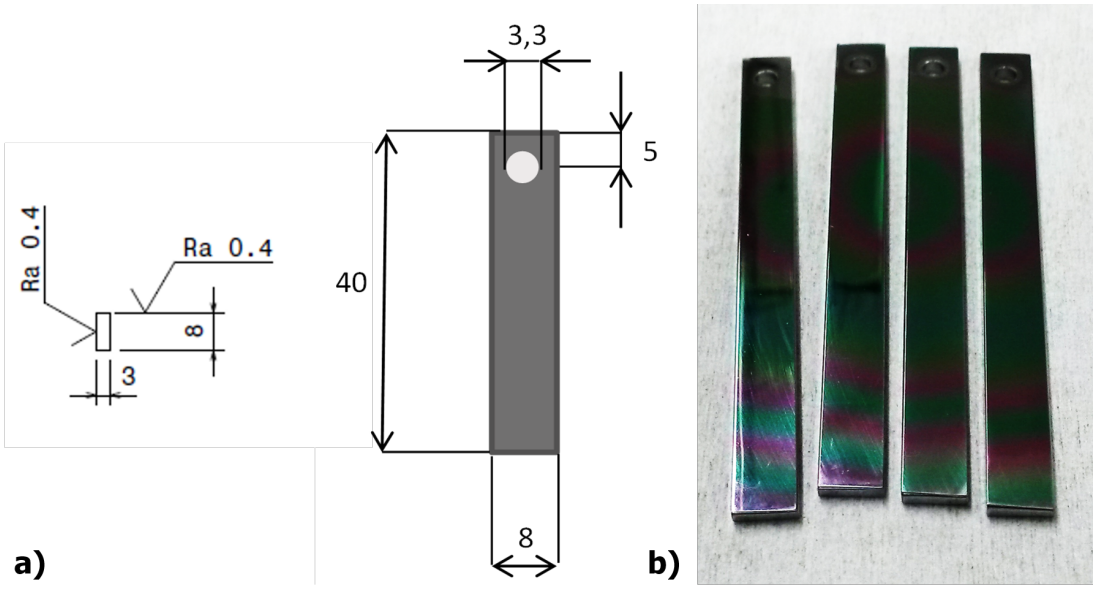

Figure 3.32: (a)Scheme of eurofer97 plates, plates are 40mm long, 8mm width and 3mm thick. (b) Pristine plates covered with 1 μm of PLD-grown alumina.

Coated and uncoated samples are characterized in a dedicate facilities in order to minimized the oxygen content and contamination of **Pb-16Li** by impurities such as: corrosion products and metals intrinsic impurities. Cylindrical vessels are equipped with an alumina crucible (125mm in diameter and 220mm height) positioned on the bottom of the vessel itself.

A system of rods handling is used to plunge the samples inside the melted **Pb-16Li** alloy. In figure 3.33 is pictured the testing facility.

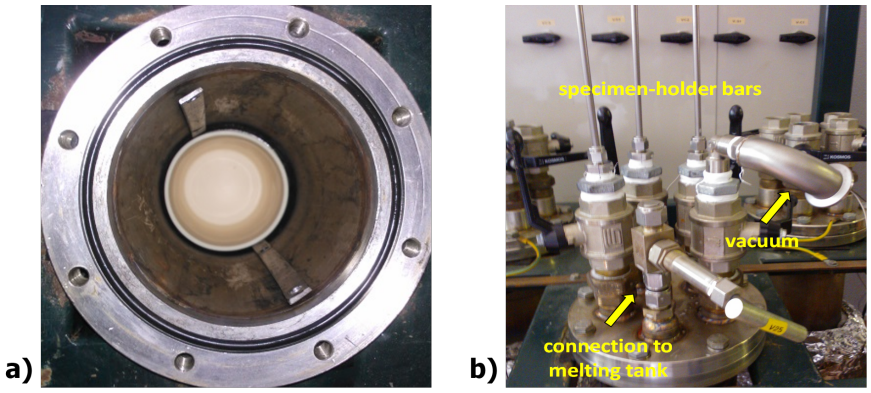

Figure 3.33: (a) Alumina crucible on the bottom of cylindrical stainless steel vessel. (b) Valves and vessel hydraulic connection with rods handling system. *Courtesy of ENEA*

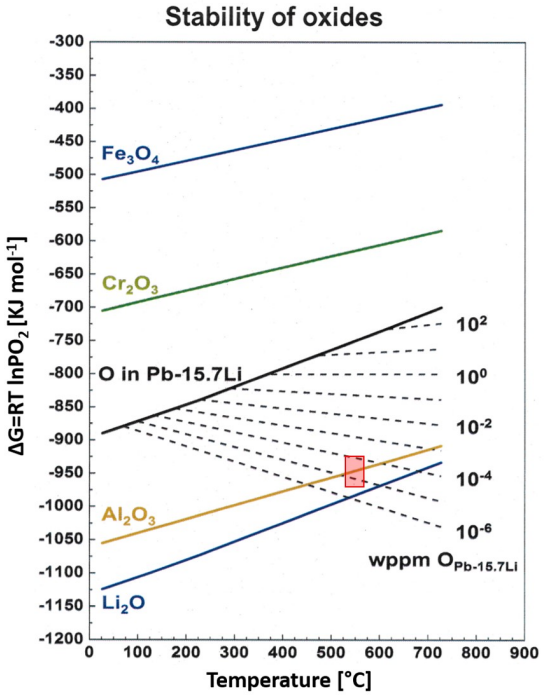

Figure 3.34: Thermodynamic condition of the corrosion test performed in collaboration with ENEA Brasimone (BO). Test is carried out at 823K in dissolutive condition. Oxygen concentration may lead to dissolutive condition for alumina.

To avoid impurities charging inside the vessel, **Pb-16Li** is charged by following the procedure below:

- Pb-16Li ingots are surface cleaned.
- Inside a melting tank, after a two days of vacuum at 400K, ingots are melted in pure argon (99,9999%) overpressure atmosphere up to 573K±5K.

- Melted Pb-16Li is moved inside the vessel (test section) by means of a tube with PORAL filter (to avoid impurities charging).
- About 12 Kg of Pb-16Li eutectic are loaded inside the vessel and solidify at room temperature.
- Samples are inserted into the vessel.
- Ceramic capsule is heated up to 823K in 0,8bar overpressure of pure Argon (static conditions).

Figure 3.34 shows the nominal thermodynamic condition of the test, which is attained performing the experiment in an ultra pure Ar atmosphere (H_2O concentration down to 10^{-3} wppm and O_2 concentration down to 5 10^{-4} wppm. Then, corrosion test is carried out in dissolutive condition, may close to the eutectic Pb-16Li saturation. At the end of the test, rods handling put off the samples from the molten **Pb-16Li**. Samples are left to cool down inside the vessel. As shown in figure 3.35 the eutectic alloy adheres to the surfaces of both coated and uncoated samples. While uncoated sample is oxidized the coated sample is still intact.

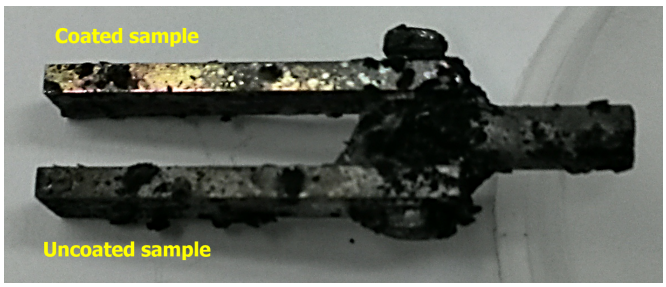

Figure 3.35: Coated and uncoated samples after 1000h in stagnant **Pb-16Li** at 823K. Uncoated sample is clearly corroded, on the contrary the coated sample seams, by visual inspection, to be in perfect conditions.

The comparative interpretation of the results of the tests is straightforward. Eurofer97 suffers of corrosion-dissolution and generalized grain boundaries attack by molten lithium. Figure 3.36 shows SEM images grain boundaries attack of the uncoated sample.

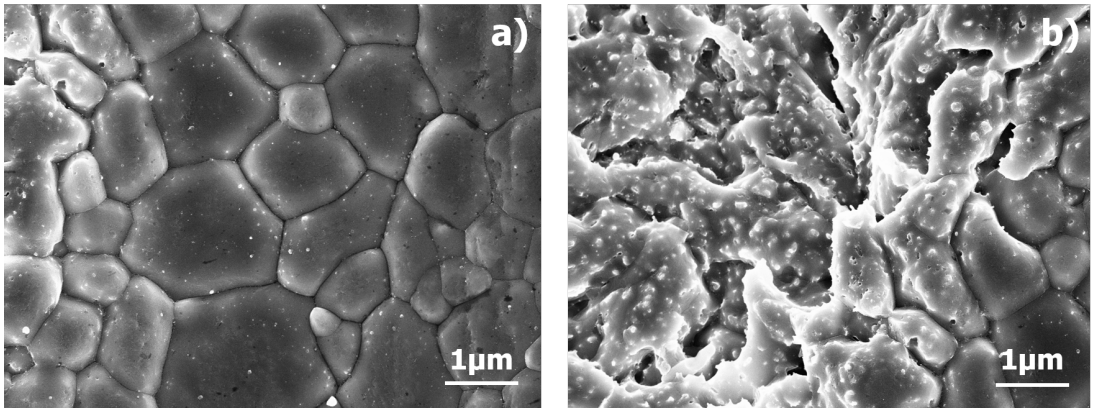

Figure 3.36: (a-b) Grain boundaries attack is a typical phenomena due to the lithium penetration. Moreover, dissolution phenomenon occurs by means of liquid lead.

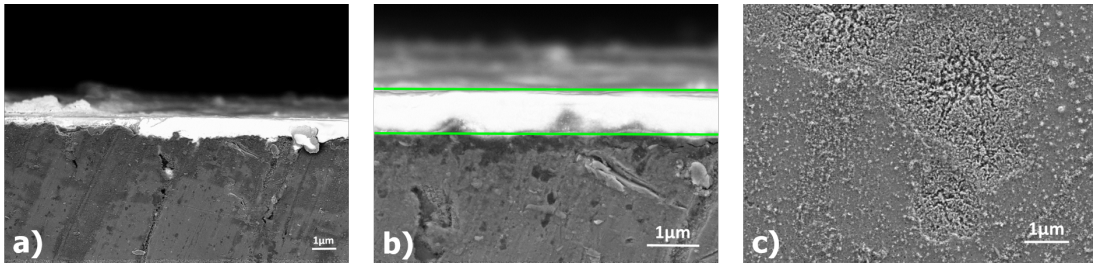

Figure 3.37: Cross-sectional SEM (a-b) of coated eurofer 97 plate exposed to liquid **Pb-16Li** for 1000h at 823 K. The thickness of the coating is still around 1 μm. (c) Top-view SEM images of the coating after exposure.

By contrast, signs of corrosion are not found on the coated sample. Figure 3.37 shows cross-sectional SEM images of coated sample. No cracks, delamination phenomena or coating thickness reduction are observed. Some traces of interaction can only be visible by means SEM on-top image as shown in figure 3.37(c). A possible explanation may be the dissolutive condition due to the low oxygen concentration. In some conditions, in term of oxygen concentration and temperature, alumina results unstable ($\Delta_r G^a \leq 0$) in eutectic **Pb-16Li**, and as mention before, oxygen concentration during the corrosion experiment could lower enough, see figure 3.34.[61,118,205] Longer corrosion tests, that are still undergoing at **ENEA Brasimone**, may answer to this question.

3.3 Atomic Layer Deposition approach for complex geometry barrier coating

One of the target of this Ph.D work is to develop a custom made **Atomic Layer Deposition**, **ALD** facility, optimized for stainless steel coating with complex geometry. **ALD** is a well known deposition technique, largely used for depositing very conformal thin films for a variety of applications, mainly: **organic electronics, semiconductor processing and micro-mechanics coating**. More and more miniaturization has produced very high aspect ratio structures that need to be coated conformally. Moreover, the necessity for continuous and pinhole-free thin films (e.g. ultra-low gas diffusion barriers) is matched perfectly only by **ALD** deposited films.[206–209] The aim of this project is to optimize the deposition process for stainless steel substrate of a *stop flow* **thermal ALD**. However thermal ALD is the first of kind design developed, is the only candidate that can be scalable-up to cover the entire and assembled **breeding blankets**.

Thanks to the **self-limiting** behavior of thin films growing, it could be possible to cover conformally the entire breeding blanket, injecting the right quantity of precursor (substrate is the whole breeding blanket volume) and using the breeding blanket itself as reaction chamber. As shown in figure 3.38, **ALD** facility is composed of stainless steel deposition chamber with a heated sample holder, ranging from room temperature up to 523K. Precursors are stored inside a separated stainless steel tanks, isolated from the deposition chamber by an **ALD** pneumatic **valve** (Swagelok® ALD3 diaphragm valve). As described in section 5.2, precursors are injected inside the chamber separately, driving by means of the pressure gradient due to the vapor pressure stability of the precursor before the ALD valve and the vacuum inside the

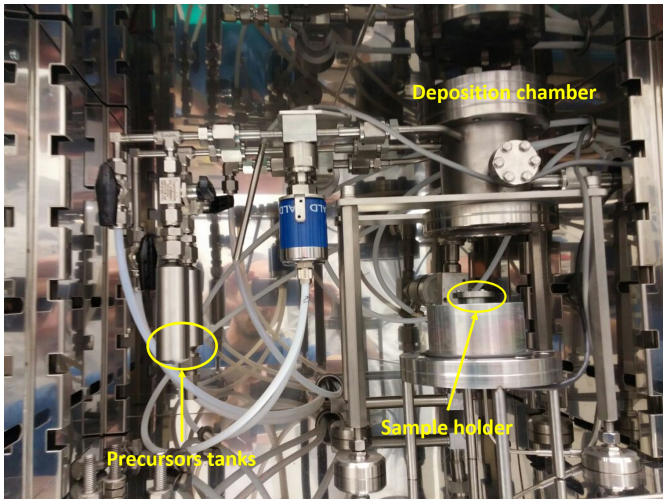

Figure 3.38: Laboratory mock-up scale ALD facility. ALD is set up for binary processes, in particular two separated precursor lines carried the precursor inside the reaction chamber. Samples are hold on a heated sample-holder ranging from room temperature up to 523K.

reaction chamber. To choose the right partial pressures of precursors (then, the right quantity of precursors to complete each **half-reactions**, (see section 5.2) tanks can be heated separately as well as the ALD valve opening can be set separately (starting from 50ms).
Each reaction with the surface must happen with the proper precursor. For ensuring so, before each precursor injection, the reaction chamber is purged by an inert gas (generally Ar or N_2) and subsequent vacuum is reached by using a turbo-molecular pump, in the order of 10^{-4}Pa. Preliminary work and experiments are focused on setting up and characterization of **ALD** machine by depositing the most common metal oxides material such as **alumina, Al_2O_3** and **titania, TiO_2** (more details in section 5.2). In particular the aim is to define the right set up of parameters such as: precursors temperature, sample holder temperature, purging time, ALD valve opening time, pumping time (to ensure the adequate level of vacuum) and reaction time (or precursor residence time) in vacuum chamber.

Tuning up these parameters is possible to perform a calibration, obtaining the so-called **ALD regime**. Since the self-limiting nature of the deposition process, ALD regime is characterized of a linear dependence of film thickness to the number of cycles, as shown in figure 3.39. In the case of metal oxides tested here, the **ALD regime** is obtained for precursors temperature in the range of 313 - 333K, sample holder temperature ranging from 353K - 450K, purging time over 120s, pumping time over 180s and reaction time above 5s.
For lower temperature of precursors, the vapor pressure is too low for reaching the saturation inside the vacuum chamber. Higher temperature of precursors may cause the boiling with condensation and consequently goggling of piping. Lower sample holder temperature may cause the condensation of the un-reacted (surplus) precursor inside the vacuum chamber. Instead, for temperature above 450K a phenomenon of precursor dissociation starts. The consequences are uncompleted surface **half-reactions** with a reduction of growth rate as well as changing in thin film properties.

Furthermore, the best thin film properties in term of density and conformality are obtained at 450K of sample temperature for both oxides. Figure 3.40(a-b) shows respectively titania

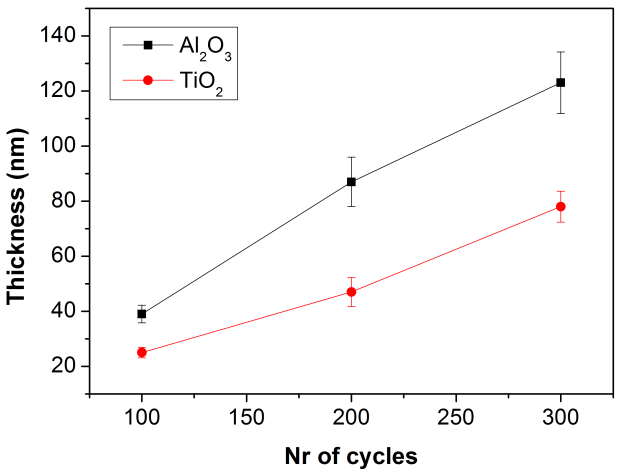

Figure 3.39: Graph shows the characterization growth regime of both Al_2O_3 and TiO_2 at 450K developed during this Ph.D. work. The linear dependence of thin film thickness with number of cycles underline an **ALD regime growth**

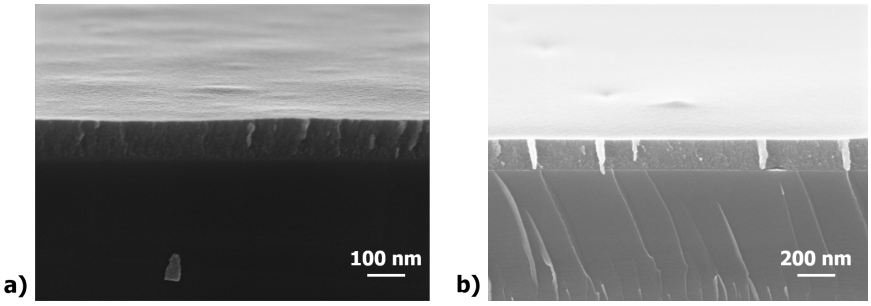

Figure 3.40: (a)Cross-sectional SEM of 300 cycles of TiO_2 grown at 450K. (b)Cross-sectional SEM of 300 cycles of Al_2O_3 grown at 450K. Both thin films show defect and pinhole free surface. Moreover, all substrate surface is homogeneously covered.

and alumina thin film deposited at 450K. Compactness and pinhole free surface are obtained. Finally, a first of kind tests in order to provide the Al_2O_3 coating conformity on cylindrical geometry, adhesion and barrier properties is carried out by means of thermal cycles in air.
AISI 316L stainless steel tube and plate are covered respectively with 100cycles (∼40nm) and 300cycles (∼130nm), as shown in figure 3.41.

Five thermal cycles are performed in air, from 523K to 823K with heating and cooling ramp of 4K per minute. In figure 3.41(a) and (c) are shown samples as deposited. After the thermal cycles, the coating seems to adhere and no delamination phenomena are detected. Moreover, looking in detail figure 3.41(b) the uncovered steel is clearly oxidized, instead the cover surface is still as pristine. The same behavior is obtained for the plate as figure 3.41(d) shows.

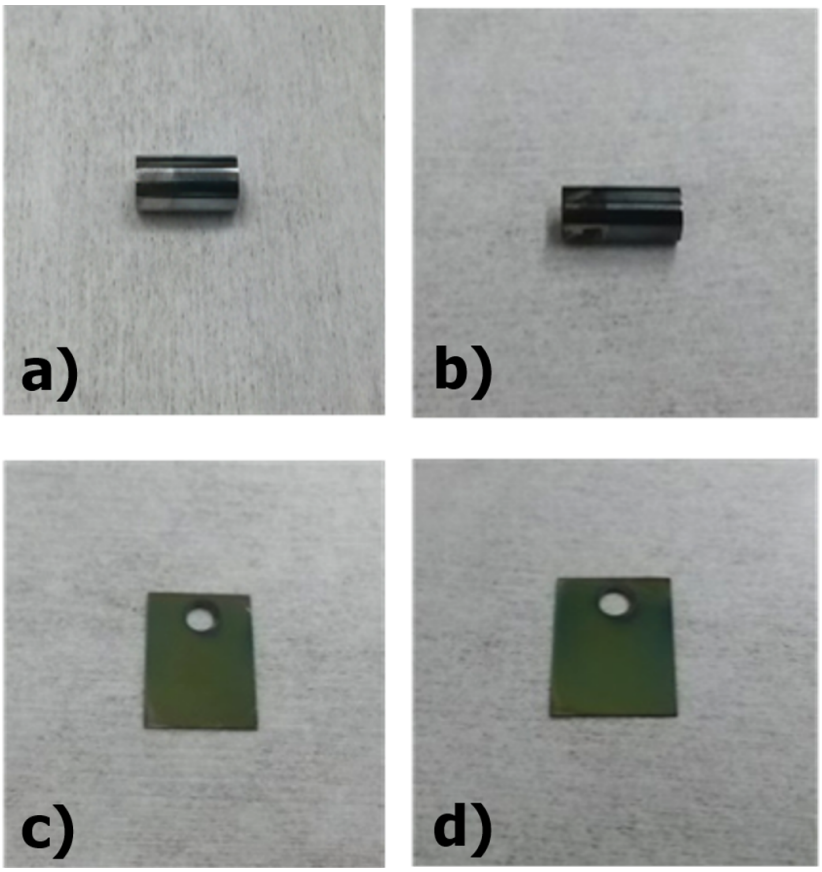

Figure 3.41: Samples are covered with ALD grown Al_2O_3 at 450K. (a)Pristine stainless steel tube covered with 100 cycles of alumina. (b)Covered tube after thermal cycles, evidence of oxidation is present for the un-covered area. Covered surface is look as pristine. (c)Pristine stainless steel plate covered with 300 cycles of alumina. (d)Covered plates after thermal cycles appear intact.

Chapter 4

Conclusion

4.1 Summary & Outlook

This **Ph.D** thesis has presented experimental investigations, accompanied by models for their interpretation, carried out with gaseous permeation and static heavy liquid metal corrosion. To meet fusion-grade requirements a promising process, namely **PLD**, as well as a custom **ALD** facility are proposed according to a bottom-up approach.
In the first part of the work, hydrogen transport and inventory parameters (permeability, activation energy) and engineering parameters (PRF and J) are determined for ferritic-martensitic (eurofer97) bare and PLD coated steels. In particular, PLD-grown alumina, thanks to its density and defect-free conditions, obtained an unprecedented PRF value close to 10^5 at 973K, an order of magnitude grater than the most performance crystalline bulk alumina.[124,133,158,160]
The condition of the surfaces is of crucial importance for the growth of PLD alumina and for hydrogen permeation. In fact, PLD-grown alumina follows the surface roughness that can influence the film adhesion and performance[159]. Thus, an accurate grounding and cleaning protocol has been developed.
Characterization of PLD-grown barrier is performed in PERI II facility in DEMO relevant conditions measuring hydrogen permeation in **continuous flow** by using a **quadrupole mass spectrometer**. Temperatures ranging from 623K to 923K are tested using a hydrogen partial pressure of 100mBar. After a preliminary screening of different PLD-grown barrier morphology, made by changing the background gas pressure, the followed choice is to to develop and optimize the deposition process for compact alumina. Several thicknesses of compact barrier films are tested (100nm, 250nm, 1μm, 3μm and 5μm) as pristine and after a severe thermal cycles (50 cycles, from 523K to 873K with heating and cooling ramp of 2K per minute and dwelling time of 2h in pure Ar (99,99999%) environment. Results underline a slight decreasing of barrier performance that can be caused by a metallurgical modification of substrates. In fact, accurate **SEM** analysis reveal no cracks or morphology modification of the PLD-grown barrier.
Moreover, interesting engineering results are extrapolated from these tests and measures. Considering, the target barrier of PRF$\sim$1000 at the end of the breeding blankets life, PLD-grown alumina meets this value already for 250nm thick film, even after thermal cycles. This result has engineering and economic importance for the developing of breeding blankets coating, allowing to define cost and materials inventory.
In the last part of the work, the same PLD-grown alumina is used to cover several eurofer 97 plates. In collaboration with **ENEA Brasimone**, the main goal is to characterize the coating as corrosion barrier in liquid eutectic **Pb-16Li**. The selected thickness, considering the previous results on permeation tests, is 1μm deposited on both sides.
Using the same condition in term of oxygen concentration (dissolution condition) and a temperature of 873K as temperature, several tests at different exposure time (1000h, 2000h, 4000h and 8000h) are expected. Shown results in this thesis regard 1000h test. Essentially, **SEM** analysis have been performed after the corrosion tests. Cross-sectional and top SEM images, for coated samples, have been shown substantially the integrity of the coating with some interaction on the surface.
Finally, during all the Ph.D. program a development of **custom** made **ALD** facility has been carried out. Unfortunately, PLD facility cannot cover a complex and closed geometry like breeding blankets. One of the most candidate, that make requirements of conformity, defect-free and high density coating is of course **ALD** process. Work has been done on process characterization,

defining the set of parameters (ALD valve timing, reaction time, background pressure, purging, precursor temperature and process temperature) to obtained the so-called **ALD regime**. This condition has been defined both for alumina and titania.
The last part, that is still undergoing, has focused on optimization of deposition process onto stainless steel substrates. Preliminary thermal cycles tests have been carried out. Five cycles from 573K to 873K with a heating and cooling ramp of 4K per minute in air have been performed, showing a good thin adhesion and effectiveness barrier against air corrosion.
In spite of exiting results, further research and development is required to qualify the use of ceramic coating in DEMO **breeding blankets**. More specifically, the performance of the PLD-grown coating must be assessed in complex and final geometry with particular concern for the main degradation modes to which **breeding blanket** material will be exposed. The most important are listed here:

- Gaseous permeation tests at different hydrogen partial pressure
- Gaseous permeation tests at higher temperature
- Permeation tests of exposed to eutectic Pb-16Li samples
- Long term exposure to flowing heavy liquid metals
- thermal creep, fatigue, thermal shock
- neutron irradiation

Further improvements of the overall coating performance are desirable in term of ductility, toughness, and adhesive strength.
Indeed, a lot of work must be required for the **ALD** ceramic thin films coatings. In particular preliminary permeation and corrosion tests are mandatory.

4.2 Concluding remarks

In this Ph.D. thesis **PLD** technique has been shown to be a valuable option to produce effectiveness barrier against both hydrogen permeation and corrosion. Although, further R&D is required, PLD-grown alumina is viable in principle.
However, unprecedented results are obtain in term of **PRF**, close to 10^5 for this amorphous alumina. Moreover, the examination of coated plates after short-term corrosion in static **Pb-16Li** at 873K reveal no evident signs of corrosion. Finally, **ALD** has a great potential in term of coating development. Dense, compact and pinhole free alumina thin films are already developed. In conclusion, amorphous Al_2O_3 processed at room temperature by meas **PLD** process is a suitable and promising ceramic coating for DEMO **breeding blankets**.

Chapter 5

Methods

5.1 Pulsed Laser Deposition process

Pulsed Laser Deposition (PLD) is a deposition technique for thin and nano-structured film growth which has started to blossom in the past few years. Conceptually and experimentally, PLD is extremely simple as shown in figure It consists of a target holder and a substrate holder housed in a vacuum chamber. A high-power laser is used as an external energy source to vaporize materials from the target and to deposit thin films on the substrates.

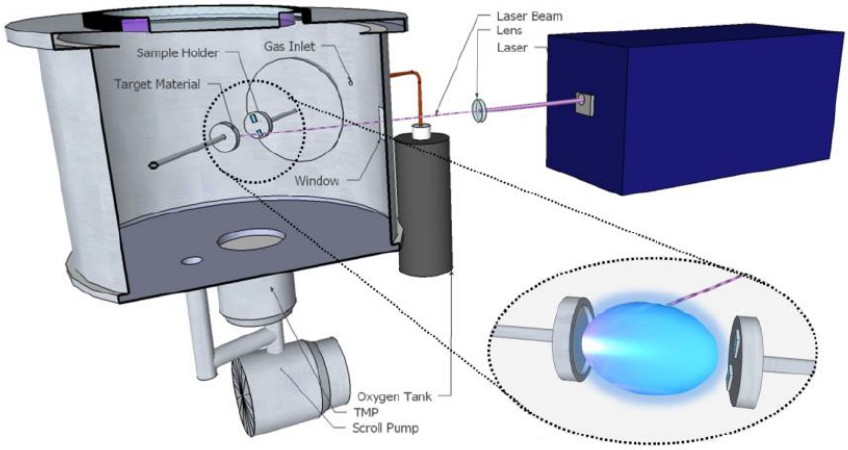

Figure 5.1: Schematic diagram of a pulsed laser deposition apparatus

The resulting films typically possess a Gaussian thickness profile. A set of optical components is used to focus and raster the laser beam over the target surface, which generally mobilized to achieve uniform ablation. The decoupling of the vacuum hardware and the evaporation power source makes this technique so flexible that it is easily adaptable to different operational modes without constraints imposed using internally powered evaporation sources. Film growth can be carried out in a reactive environment containing any kind of gas with or without plasma excitation. In contrast to the simplicity of the hardware, the laser-target interaction is a very complex physical phenomenon. Theoretical descriptions are multidisciplinary and combine both equilibrium and non-equilibrium processes. The mechanism that leads to material ablation depends on laser characteristics, as well as the optical, topological, and the thermodynamically properties of the target. When the laser radiation is absorbed by a solid surface, electromagnetic energy is converted first into electronic excitation and then into thermal, chemical, and even mechanical energy to cause evaporation, ablation, excitation, plasma formation, and exfoliation. Evaporants form a plume consisting of a mixture of energetic species, including atoms, molecules, electrons, ions, clusters, micron-sized solid particulate, and molten globules. The collisional mean free path inside the dense plume is very short. Thus, immediately after the laser irradiation, the plume rapidly expands into the vacuum from the target surface to form a nozzle jet with hydrodynamic flow characteristics. This process attributes to many advantages as well as disadvantages. The advantages are flexibility,fast response, energetic evaporants, congruent evaporation, and great variety of film structures that can be obtained (e.g. compact and homogeneous, columnar or porous). The disadvantages are the presence of micron-sized particulate, and the narrow forward angular distribution that makes large-area

scale-up a very difficult task. PLD is so versatile that with the choice of an appropriate laser, it can be used to grow thin films of any kind of material.[210]

5.2 Atomic Layer Deposition process

Atomic Layer Deposition (ALD) is a vapor phase technique capable of producing high conformal thin films of a variety of materials.
ALD is based on sequential, **self-limiting** reactions, that offers exceptional conformality on high aspect ratio structures. (see figure 5.2).

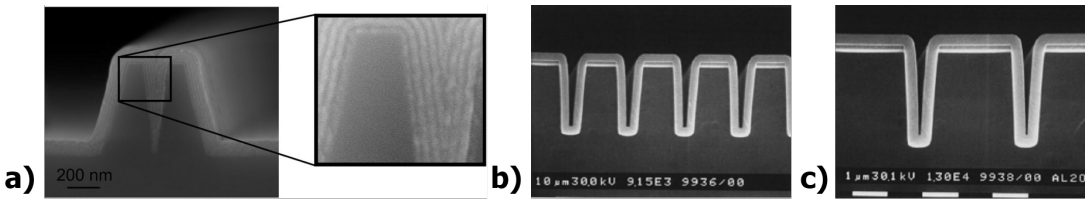

Figure 5.2: (a-c) Examples of oxide thin film (Al_2O_3) deposited on high aspect ratio substrates. Thin film results conformally on overall the coated surfaces.[211]

Atomic Layer Deposition was introduced by Suntola and Anston in 1977 as Atomic Layer Epitaxy depositing ZnS onto flat panel displays. As the most common Chemical Vapor Deposition (CVD) technique, ALD is characterized on chemistry-based reaction to grow the thin film. In contrast to its CVD analogs, the ALD procedures feature alternating exposure of chemical precursors to react to form the desired material (see figure 5.3, often at significantly lower temperature.

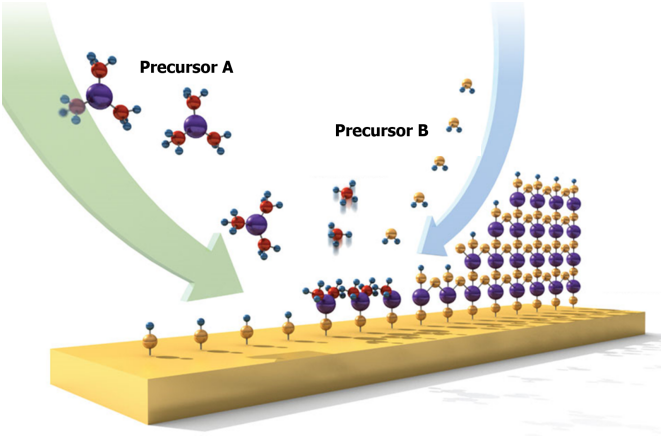

Figure 5.3: Schematic of a ALD binary process. Precursors react separately with the substrate surface in a self-limiting reaction.[212]

Thus, a general ALD process consists of a sequential alternating pulses of gaseous chemical precursors that react with the substrate. These individual gas-surface reactions are called *half*

reactions and appropriately make up only part of the materials synthesis. During each *half reactions*, the precursor is pulsed into a chamber under vacuum (less than 10^{-5} Torr for a stop flow design and around 1 Torr for continuous flow design) for a designed amount of time to allow the precursor to fully react with the substrate surface through a self-limiting that leaves no more than one mono-layer at the surface. Subsequently, the chamber is purged with an inert carrier gas (typically N_2 or Ar) to remove non reacted precursor or reaction by-products. Thus, this processes is cycled until the appropriate film thickness is obtained.[211–215] Here, are reported the essential chemistry of self-limiting reaction of the main oxides materials deposited by means of the **ALD** technique.

Alumina

(A) $AlOH + Al(CH_3)_3 \rightarrow AlOAl(CH_3)_2 + CH_4$
(B) $AlCH_3 + H_2O \rightarrow AlOH + CH_4$
The overall reaction is:
(C) $2Al(CH_3)_3 + 3H_2O \rightarrow Al_2O_3 + 3CH_4$
with a ΔH = -376 kcal.

Titania

(A) $TiCl_4 + 2H_2O \rightarrow TiO_2 + 4HCl$
with a ΔH = -16 kcal.

5.3 Characterization

In this session a review is given on the methods used to characterize the materials and the devices presented in the thesis.

Scanning Electron Microscopy (SEM)

On-top and morphologies images were performed with a scanning electron microscope **Jeol** at the Center for NanoScience and Technology of Istituto Italiano di Tecnologia. High resolution imagining, such as cross-section, was performed with a field emission scanning electron microscope **Zeiss Supra 40. A** at the energy department of Politecnico di Milano.

Atomic Force Microscope (AFM)

The roughness was measured with an **Agilent Technologies Atomic Force Microscopy model 5500**. Static tip deflection was used as a feedback signal. Root Mean Square Roughness (or **Rms**) was measured and evaluated as an average of nine measurements carried out on different sample spots.

PERI II

The permeation of hydrogen through bare and coated Eurofer97 discs (52 mm diameter and 1 mm thickness) was measured using the **PERI II** facility, a courtesy of research center of ENEA Brasimone (Bologna, Italy).[115] A scheme of the facility is shown in figure 5.4

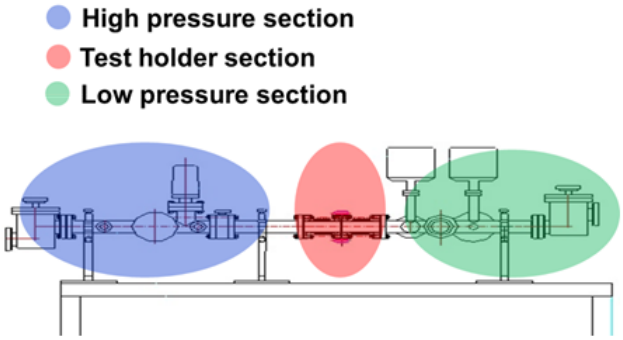

Figure 5.4: Schematic diagram of PERI II facility.

PERI II contains:

- **High pressure section**. Here, the pump group takes pressure down to 10^{-5} Pa. Then, the pumping systems are isolated and the pressure is raised with pure H_2 up to 100 mBar.
- **Low pressure section**. Pump group keeps pressure constantly in the range of 10^{-5} Pa, and a quadrupole mass spectrometer reads ion current due to permeation of H_2 through the samples.
- **Test section**. Here, samples (bare and coated) divides the high pressure section from the low pressure section. The temperature can be set between room temperature and 1023K. In this thesis the temperature tested were 623K, 723K, 823K and 923K.

Quadrupole Mass Spectrometer

H_2 permeation through samples were detected by using a **Quadrupole Mass Spectrometer, Pfeiffer QMS200 Prisma 80**. Hydrogen detection results in ion current variation measured by QMS.

Bibliography

[1] S. Chu, A. Majumdar. *Opportunities and challenges for a sustainable energy future.* Nature 488 (2012) 294.

[2] World list of nuclear power plants. Nucl. News 55 (2012) 55.

[3] *A technology roadmap for Generation IV nuclear energy systems.* Generation IV International Forum, 2002.

[4] *GIF R&D outlook for Generation IV nuclear energy systems.* Generation IV International Forum, 2009.

[5] *Technology roadmap update for Generation IV nuclear energy systems.* Generation IV International Forum, 2014.

[6] S. Saito. *Role of nuclear energy to a future society of shortage of energy resources and global warming.* J. Nucl. Mater. 398 (2010) 1-9.

[7] K. Miyamoto. *Plasma Physics and Controlled Nuclear Fusion.* Springer-Verlag, Berlin & Heidelberg, (2005).

[8] Kenneth S. Krane. *Introductory Nuclear Physics.* John Wiley & Sons, New York, 3rd edition, (1987).

[9] S.J. Zinkle, G.S. Was. *Materials challenges in nuclear energy.* Acta Materialia 61 (2013) 735-758.

[10] ASTM E 521-96. *Standard practice for neutron damage simulation by charged-particle irradiation*, 2000.

[11] M.J. Norgett, M.T. Robinson, I.M. Torrens. *A proposed method of calculating displacement dose rates.* Nucl. Eng. Des. 33 (1975) 50.

[12] R.E. Stoller, M.B. Toloczko, G.S. Was, A.G. Certain, S. Dwaraknath, F.A. Garner. *On the use of SRIM for computing radiation damage exposure.* Nucl. Instrum. Meth. B 310 (2013) 75.

[13] JET project website: http://www.jet.efda.org

[14] J.J. Duderstadt, G.A. Moses. *Inertial confinement fusion.* John Wiley & Sons, New York, (1982).

[15] D. Maisonnier, D. Campbell, I. Cook, L. Di Pace, L. Giancarli, J. Hayward, A. Li Puma, M. Medrano, P. Norajitra, M. Roccella, P. Sardain, M.Q. Tran, D. Ward. *Power plant conceptual studies in Europe.* Nucl. Fusion 47 (2007) 1524-1532.

[16] G. Federici, R. Kemp, D. Ward, C. Bachmann, T. Franke, S. Gonzalez, C. Lowry, M. Gadomska, J. Harman, B. Meszaros, C. Morlock, F. Romanelli, R. Wenninger. *Overview*

of EU DEMO design and R&D activities. Fusion Eng. Des. 89 (2014) 882-889.

[17] D. Stork, P. Agostini, J.L. Boutard, D. Buckthorpe, E. Diegele, S.L. Dudarev, C. English, G. Federici, M.R. Gilbert, S. Gonzalez, A. Ibarra, C. Linsmeier, A. Li Puma, G. Marbach, L.W. Packer, B. Raj, M. Rieth, M.Q. Tran, D.J. Ward, S.J. Zinkle. *Materials R&D for a timely DEMO: Key findings and recommendations of the EU Roadmap Materials Assessment Group.* Fusion Eng. Des. 89 (2014) 1586-1594.

[18] M. Utili. *Sviluppo delle tecnologie a metallo liquido del modulo di blanket HCLL del reattore a fusione ITER e DEMO.* Ph.D. Thesis (2010).

[19] E. Proust, L. Anzidei, G. Casini, M. Dalle Donne, L. Giancarli, S. Malang. *Breeding blanket for DEMO.* 17^{th} symposium on fusion technology (1992).

[20] A.R. Raffray, M. Akiba, V. Chuyanov, L. Giancarli, S. Malang. *Breeding blanket concepts for fusion and materials requirements.* J. Nucl. Mater. 307-311 (2002) 21-30.

[21] U. Fischer, C. Bachmann, J.C. Jaboulay, F. Moro, I. Palermo, P. Pereslavtsev. *Neutronic performance issues of the breeding blanket options for the European DEMO fusion power plant.* Fusion Eng. Des. 109-111 (2016) 1458-1463.

[22] D. Damange, L.V. Bocaccini, F. Franza, A. Santucci, S. Tosti, R. Wagner. *Tritium management and anti-permeation strategies for three different breeding blanket options for the European power plant physics and technology demonstration reactor study.* Fusion Eng. Des. 89 (2014) 1219-1222.

[23] J.E. Pawel, A.F. Rowcliffe, D.J. Alexander, M.L. Grossbeck, K. Shiba. *Effects of low-temperature neutron irradiation on deformation behavior of austenitic stainless steels.* J. Nucl. Mater. 233-237 (1996) 202

[24] T.S. Byun, K. Farrell. *Plastic instability in polycristalline metals ofter low temperature irradiation.* Acta Mater. 52 (2004) 1597.

[25] T.S. Byun, K. Farrell, M. Li. *Deformation in metals after low-temperature irradiation: Part I - Mapping macroscopic deformation modes on true stress-dose plane.* Acta Mater. 56 (2008) 1056.

[26] T.S. Byun, K. Farrell, M. Li. *Deformation in metals after low-temperature irradiation: Part II - Irradiation hardening, strain hardening and stress ratios.* Acta Mater. 56 (2008) 1056.

[27] N. Hashimoto, T.S Byun, K. Farrell. *Microstructural analysis of deformation in neutron-irradiated fcc materials.* J. Nucl. Mater. 351 (2006) 295.

[28] M. Sauzay, K. Bavard, W. Karlsen. *TEM observations and finite elemet modeling of channel deformation in pre-irradiated austenitic stainless steels - Interactions with free surface and grain boundaries.* J. Nucl. Mater. 406 (2010) 152.

[29] M. Victoria, N. Baluc, C. Bailat, Y. Dai, M.I. Luppo, R. Schaublin. B.N. Singh. *The microstructure and assosiated tensile properties of irradiated fcc and bcc metals.* J. Nucl. Mater. 276 (2000) 269.

[30] S.J. Zinkle, B.N. Singh. *Microstructure of neutron irradiated iron before and after tensile deformation.* J. Nucl. Mater. 351 (2006) 269.

[31] L.Cinotti. *Design for LFR and ADS*, VELLA, Karlsruhe, (2008).

[32] S.J Zinkle, J.T Busby. *Structural materials for fission and fusion energy.* Mater. Today 12 (2009) 12.

[33] F.A. Garner, M.B. Toloczko, B.H. Sencer. *Comparison of swelling and irradiation creep behavior of fcc-austenitic and bcc-ferritic/martensitic alloys at high neutron exposure.* J. Nucl. Mater. 276 (2000) 123.

[34] G.S. Was, Y. Ashida, P.L. Andersen. *Irradiation assisted stess corrosion cracking.* Corros. Rev. 29 (2011) 7.

[35] A.F. Roecliffe, J.P. Robertson, R.L. Klueh, K. Shiba, D.J. Alexander, M.L. Grossbeck, S. Jitsukawa. *Fracture toughness and tensile behavior of ferritic-martensitic steels irradiated at low temperatures.* J. Nucl. Mater 258-263 (1998) 1275

[36] A. Hishinuma, A. Kohyama, R.L. Klueh, D.S. Gelles, W. Dietz, K. Ehrlich. *Current status and future R&D for reduced activation ferritic\martensitic steels.* J. Nucl. Mater. 258-263 (1998) 193-204.

[37] J. Knaster, A. Moeslang, T. Muroga. *Materials research for fusion.* Nature Physics 12 (2016) 424-434.

[38] E. Gaganidze, C. Petersen, E. Materna-Morris, C. Dethloff, O.J. Weiss, J. Aktaa, A. Povstyanko, A. Fedoseev, O. Makarov, V. Prokhorov. *Mechanical properties and TEM examination of RAFM steels irradiated up to 70 dpa in BOR-60.* J. Nucl. Mater 417 (2011) 93-98.

[39] B.L. Cox, F.W. Wiffen. *The ductility of molybdenum alloys irradiated between 425 and 1000°C.* J. Nucl. Mater. 85&86 (1973) 901-905.

[40] R.L. Klueh, D.J. Alexander. *Embrittlement of Cr-Mo steels after low fluence irradiation in HFIR.* J. Nucl. Mater. 218 (1995) 151-160.

[41] G.R. Odette, G.E. Lucas. *Analysis of cleavage fracture potential of martensitic stainless steel fusion structures.* J. Nucl. Mater. 117 (1983) 264-275.

[42] M. Rieth, B. Dafferner, H.D. Röhrig. *Embrittlement behavior of different international low activation alloys after neutron irradiation.* J. Nucl. Mater. 258-263 (1998) 1147-1152.

[43] O.P. Maksimkin. *Radiation and radiation-anneal hardening of tantalum.* Phys. Met. Metallogr. 80 (1995) 592-594.

[44] S.J. Zinkle. *Research and development on vanadium alloys for fusion applications.* J. Nucl. Mater. 258-263 (1998) 205-214.

[45] J. Rensman, E. Lucon, J. Boskeljon, J. van Hopen, R. den Boef, P. ten Pierick. *Irradiation resistance of Eurofer97 at 300°C up to 10 dpa.* J. Nucl. Mater. 329-333 (2004) 1113-1116.

[46] E.Lucon, A.Leenars, W. Vandermeulen. *Mechanical response of oxide dispersion stregthened (ODS) EUROFER97 after neutron irradiation at 300°C.* Fusion Eng. Des. 82 (2007) 2438-2443.

[47] N.V. Luzginova, H.S. Nolles, P. ten Pierick, T. Bakker, R.K. Mutnuru, M. Jong, D.T. Blagoeva. *Irradiation response of ODS Eurofer97 steel.* J. Nucl. Mater. 428 (2012) 192-196.

[48] H. Schroeder, H. Ullmaier. *Helium and hydrogen effects on the embrittlement of iron- and nickel- based alloys.* J. Nucl. Mater. 179-181 (1991) 118-124.

[49] S.J. Zinkle, N.M. Ghoniem. *Oprating temperature windows for fusion reactor structural materials.* Fusion Eng. Des. 51-52 (2000) 55-71.

[50] J. Konys, W. Krauss, J. Novotny, H. Steiner, Z. Voss, O. Wedemeyer. *Compatibility behavior of EUROFER steel in flowing Pb-17Li.* J. Nucl. Mater. 386-388 (2009) 678-681.

[51] S. Malang, R. Mattas. *Comparison of lithium and the eutectic lead-lithium alloy, two candidate liquid metal breeder materials for self-cooled blankets.* Fusion Eng. Des. 27 (1995) 399-406.

[52] O.K Chopra, D.L. Smith. *Compatibility of ferritic steels in forced circulation lithium and Pb-17Li systems.* J. Nucl. Mater. 155-157 (1988) 722-727.

[53] P.F. Tortorelli. *Dissolution kinetics of steels exposed in lead-lithium and lithium environments.* J. Nucl. Mater. 191-194 (1992) 965-969.

[54] P.F. Tortorelli. *Corrosion of ferritic steels by molten lithium: influence of competing thermal mass transfer and surface product reactions.* J. Nulc. Mater. 155-157 (1988) 722-727.

[55] M. Broc, T. Flament, P. Fauvet, J. Sannier. *Corrosion of austenitic and martensitic stainless steels in flowing 17Li-83Pb alloy.* J. Nucl. Mater. 155-157 (1988) 715-721.

[56] J.R. DiStefano. *Review of alkali metal and refractory alloy compatibility for rankine cycle applications.* J. Mater. Eng. 11 (1989) 215-225.

[57] J. Saito, M. Morinaga, S. Kano, M. Furui, K. Noda. *Corrosion behavior of Mo-Re based alloys in liquid Li.* J. Nucl. Mater. 264 (1999) 206-215.

[58] H. Feurestein, H. Gräbner, J. Oschinski, S. Horn. *Compatibility of refractory metals and beryllium with molten Pb-Li.* J. Nucl. Mater. 233-237 (1996) 1383-1386.

[59] J.W. Cree, M.F. Amateau. *Degradetion of silicon carbide by molten lithium.* J. Am. Ceram. Soc. 70 (1987) C318-C321.

[60] J.E. Battles. *Materials for advanced high temperature secondary batteries.* Intern. Mater. Rev. 34 (1989) 1-18.

[61] P. Hubberstey, T. Sample. *Thermodynamics of the interactions between liquid breeders and ceramic coating materials.* J. Nucl. Mater. 248 (1997) 140-146.

[62] H. Merher. *Diffusion in solids* Springer (2007)

[63] L. Katz, M. Guinan, R.J. Borg. *Diffusion of H_2, D_2 and T_2 in single-crystal Ni and Cu.* Phys. Rev. 4 (1971) 330-341.

[64] M.R. Louthan, R.G. Derrick. *Permeability of nickel to high pressure hydrogen isotopes.* Scri. Metal. 10 (1976) 53-55.

[65] N.R. Quik, H.H. Johnson. *Permeation and diffusion of hydrogen and deuterium in 310 stainless steel, 472K to 779K.* Metal. Trans. 10 (1979) 67-70.

[66] W.A. Swansiger, R. Bastsz. *Tritium and deuterium permeation in stainless steels: influence of thin oxide films.* J. Nucl. Mater. 85-86 (1979) 335-339.

[67] A.D. Le Claire. *Permeation of gases through solids: 2. An assessment of measurements of the steady-state permeability of H and its isotopes through Fe, Fe-based alloys, and some commercial steels.* Diffusion and Defect Data 34 (1983) 1-35.

[68] A.S. Zarchy, R.C. Axtmann. *Tritium permeation through 304 stainless steel at low pressures.* J. Nucl. Mater. 79 (1979) 110-117.

[69] H.K. Perkins, T. Noda. *Deuterium transport through 304 and 304L stainless steel at low driving pressures and 15KeV deuteron bombardment.* J. Nucl. Mater. 131 (1978) 208-220.

[70] M.I. Baskes. *A calculation of the surface recombination rate constant for hydrogen isotopes on metals.* J. Nucl. Mater. 92 (1980) 318-324.

[71] M.A. Pick, K. Sonnenberg. *A model for atomic-hydrogen metal interactions - Application to recycling, recombination and permeation.* J. Nucl. Mater. 131 (1985) 208-220.

[72] W.R. Wampler. *Surface-limited of deuterium from iron and the effect of surface oxygen.* Appl. Phys. Let. 48 (1986) 405-407.

[73] J. Crank. *The mathematics of diffusion* Oxford University Press (1975).

[74] A. Perujo, K. Douglas, E. Serra. *Low pressure tritium interaction with Inconel 625 and 316L stainless steel surfaces: an evaluetion of the recombination and adsorption constants* Fusion Eng. Des. 31 (1996) 101-108.

[75] I. Ali-Khan, K.J. Dietz, F.G. Waelbroeck, P. Wienhold. *The rate of hydrogen release out of clean metallic surfaces.* J. Nucl. Mater. 76 & 77 (1978) 337-343.

[76] R.A. Causey, M.I. Baskes. *Plasma-driven permeation of deuterium in nickel.* J. Nucl. Mater. 145-147 (1987) 284.

[77] P.M. Richards. *Surface-limited hydrogen release and uptake in metals.* J. Nucl. Mater. 152 (1988) 246.

[78] F. Reiter, S. Alberici, J. Camposilvan, G.B. Cueroni, K. Douglas, K.S. Forcey, G. Gervasini, P.L. Lolli-Ceroni, A. Perujo, E. Serra, S. Tominetti. *Hydrogen Isotopes - Material Interaction Studies at JRC Ispra.* EUR 15269 EN. (1993) b.

[79] R.A. Strehlow, H.C. Savage. *The Permeation of Hydrogen Isotopes Through Structural Metals at Low Pressures and Through Metals with Oxide Film Barriers.* Nucl. Technol. 22 (1974) 127-137.

[80] K.S. Forcey, D.K. Ross, J.C.B. Simpson, D.S. Evans. *Hydrogen transport and solubility in 316L and 1.4914 steels for fusion reactor applications.* J. Nucl. Mater. 160 (1988) 117-124.

[81] T.N Kompaniets, A.A. Kurdyumov. *Surface processes in hydrogen permeation through metal membranes.* Prog. Surf. Sci. 17 (1984) 75-151.

[82] I.V. Gorynin, G.P. Karzov, V.G. Markov, V.A. Yakolev. *Structural materials for atomic reactors with liquid metal heat-transfer agents in the form of lead-bismuth alloy.* Met. Sci. Heat. Treat. 41 (1999) 384.

[83] B.F. Gromov. *Desining the reactor installation with lead-bismuth coolant for nuclear submarines. The brief history. Summarized operation results.* Proceedings of the conference of heavy liquid metal coolants in nuclear technologies. 1-14 (1998) Obninsk.

[84] Nuclear Energy Agency. *Handbook on lead-bismuth eutectic alloy and lead properties, materials compatibility, thermal-hydraulics and technologies* OECD Nuclear science (2015).

[85] G. Müller, A. Heinzel, J. Konys, G. Schumacher, A. Weisenburger, F. Zimmermann, A. Rusanov, V. Markov. *Results of steel corrosion tests in flowing liquid Pb/Bi at 420-600C after 2000 h.* J. Nucl. Mater. 301 (2002) 40-46.

[86] L. Martinelli, T. Dufrenoy, K. Jaakou, A. Rusanov, F. Balbaud-Célérier. *High temeperature oxidation of Fe-9Cr-1Mo steel in stagnant liquid lead-bismuth at several temperatures and for different lead contents in the liquid alloy.* J. Nucl. Mater. 376 (2008) 282-288.

[87] L. Zhang, N. Li, Y. Chen, A.E. Rusanov. *Corrosion behavior of US steel in flowing lead-bismuth eutectic.* J. Nucl. Mater. 336 (2005) 1-10.

[88] M. Machut, K. Sridharan, N. Li, S. Ukai, T. Allen. *Time dependence of corrosion in steels for use in lead alloy-cooled reactors.* J. Nucl. Mater. 371 (2007) 134-144.

[89] O. Yeliseyeva. V.Tsisar, G.Benamati *Influence of temperature on interaction mode of T91 and AISI 316L steels with Pb-Bi melt saturated by oxygen.* Corr. Sci. 50 (2008) 1672-1683.

[90] F. Balbau-Célérier. *Corrosion of steels in liquid lead alloys protected by an oxide layer, application to the MEGAPIE target and to the Russian reactor concept Breast 300.* CEA Report (2003).

[91] E. Yamaki, K. Ginestar, L. Martinelli. *Dissolution mechanism of 316L in lead bismuth eutectic at 500 °C.* Corros. Sci. 53 (2011) 3075.

[92] C. Schroer, O. Wedemeyer, J. Novotny, A. Skrypnik, J. Konys. *Selective leaching of nickel and chromium from type 316L austenitic steel in oxygen-containing lead-bismuth eutectic (LBE).* Corros. Sci. 84 (2014) 113.

[93] E.M. Lyutyi. Soviet Union Materials Science. 24 (1988) 441.

[94] F.N. Remy, M. Bouchacourt. *Flow-assisted corrosion: a method to avoid damage.* 133 (1992) 23-30.

[95] G. Ilinčev. *Research results on the corrosion effects of liquid heavy metals Pb, Bi and Pb-Bi on structural materials with and without corrosion inhibitors.* 217 (2002) 167-177.

[96] E.Heitz. *Chemo-Mechanical effects of flow on corrosion.* 47 (1991) 135-145.

[97] D. Gorse, T. Auger, J.B. Vogt, I. Serre, A. Weisenburger, A. Gessi, P. Agostini, C. Fazio, A. Hojna, F. Di Gabriele, J. Van den Bosch, G. Coen, A. Almazouzi, M. Serrano. *Influence of liquid lead and lead-bismuth eutectic on tensile, fatigue, and creep properties of Ferritic-Martensitic and Austenitic steels for transmutation systems.* J. Nucl. Mater. 415 (2011) 284.

[98] J. Van den Bosch, P. Hosemann, A. Almazouzi, S.A. Maloy. *Liquid Metal Embrittlement of T91 martensitic steel evidenced by small punch tests.* Nucl. Eng. Des. 237 (2007) 677.

[99] B. Long, Y. Dai. *Investigation of the LBE embrittlement effects on the fracture properties of T91.* J. Nucl. Mater. 376 (2008) 341.

[100] J. Van den Bosch, R.W. Bosch, D. Sapundijev, A. Almazouzi.*Liquid metal embrittlement susceptibility of ferritic-martensitic steel in liquid lead alloys.* J. Nucl. Mater. 376 (2008) 322.

[101] J. Van den Bosch, G. Coen, A. Almazouzi, J. Degrieck. *Fracture toughness assessment of ferritic-martensitic steel in liquid lead-bismuth eutectic.* J. Nucl. Mater. 385 (2009) 250.

[102] J. Van den Bosch, P. Hosemann, A. Almazouzi, S.A. Maloy. *Liquid metal embrittlement of silicon enriched steel for nuclear applications.* J. Nucl. Mater. 398 (2010) 116.

[103] G. Coen, J. Van den Bosch, A. Almazouzi, J. Degrieck. *Investigation of the effect of lead-bismuth eutectic on the fracture properties of T91 and 316L.* J. Nucl. Mater. 398 (2010) 122.

[104] J. Van den Bosch, G. Coen, P. Hosemann, S.A. Maloy. *On the LME susceptibility of Si enriched steels* J. Nucl. Mater. 429 (2012) 105.

[105] C. Ye, J.B. Vogt, I. Proiol-Serre. *Liquid metal embrittlement of the T91 steel in lead bismuth eutectic: the role of loading rate and the oxygen content in the liquid metal.* Mater. Sci. Eng. A 608 (2014) 242.

[106] A. Jianu, G. Müller, A. Weisenburger, C. Fazio, V.G. Markov, A.D. Kasthanov. *Creep-to-rupture tests of T91 steel in flowing Pb-Bi eutectic melt at 550° C.* J. Nucl. Mater. 394 (2009) 102.

[107] A. Verleene, J.B. Vogt, I. Serre, A. Legris. *Low cycle fatigue behavior of T91 martensitic steel at 300 °C in air and in liquid lead bismuth eutectic.* Int. J. Fatigue 28 (2006) 843.

[108] A. Weisenburger, A. Heinzel, C. Fazio, G. Müller, V.G. Markow, A.D. Kastanov. *Low cycle fatigue tests of surface modified T91 steel in 10^{-6} wt.% oxygen containing $Pb_{45}Bi_{55}$ at 550 °C.* J. Nucl. Mater. 377 (2008) 261.

[109] J.B. Vogt, I. Proriol-Sierre. *Fatigue behavior of a martensitic and an austenitic steel in heavy liquid metals.* Procedia Eng. 55 (2013) 812

[110] R.A. Causey, W.R. Wampler, J.R. Rettelle, J.L. Kaane. *Tritium migration in vapor-deposited β-silicon carbide.* J. Nucl. Mater. 203 (1993) 196-205.

[111] K. Verghese, L.R. Zumwalt, C.P. Feng, T.S. Elleman. *Hydrogen permeation through non-metallic solids.* J. Nucl. Mater. 85/86 (1979) 1161-1164.

[112] R.M. Roberts, T.S. Elleman, H. Palour III, K. Verghese. *Hydrogen permeability of sintered aluminum oxide.* J. Am. Ceram. Soc. 62 (1979) 495-499.

[113] J. Konys, W. Krauss, N. Holstein. *Development of advanced Al coating processes for future application as anti-corrosion and T-permeation barriers.* Fusion Eng. Des. 85 (2010) 2141-2145.

[114] J. Konys, W. Krauss, H. Steiner, J. Novotny, A. Skrypnik. *Flow rate dependent corrosion behavior of Eurofer steel in Pb-15.7Li.* J. Nucl. Mater. 417 (2011) 1991-1194.

[115] A. Aiello, M. Utili, S. Scalia, G. Coccoluto. *Experimental study of efficiency of natural oxide layers for reduction of tritium permeation through EUROFER 97.* Fusion Eng. Des. 84 (2009) 385-389.

[116] A. Aiello, M. Utili, A. Ciampichetti. *Reduction of tritium permeation through Inconel 718 and Incoloy 800 HT by means of natural oxides.* J. Nucl. Mater. 417 (2011) 1162-1165.

[117] G.W. Hollenberg, E.P. Simonen, G. Kalinin. *Tritium hydrogen barrier development.* Fusion Eng. Des. 28 (1995) 190-208.

[118] P. Hubberstey, T. Sample, A. Terlain. *The stability of tritium permeation barriers and the self-healing capability of aluminade coatings in liquid Pb-17Li.* Fusion Tech. 28 (1995) 1194-1199.

[119] Z.G. Zhang, F. Gesmundo, P.Y. Hou, Y. Niu. *Criteria for the formation of protective scales on Fe-Al and Fe-Cr-Al alloys.* Corr. Sci. 48 (2006) 741.

[120] B.A. Pint, J.R. Martin, L.W. Hobbs. *The oxidation mechanism of θ-Al_2O_3 scales.* Solid State Ionics 78 (1995) 99-107.

[121] B.A. Pint, K.L. More. *Transformation of Al_2O_3 to $LiAlO_2$ in Pb-17Li at 800°C.* J. Nucl. Mater. 376 (2008) 108-113.

[122] B.A. Pint. *The effect of coatings on the compatibility of Fe-Cr steels with Pb-Li.* J. Nucl. Mater. 417 (2011) 1195-1199.

[123] K.S. Forcey, D.K. Ross, C.H. Wu. *The formation of hydrogen permeation barriers on steels by aluminizing.* J. Nucl. Mater. 182 (1991) 36.

[124] E. Serra, A. Calza Bini, G. Cosoli, L. Pilloni. *Hydrogen permeation measurements on alumina.* J. Am. Ceram. Soc. 88 (2005) 15-18.

[125] D. Levchuck, F. Koch, H. Maier, H. Bolt. *Deuterium permeation through Eurofer and α-alumina coated Eurofer.* J. Nucl. Mater. 328 (2004) 103-106.

[126] F. Koch, R. Brill, H. Maier, D. Levchuck, A. Suzuki, T. Muroga, H. Bolt. *Crystallization behavior of arc-deposited ceramic barrier coatings.* J. Nucl. Mater. 329 (2004) 1403-1406.

[127] D.Levchuck, F.Koch, H. Maier, H. Bolt. *Gas-driven deuterium permeation through Al_2O_3 coated samples.* Phys. Scr. (2004) 119-123.

[128] Y. Ueki, T. Kunogi, N.B. Morley, M.A. Abdou. *Electrical insulation test of alumina coating fabricated by Sol-Gel method in molten Pb-Li pool.* Fusion Eng. Des. 85 (2010) 1824-1828.

[129] A. Aiello, I. Recapito, G. Benamati, A. Ciampichetti. *Qualification of tritium permeation barriers in liquid Pb-17Li.* Fusion Eng. Des. 69 (2013) 245-252.

[130] T. Terai, T. Yoneoka, H. Tanaka, H. Kawamura, M. Nakamichi, K. Miyajima. *Tritium permeation through austenitic stainless steel with chemically densified coating as a tritium permeation barrier.* J. Nucl. Mater. 212-215 (1994) 976-980.

[131] G.W. Hollenberg, E.P. Simonen, G. Kalinin, A. Terlain. *Tritium/Hydrogen barrier development.* Fusion Eng. Des. 28 (1995) 190-208.

[132] A. Perujo, K.S. Forcey. *Tritium permeation barriers for fusion technology.* Fusion Eng. Des. 28 (1995) 252-257.

[133] E. Serra, P.J. Kelly, D.K. Ross, R.D. Arnell. *Alumina sputtered on MANET as an effective deuterium permeation barrier.* J. Nucl. Mater. 257 (1998) 194-198.

[134] G. Benamati, C. Chabrol, A. Perujo, E. Rigal, H. Glasbrenner. *Development of tritium permeation barriers on Al base in Europe.* J. Nucl. Mater. 271-272 (1999) 391-395.

[135] R. Hecker, D. Stover, H. Jonas, H.P. Buchkremer. *Properties of chromia scales on high temperature alloys used as barriers against hydrogen permeation.* J. Nucl. Mater. 171 (1990) 84-93.

[136] M. Nakamichi, H. Nakamura, K. Hayashi, I. Takagi. *Impact of ceramic coating deposition on the tritium permeation in the japanese ITER-TBM.* J. Nucl. Mater. 386-388 (2009) 692-695.

[137] J.G. McGuire. *Hydrogen permeation resistance layers for liquid metal reactors.* Proc. Conf. on Tritium Technology in Fission, Fusion and Isotopic Applications. Dyton OH. (1980) 64-68.

[138] K.S. Forcey, D.K. Ross, J.C.B. Simpson, D.S. Evans, A.G. Whitaker. *The use of aluminizing on 316L austenitic and 1.4914 martensitic steels for the reduction of tritium leakege from the NET blanket.* J. Nucl. Mater. 161 (1989) 108-116.

[139] E.H. Van Deventer, V.A. MacLaren, V.A. Maroni. *Hydrogen permeation characteristics of aluminum-coated and aluminum-modified steels.* J. Nucl. Mater. 88 (1980) 168-173.

[140] E.R. Gilbert, R.P. Allen, D.L. Baldwin, R.D. Bell, J.L. Brimhall, R.G. Clemmer, S.C. Marschman, M.A. McKinnon, R.E. Page, H.G. Powers, S.G. Chalk. *Tritium permeation and related studies on barrier treated 316 stainless steel.* Fusion Technol. 21 (1992) 739-744.

[141] A. Perujo, K.S. Forcey, T. Sample. *Reduction of deuterium permeation through DIN 1.4911 stainless steel (MANET) by plasma spray deposited aluminum.* J. Nucl. Mater. 207 (1993) 86-91.

[142] A. Muhlratzer, H. Zeilinger, H.G. Esser. *Development of protective coating to reduce hydrogen and tritium permeation.* Nucl. Technol. 66 (1984) 570-577.

[143] C. Shan, A. Wu, Y. Li, Z. Zhao, Q. Chen, Q. Huang, S. Shi. *The behavior of diffusion and permeation of tritium through 316L stainless steel with coating of TiC and TiN/TiC.* J. Nucl. Mater. 191-194 (1992) 221-225.

[144] K.S. Forcey, A. Perujo, F. Reiter, P.L. Lolli Ceroni. *The formation of tritium permeation barrier by CVD.* J. Nucl. Mater. 200 (1993) 417-420.

[145] M. Bonelli, R. Checchetto, L.M. Gratton, L. Guzman, A. Miotello, C. Tosello, I. Scotoni, F. Ferrari, L. Calliari, C. Cestari, M. Elena, N. Laidani, E. Voltolini, B. Mussini. *Study of hydrogen diffusion behavior in PVD deposited and ion bombarded thin TiN film barriers on nuclear grade 316L stainless steel.* Fusion Technol. (1992) 196-200.

[146] T. Nelson, G.T. Murray. *Prevention of hydrogen embrittlement by TiO_2 surface layer.* Metall. Trans. A. 15 (1984) 597-600.

[147] J. Bowker, G.R. Pierch. *The effect of a thin barrier layer on the permeation of hydrogen through mild steel and ferritic stainless steel.* Metall. Trans. A. 15 (1984) 2093-2095.

[148] A.M. Brass, J. Chene, J.C. Pivin. *Influence of nitrogen ion implantation on hydrogen permeation in an extra mild steel.* J. Mater. Sci. 24 (1989) 1693-1699.

[149] T. Chikada, A. Suzuki, T. Kobayashi, H. Maier, T. Terai, T. Muroga. *Microstructure change and deuterium permeation behavior of erbium oxide coating.* J. Nucl. Mater. 417 (2011) 1241-1244.

[150] T. Chikada, A. Suzuki, C. Adelhelm, T. Terai, T. Muroga. *Surface behavior in deu-*

terium permeation through erbium oxide coatings. Nucl. Fusion 51 (2011) 063023.

[151] T. Chikada, A. Suzuki, T. Terai, T. Muroga, F. Koch. *Compatibility of Erbium oxide coating with liquid lithium-lead alloy and corrosion protection effect of iron layer.* Fusion Eng. Des. 88 (2013) 640-643.

[152] T. Chikada, S. Naitoh, A. Suzuki, T. Terai, T. Tanaka, T. Muroga. *Deuterium permeation through erbium oxide coatings on RAFM steels by a dip-coating technique.* J. Nucl. Mater. 442 (2013) S33-S37.

[153] T. Chikada, A. Suzuki, F. Koch, H. Maier, T. Terai, T. Muroga. *Fabrication and deuterium permeation properties of erbia-metal multilayer coatings.* J. Nucl. Mater. 442 (2013) S592-S596.

[154] T. Chikada, M. Shimada, R.J. Pawelko, T. Terai, T. Muroga. *Tritium permeation experiments using reduced activation ferriticmartensitic steel tube and erbium oxide coating.* Fusion Eng. Des. 89 (2014) 1402-1405.

[155] M.F. Ashby. *Materials selection in mechanical design.* Butterworth Heinmann (1999)

[156] T. Sample, A. Perujo, H. Kolbe, B. Mancinelli. *The hydrogen permeation behavior of aluminised coated martenstic steels under gaseous hydrogen, liquid Pb-17Li/hydrogen and cyclic tensile load.* J. Nucl. Mater. 283-287 (2000) 1272-1276.

[157] J. Konys, A. Aiello, G. Benamati, L. Giancarli. *Status of tritium permeation barrier development in the EU.* Fusion Sci. Tech. 47 (2005) 844-850.

[158] A. Perujo, E. Serra, H. Kolbe, T. Sample. *Hydrogen permeation rate reduction by post-oxidation of aluminide coatings on DIM 1.4914 martensitic steel (MANET).* J. Nucl. Mater. 233-237 (1996) 1102-1106

[159] E. Serra, A. Perujo. *Influence of the surface conditions on permeation in the deuterium-MANET system.* J. Nucl. Mater. 240 (1997) 215-220.

[160] A. Aiello, G. Benamati, M. Chini, C. Fazio, E. Serra, Z. Yao. *Hydrogen permeation through tritium permeation barrier in Pb-17Li.* Fusion Eng. Des. 58-59 (2001) 737-742.

[161] A. Aiello, A. Ciampichetti, G. Benamati. *An overview on tritium permeation barrier development for WCLL blanket concept.* J. Nucl. Mater. 329-333 (2004) 1398-1402.

[162] K.A. Unocic, B.A. Pint. *Alloying and coating strategies for improved Pb-Li compatibility in DEMO-type fusion reactors.* J. Nucl. Mater. 455 (2014) 330-334.

[163] A. Rouaix-Vande Put, B.A Pint. *Inhibited aluminization of an ODS FeCr alloy.* Surf. Coat. Technol. 206 (2012) 5036-5041.

[164] B.A. Pint, L.D. Chitwood, J.R. Di Stefano. *Long-term stability of ceramics in liquid lithium.* J. Nucl. Mater. 289 (2001) 52-56.

[165] Y. Wu, D. He, H. Zhang, S. Li, X. Liu, S. Wang, L. Jiang. *Preparation of yttrium ox-*

ide coating by MOCVD as tritium permeation barrier. Fusion Eng. Des. 90 (2015) 105-109.

[166] H.G. Yang, Q. Zhan, W.W. Zhao, X.M. Yuan, Y. Hu, Z.B. Han. *Study of an iron-aluminide and alumina tritium barrier coating*. J. Nucl. Mater. 417 (2011) 1237-1240.

[167] W. Krauss, J. Konys, N. Holstein, H. Zimmermann. *Al-based anti-corrosion and T-permeation barrier development for future DEMO blankets*. J. Nucl. Mater. 417 (2011) 1233-1236.

[168] S.E. Wulf, W. Krauss, J. Konys. *Comparison of coating processes in the development of aluminum-based barriers for blanket applications*. Fusion Eng. Des. 89 (2014) 2368-2372.

[169] S.E. Wulf, N. Holstein, W. Krauss, J. Konys. *Influence of deposition conditions on the microstructure of Al-based coatings for applications as corrosion and anti-permeation barrier*. Fusion Eng. Des. 88 (2013) 2530-2534.

[170] J. Konys, W. Krauss, N. Holstein, J. Lorenz. S.E. Wulf, K. Bhanumurthy. *Impact of heat treatment on surface chemistry of Al-coated Eurofer for application as anti-corrosion and T-permeation barriers in a flowing Pb-15.7Li environment*. Fusion Eng. Des. 87 (2012) 1483-1486.

[171] W. Krauss, J. Konys, S.E. Wulf. *Corrosion barriers processed Al electroplating and their resistance against flowing Pb-15.7Li*. J. Nucl. Mater. 455 (2014) 522-526.

[172] A. Santucci, A. Ciampichetti, D. Demange, F. Franza, S. Tosti. *Tritium migration in HCLL and WCLL blankets: Impact of tritium solubility in liquid Pb-17Li*. IEEE Transaction on Plasma Science. 42 (2014) 1053-1057.

[173] A. Pisarev, I. Tsvetkov, S. Yarko. *Hydrogen permeation through membranes with cracks in protection layer*. Fusion Eng. Des. 82 (2007) 2120-2125.

[174] P.F. Carcia, R.S. McLean, Z.G. Li, M.H. Reilly, W.J. Marshall. *Permeability and corrosion in $ZrO_2Al_2O_3$ nanolaminate and Al_2O_3 thin films grown by atomic layer deposition on polymers*. J. Vac. Sci. Technol. A 30(4) (2012) 041515

[175] F. Di Fonzo, D. Tonini, A. Li Bassi, C.S. Casari, M.G. Beghi, C.E. Bottani, D. Gastaldi, P. Vena, R. Contro. *Growth regimes in pulsed laser deposition of aluminium oxide fils*. Appl. Phys. A. 93 (2008) 765.

[176] V. Edlmayr, M. Moser, C. Walger, C. Mitterer. *Thermal stability of sputtered Al_2O_3 coatings*. Surf. Coat. Technol. 204 (2010) 1576.

[177] C. Cibert, H. Hidalgo, C. Champeaux, P. Tristant, C. Tixer, J. Desmaison. A. Catherinot. *Properties of aluminium oxide thin films deposited by pulsed laser deposition and plasma enhanced chemical vapor deposition*. Thin solid films 516 (2008) 1290.

[178] P. Eklund, M. Sridharan, G. Singh, J. Bottinger. *Thermal stability and phase transformations of γ-/amorphous-Al_2O_3 thin films*. Plasma Process. Polym. 6 (2009) S907.

[179] M. Sridharan, M. Sillassen, J. Bottinger, J. Chevallier, H. Birkedal. *Pulsed DC magnetron sputtered Al_2O_3 films and their hardness.* Surf. Coat. Technol. 202 (2007) 920.

[180] A. Khanna, D.G. Bhat, A. Harris, B.D. Beake. *Structure-property correlations in aluminum oxide thin films grown by reactive AC magnetron sputtering.* Surf. Coat. Technol. 201 (2006) 1109.

[181] D. Iadicicco *High performance alumina protective coatings.* Master Thesis (2013) Politecnico di Milano.

[182] F. García Ferré, E. Bertarelli, A. Chiodoni, D. Carnelli, D. Gastaldi, P. Vena, M.G. Beghi, F. Di Fonzo. *The mechanical properties of a nanocrystalline Al_2O_3/a-Al_2O_3 composite coating measured by nanoindentation and Brillouin spectroscopy.* Acta Mater. 61 (2013) 2662.

[183] A. Leyland, A. Matthews. *On the significance of the H/E ratio in wear control: a nanocomposite coating approach to optimized tribological behavior.* Wear 246 (2000) 11.

[184] F.G. FerrÃ©, A. Mairov, L. Ceseracciu, Y. Serruys, P. Trocellier, C. Baumier, O. Kaïtasov, R. Brescia, D. Gastaldi, P. Vena, M.G. Beghi, L. Beck, K. Sridharan, F. Di Fonzo. *Radiation endurance in Al_2O_3 nanoceramics.* Sci. Rep. 6 (2016) 33478.

[185] S. Li, D. He, X. Liu, S. Wang, L. Jiang. *Deuterium permeation of amorphous alumina coating on 316L prepared by MOCVD.* J. Nucl. Mater. 420 (2012) 405-408.

[186] T. Chikada, A. Suzuki, Z. Yao, D. Levchuck, H. Maier, T. Terai, T. Muroga. *Deuterium permeation behavior of erbium oxide coating on austenitic, ferritic and ferriticmartensitic steels.* Fusion Eng. Des. 84 (2009) 590-592.

[187] T. Shrestha, M. Basirat, I. Charit, G.P. Potirniche, K.K. Rink. *Creep deformation mechanisms in modified 9Cr-1Mo steel.* J. Nucl. Mater 423 (2012) 110.

[188] M. Basirat, T. Shrestha, G.P. Potirniche, I. Charit, K.K. Rink. *A study of the creep behavior of modified 9Cr-1Mo steel using continuum damage modeling.* Int. J. Plast. 37 (2012) 95.

[189] T. Shrestha, M. Basirat, I. Charit, G.P. Potirniche, K.K. Rink. *Creep rupture behavior of grade 91 steel* Mater. Sci. Eng. A 565 (2013) 382.

[190] J.C. Ahn, G.M. Sim, K.S. Lee. *Effect of aging treatment on high temperature strength of Nb added ferritic stainless steels* Mater. Sci. Forum 475 (2005) 191.

[191] B.J. Ganesh, S. Raju, A.K. Rai, E. Mohandas, M. Vijayalakshmi, K.B.S. Rao, B. Raj. *Differential scanning calorimetry study of diffusional and martensitic transformations in some 9 wt-% Cr low carbon ferritic steels.* Mater. Sci. Technol. 27 (2011) 500.

[192] M. Yoshino, Y. Mishima, Y. Toda, H. Kushima, K. Sawada, K. Kimura. *Influence of normalizing heat treatment on precipitation behavior in modified 9Cr-1Mo steel.* Mater. High. Temp. 25 (2008) 149.

[193] T.C. Totemeier, H. Tian, J.A. Simpson. *Effect of normalization temperature on the creep strength of modified 9Cr-1Mo steel.* Metall. Mater. Trans 37 (2005) 1519.

[194] V. Dudko, A. Delyakov, R. Kaibyshev. *Effect of tempering on mechanical properties and microstructure of a 9% Cr heat resistant steel.* Mater. Sci. Forum. 706 (2012) 841.

[195] K. Sawada, K. Suzuki, H. Kushima, M. Tabuchi, K. Kimura. *Effect of tempering temperature on Z-phase formation and creep stregth in 9Cr-1Mo-V-Nb-N steel.* Mater. Sci. Eng. A 480 (2008) 558.

[196] A. Moroño, E.R. Hodgson, M. Malo. *Radiation enhanced deuterium adsorption for Al_2O_3 and macor ceramic.* Fus. Eng. and Design. 88 (2013) 2488.

[197] E.R. Hodgson, M. Malo, A. Moroño. *Radiation testing of diagnostic window bonding for enhanced H isotopes diffusion.* Fus. Eng. and Design. 86 (2011) 2466.

[198] J. Zhang, P. Hosemann, S. Maloy. *Models of liquid metal corrosion.* J. Nucl. Mater. 404 (2010) 82-96.

[199] P.F. Tortorelli, O.K. Chopra. *Corrosion and compatibility considerations of liquid metals for fusion reactor applications.* J. Nucl. Mater. 103-104 (1981) 621-632.

[200] P.F. Tortorelli, J.H. Devan. *Compatibility of stainless steel with Pb-17Li At. Pct Li.* J. Mater. Energy Syst. 4 (1982) no. 2.

[201] J. Konys, W. Krauss, Z. Zhu, Q. Huang. *Comparison of corrosion behavior of EUROFER and CLAM steels in flowing Pb15.7Li.* J. Nucl. Mater. 455 (2014) 491-495.

[202] B.A. Pint, K.A. Unocic. *Pb-Li compatibility issues for DEMO.* J. Nucl. Mater. 442 (2013) S572-S575.

[203] B.A. Pint, J.L. Moser, P.F. Tortorelli. *Investigation of Pb-Li compatibility issues for the dual coolant blanket concept.* J. Nucl. Mater. 367-370 (2007) 1150-1154.

[204] B.A. Pint, J.L. Moser, P.F. Tortorelli. *Liquid metal compatibility issues for test blanket modules.* Fusion. Eng. Des. 81 (2006) 901-908.

[205] R.J. Pulham, P. Hubberstey. *Comparison of chemical reactions in liquid lithium with those in liquid sodium.* J. Nucl. Mater. 115 (1983) 239-250.

[206] R.S. Kumar, M. Auch, E. Ou, G. Ewald, C.S. Jin. *Low moisture permeation measurement through polymer substrates for organic light emitting devices.* Thin Solid Films. 417 (2002) 120-126.

[207] J. Meyer, P. Goern, F. Bartam, S. Hamwi, T. Winkler, H.H. Johannes, T. Weimann, P. Hinze, T. Riedl, W. Kowalsky. *$Al_2O_3ZrO_2$ nanolaminates as ultrahigh gas-diffusion barriers - A strategy for reliable encapsulation of organic electronics.* Adv. Mater. 21 (2009) 1845-1849.

[208] P.F. Carcia, R.S. McLean, M.D. Groner, A.A. Dameron, S.M. George. *Gas diffusion untrabarriers on polymer substrates using Al_2O_3 atomic layer deposition and SiN*

plasma-enhanced chemical vapor deposition. J. Appl. Phys. 106 (2009) 023533.

[209] A. Behrendt, C. Friedenberger, T. Gahlmann, S. Trost, T. Becker, K. Zilberberg, A. Polywka, P. Goern, T. Riedl. *Highly robust transparent and conductive gas diffusion barriers based on TiN oxide.* Adv. Mater. 27 (2015) 5061-5967.

[210] D.B. Chrisley, G. Hubler. *Pulsed Laser Deposition of Thin Films.* Wiley & Sons, 1994.

[211] D.C. Miller, R.R. Foster, S.H. Jen, J.A. Bertrand, S.J. Cunningham, A.S. Morris, Y.C. Lee, S.M. George, M.L. Dunn. *Thermomechanical properties of alumina films created using atomic layer deposition technique.* Sensor and Actuators. A 164 (2010) 58-67.

[212] S.M. George. *Atomic Layer Deposition: An Overview.* Chem. Rev. 110 (2010) 111-131.

[213] B. Diaz, E. Harkonen, J. Swiatowska, V. Maurice, A. Seyeux, P. Marcus, M. Ritala. *Low-temperature atomic layer deposition of Al_2O_3 thin coatings for corrosion protection of steel: Surface and electrochemical analysis.* Corr. Sci. 53 (2011) 2168-2175.

[214] E. Marin, L. Guzman, A. Lanzutti, W. Ensinger. L. Fedrizzi. *Multilayer $Al_2O_3TiO_2$ atomic layer deposition coatings for the corrosion protection of stainless steel.* Thin Solid Films. 522 (2012) 283-288

[215] E. Marin, A. Lanzutti, L. Guzman, L. Fedrizzi. *Corrosion protection of AISI 316 stainless steel by ALD aluminatitania nanomettric coatings.* J. Coat. Technol. Res. 8 (2011) 655-659.

List of Tables

List of Figures